DESIGN AND FABRICATION OF PIEZOELECTRIC MICRO GENERATOR USING LASER MICROMACHINING AND MEMS TECHNIQUE

by

HYUNUK KIM

Presented to the Faculty of the Graduate School of

The University of Texas at Arlington in Partial Fulfillment

of the Requirements

for the Degree of

MASTER OF SCIENCE IN MATERIALS SCIENCE AND ENGINEERING

THE UNIVERSITY OF TEXAS AT ARLINGTON

AUGUST 2008

Copyright © HYUNUK KIM 2008

All Rights Reserved

ACKNOWLEDGEMENTS

First of all, I want to express my appreciation to the Dr. Priya, Dr. Lee, and Dr. Bruce Gnade for supporting my research and providing motivation to do this research. Without Dr. Priya's advice related to piezoelectric material, this research could not be completed. The guidance of Dr. Lee on device design and fabrication was also an essential part of this research. Whenever I felt a lack of experience and knowledge in fabrication processes, Dr. Gnade at UT Dallas showed me the way to go.

I also would like to express that it was a great honor for me to study under the greatest professors in the world, especially, Dr. Pranesh Aswath, Dr. Choong-Un Kim, and Dr. Michael Jin. Their classes inspired me to continue the journey of knowledge. Thanks to Dr. Rashed Islam, Vishwas Bedekar, Rahul Mahajan and Makarand Karmarkar who gave me much of support during this research. I would like to thank to Bo-Hoon Kim, Kun Hee Han, Emil H. Zin, and Chun-Young Lee who refreshed my mind whenever I was depressed. Rakesh, who has the mildest smile in the ARRI, supported me to do backside lithography. Thanks to all my friends at UT Arlington who remember the late nights in nanofab, ARRI, and Woolf Hall.

Most of all, I would like to extend special thanks to my father, mother, and younger brother in my hometown. And thanks to god who helps me keep peace of mind.

June 16, 2008

ABSTRACT

Design and fabrication of piezoelectric micro generator using laser micromachining and mems technique

HyunUk Kim, M.S.

The University of Texas at Arlington, 2008

Supervising Professor: Supervising Professor Shashank Priya

I. An energy harvesting device based on $Pb(Zr_{0.52}Ti_{0.48})O_3$-$Pb(Zn_{1/3}Nb_{2/3})O_3$ ceramics was fabricated by using laser micromachining technique. It was found that the laser machining process did not have a significant effect on electrical properties of piezoelectric material. The device was found to generate continuous power of 1.13 μW at 870Hz across a 288.5 kΩ load with power density of 301.3 $\mu W/cm^3$. The characterization was conducted in low frequency regime of 50-1000Hz at the constant force of 8g (where $g=9.8m/s^2$).

II. In order to fabricate a lead free MEMS device, $BaTiO_3$ was selected as the piezoelectric material. $BaTiO_3$ gel was synthesized by aqueous process using barium acetate and titanium bis (ammonium lacto) dihydroxide. This solution is very stable in air at room temperature over a long period of time, compared to other sols using non aqueous systems. By incorporating PVP (Polyvinylpyrrolidone) during the synthesis process, and increasing surface

energy of the substrate by plasma treatment, a 600nm thick crack-free film with (111) preferred orientation was obtained. $BaTiO_3$ has tetragonal symmetry at room temperature and by orienting the polarization along (111) direction high piezoelectric properties can be obtained.

III. A piezoelectric micro-generator based on lead free barium titanate thin film was fabricated by using MEMS approach. This device may be a promising candidate to supply power to implantable sensors in medical applications. $BaTiO_3$ polycrystalline thin films on SOI (Silicon On Insulator) were used to fabricate the micro-generator. The etching rate of $BaTiO_3$ thin film by using 2% HF solution was determined to be in the range of 86nm/min to 187nm/min. The fabricated device had interdigital electrode pattern which allowed accessing the longitudinal piezoelectric coefficients. Each cell of the micro-generator had six cantilevers connected in series to provide high voltage.

TABLE OF CONTENTS

ACKNOWLEDGEMENTS……………………………………………………………………… iii

ABSTRACT……………………………………………………………………………………… iv

LIST OF ILLUSTRATIONS………………………………………………………………….. ix

LIST OF TABLES……………………………………………………………………………... xiii

Chapter Page

1. INTRODUCTION………………...... 1

1.1 Mechanical Vibration sources…………………………………………………….. 2

1.1.1 Power spectral density (PSD) curve… 4

1.2 Power estimation from spring mss system, Electrical energy and Energy harvesting..5

1.2.1 Power estimation from spring mass system. 5

1.2.2 Simple equivalent circuit model...…................................... ..5

1.2.3 Energy density of capacitor…..6

1.3 Energy harvesting circuit……………………………….................................7

1.3.1 Rectification (AC/DC conversion)..………………………....... 8

1.3.2 Filter capacitor...………………………... 9

1.3.3 Buck converter (Step down): A simple description of DC/DC conversion…………………............9

1.3.4 Energy storage in capacitor……………………………….. 10

1.4 Piezoelectric materials………………………………………………………… 11

1.4.1 Piezoelectricity………………………………………………… 11

1.4.2 Electromechanical factors……………………………............. 15

1.5 Current status of Piezoelectric Macro-generators…………………...................16

1.6 Laser micro-machining 18

1.7 Principle of Sol-Gel synthesis 19

1.8 Textured piezoelectric thin film 20

1.9 Domain engineering 20

1.10 Process flow for MEMS device 21

1.10.1 Etching process 21

1.10.2 Patterning or photolithography 23

1.10.3 Packaging 23

1.11 MEMS (Micro-Electromechanical system) energy harvesting device 24

1.12 Current status of piezoelectric micro-generator 25

2. ENERGY HARVESTING DEVICE FABRICATED BY LASER MICROMACHINING OF $Pb(Zr_{0.52}Ti_{0.48})O_3$-$Pb(Zn_{1/3}Nb_{2/3})O$ 28

2.1 Fabrication process 30

2.2 Experiment setup 32

2.3 Result and discussion 34

2.4 Summary 39

3. BARIUM TITANATE THIN FILM FOR LEAD-FREE POWER GENERATOR 40

3.1 $BaTiO_3$ sol-gel synthesis 41

3.2 $BaTiO_3$ thin film characterization 44

3.2.1. Effect of annealing temperature and time on ferroelectric property 44

3.2.2. $BaTiO_3$ thin film with sub surface treatment using oxygen plasma 46

3.2.3. (111) oriented crack free $BaTiO_3$ thin film with PVP 49

3.2.4. Effect of BT sol-gel synthesis temperature on Ferroelectric property 52

4. FABRICATION OF MEMS ENERGY HARVESTING APPLICATION USING LEAD FREE BARIUM TITANATE THIN FILM 55

4.1 Selection of electrode design and cantilever beam layout.......................................55

4.2 Resonance frequency of cantilever beam..56

4.3 Fabrication process design...58

4.3.1 Etching feasibility test of barium titanate polycrystalline thin film.. 59

4.3.2. 500um Si wet etching feasibility test.............................. 61

4.3.3. 500um Si dry etching feasibility test with DRIE................62

4.4 Implementation of fabrication process.. 63

4.4.1. EH (Energy Harvesting) device fabrication step 1 and step 2... 63

4.4.2. EH (Energy Harvesting) device fabrication step 3 and step 4...64

4.4.3. EH (Energy Harvesting) device fabrication step 5 and step 6... 66

4.4.4. EH (Energy Harvesting) device fabrication step 7 and step 8...67

4.4.5. EH (Energy Harvesting) device fabrication final steps...69

4.5 Problems of fabrication process..70

4.6 Summary...72

APPENDIX

A. ATILA SIMULATION, THIN FILM SYNTHESIS, AND EH (ENERGY HARVESTING) MEMS DEVICE FABRICATION TOOL INFORMATION.. 73

B. FIRST DRAFT OF STANDARD ON VIBRATION ENERGY HARVESTING.. 86

REFERENCES 90

BIOGRAPHICAL INFORMATION.. 94

LIST OF ILLUSTRATIONS

Figure Page

1.1 Comparison of energy density for the three types of mechanical to electrical energy converter………………………………………………..… 2

1.2 Equivalent circuits for measuring voltage and power…..………………… 6

1.3 Block diagram for the energy harvesting circuit…………………………… 7

1.4 I-V curve of diode…………………………………………………………… 8

1.5 (a) Bridge rectifier circuits, (b) raw & rectified signal……………………….. 8

1.6 Buck converter……………………………………………..……………….. 9

1.7 Relationship among the piezoelectric, pyroelectric and ferroelectric Material...…….................. 12

1.8 Unpoled and poled ferroelectric domain orientations (Copyright: APC international, Permission granted by R. STaut)......…….. 12

1.9 Typical hysteresis curves for a ferroelectric ceramics (Data source: B. Jaffe, W. R. Cook, and H. Jaffe, Piezoelectric Ceramics 1971)…………………………………………………………………13

1.10 Phase transition and related changes in properties for $BaTiO_3$ with temperature (a) crystal structure (b) lattice spacing, and (c) spontaneous polarization (Data source: B. Jaffe, W. R. Cook, and H. Jaffe, Piezoelectric ceramics 1971) ……………………………..…………..….......14

1.11 Commercialized energy harvesting devices (a) MIDE http://www.mide.com/products/volture/volture_catalog.php
(b) POWERCAST http://powercastco.com/
(c) PMG Perpetuum http://www.perpetuum.co.uk/
(d) FERRO Solutions http://www.ferrosi.com/products.html
(d) Hi-Z technology, INC. http://www.hi-z.com/
(e) MicroStrain http://www.microstrain.com/
(f) Cedrat http://www.cedrat.com/en/technologies/mechatronic-systems/
(g) KCF Technologies http://www.kcftech.com/…………....……………….. 16

1.12 (a) Anisotropic etching (Reprinted with permission from AACHBOUN et al.,Copyright 1999, American Vacuum Society) (b) Isotropic etching (Reprinted with permission from IOP publishing, @2005)…………………………………………..………………………… 22

1.13 (a) d_{33} mode energy harvesting device(Used with permission from Elsevier, License No: 1971191064688) (b) d_{31} mode energy harvesting(Used with permission from Elsevier, License No:197190704094)... 25

1.14 (a) SEM image of front side and (b) back side of energy harvesting device of embedded Si proof mass(Reprinted with permission from Shen et al., Copyrihgt:IOP publishing, 2008).……………….…………25

1.15 Plot of power density as a function of excitation ratio for various mechanical to electrical energy conversion devices reported in literature.. 27

2.1 Laser machined cantilever beam (SEM picture)…………………................30

2.2 Laser machined cantilever beam (optical picture) …………………........... 31

2.3 Schematic of side view of stacked wafer.. 31

2.4 Assembled energy harvesting device... 32

2.5 Mounted EH device on the shaker……………………………….………… 33

2.6 Oscilloscope for the acceleration (top) measurement and lock-in amplifier for voltage………………………………………………………….……… 33

2.7 Shaker (Left) and amplifier (Right)…………………………...................... 34

2.8 Output voltage(Vrms) in the open circuit condition as a function of frequency for the fabricated energy harvesting in two different mounting conditions... 35

2.9 Impedance spectrum of the PZT wafer before and after laser machining. After laser machining the wafer was mounted onto chip package and wire bonded for measuring the spectrum. FEM Simulation was conducted on the laser machined wafer attached to package…………………………………………………………….……36

2.10 Schematic depiction of the buckling of the chip package under the loading of the aluminum bar(exaggerated) (a) Initial state and (b) Final state.. 37

2.11 (a) Variation of the output power & voltage as a function of load at frequency of 870Hz under 8g acceleration (b) Variation of the output power & voltage as a function of load at frequency of 270Hz under 8g acceleration... 38

3.1 PVP (Polyvinylpyrrolidone)………………..42

3.2 Barium titanate solution synthesis flow chart... 42

3.3 (a) TGA and DSC of the barium titanate solution, (b) XRD pattern after test(Data measured after heating the solution for 4hrs at 100°C)... 43

3.4 (a)Temperature dependence of dielectric constant with 5mins crystallization time
(b) Temperature dependence of resistivity with 5mins crystallization time (c) Crystallization time dependence of c/a ratio at 850°C
(d) Temperature dependence of polarization with 5mins crystallization time(at 1Khz)... 45

3.5 Process flow of the barium titanate thin film deposition and crystallization... 46

3.6 (a) Top view (Crack free) batch No 1
(b) Top view (Crack free) batch No 2
(c) Side view (Crack free)……... 48

3.7 XRD of (111) preferred orientation seed layer…………………..……….. 50

3.8 XRD of (111) preferred orientation 600nm thickness Barium titanate thin film………... 51

3.9 SEM tilt view of crack free 600nm $BaTiO_3$ thin film……………………...... 51

3.10 Dielectric constant vs frequency (Hz) at 1V…………………………………. 52

3.11 Loss tangent vs frequency (Hz) at 1 V.. 53

3.12 P-E loop of BT thin film from 130°C initial synthesize temperature........... 53

3.13 SEM image of BT thin film with 130°C initial synthesis temperature (a):top view; inset shows the XRD peak of BT thin film and side view…………………………………………………………..…….. 54

4.1 Designed devices: (a) Layout of six micro cantilever energy harvesting beams, (b) lay out of 4” wafer, and (c)close up of a d_{33} mode cantilever beam... 56

4.2 Neutral axis of the each layer of the cantilever beam................................ 58

4.3 Designed EH MEMS fabrication process flow: (a) barium titanate deposition using sol-gel, (b) lithography, (c) Au/Cr IDT deposition & Lift-off, and (d) Wet etch of BT film with 2% HF & Si DRIE, (e) Thermal SiO_2 DRIE & Si etch with KOH or Si etch with DRIE, (f) SiO_2 dry etching using RIE, and (g) Wire bonding, tip mass attach & poling………………………………….......................................59

4.4 Profile of surface after RIE with Ar/CF_4/O_2 gas mixture (150W)................ 60

4.5 Optical microscopy after front side wet etching with 2% HF.................... 61

4.6 30wt% KOH etching rate of (100) Si
(Reproduced with permission from electrochemical society)................... 61

4.7 Optical microscopy after 500µm Si backside etching
with 30 wt% KOH………………………………………………….................. 62

4.8 Working principle of the DRIE process... 63

4.9 Backside of the energy harvesting device after DRIE process................. 63

4.10 Schematic of fabrication process: (a) step 1 (BT deposition using
Sol-gel method on top of the 4 inch SOI wafer & (b) step 2
(Cr/Au IDT electrode deposition on top of BT layer after
lithography process), and (c) EH wafer after the Cr/Au top
electrode deposition……………………………………............................. 64

4.11 Schematic of process: step 3 (Photoresist deposition
and lithography) & 4 (Barium titanate wet etching with 2% HF and
Si device layer etching with DRIE)…………….. 65

4.12 EH wafer after step 3 & 4.. 65

4.13 Schematic fabrication process flow step: 5 (PECVD SiO_2 deposition
on the backside of the wafer) & 6 (SiO_2 hard mask pattern)..................... 66

4.14 Patterned backside of the EH wafer.. 67

4.15 Schematic of process flow step: 7 (Backside 500µm thickness
Si DRIE) & 8 (cantilever beam release by removing SiO_2 Layer with
DRIE)………………………………….. 67

4.16 Energy harvesting device after laser wafer saw process (Front side)........ 68

4.17 SEM image of the cantilever beam (Front side)... 68

4.18 (a) Top view of released cantilever beam, and
(b) Tilt view of released cantilever beam …... 69

4.19 Packaged EH device..…………………………….………………………….……69

4.20 Backside mask mis-aligned device……………………………………………70

4.21 Damaged BT film on the SOI wafer by exposure to KOH solution…..…….71

4.22 Peeling of wire bonding pad by wire bonder capillary……………………… 71

LIST OF TABLES

Table Page

1.1 Examples of vibration sources.. 3

1.2 Magnitude of acceleration and frequency for common sources...............3

1.3 Summary of the prototypic devices available commercially........................17

1.4 Compilation of the power density and operating condition for various mechanical energy harvesting devices.. 26

3.1 Piezoelectric properties of lead free piezoelectric candidates................ 41

3.2 Experiment table for the plasma and spin coating condition.................... 47

4.1 Dimension of micro cantilever beams... 57

CHAPTER 1

INTRODUCTION

Increasing research in the area of small wireless electronic devices such as wireless sensor networks to monitor building and military applications[1] has prompted re-evaluation of powering technology. Such sensor networks utilize low power wireless nodes based on VLSI (Very Large Scale Integration) technology[2]. The drop in power requirement over the years has brought us to the point where one can start thinking of "self-powered electronics" by continuously harvesting energy from the environmental sources. Currently, energy harvesters are deployed in various forms including the use of mechanical transducers in sport equipment including tennis racquets and skis where strain is used to power actuators for feedback control loops, also body motion is used to drive watches. In this thesis, the main goal was to fabricate micro-scale mechanical energy harvesting devices that can be easily integrated with wireless sensor nodes. To achieve this goal, laser micromachining and MEMS (Micro-Electromechanical System) approach was adopted to fabricate piezoelectric material based harvesters.

Piezoelectric transducers are most suitable as mechanical to electrical energy converters. In addition to the advantage of being smaller and lighter the piezoelectrics have three times higher energy density as compared to their counterparts electrostatic and electromagnetics. Figure 1.1 compares the magnitude of energy density for three types of converters. In this figure, the symbol ε is the dielectric constant, E is the electric field, B is the magnetization, X is the stress, d is the piezoelectric strain constant and g is the piezoelectric voltage constant. This figure shows that piezoelectric has energy density in the range of 15 –

20 mJ/cm^3. This magnitude can be further enhanced by incorporating newly developed high performance piezoelectric materials.

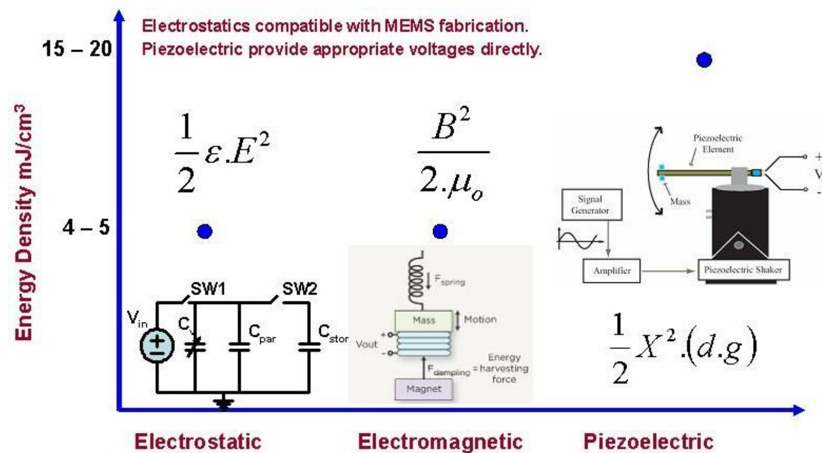

Figure 1.1: Comparison of the energy density for the three types of mechanical to electrical energy converters.

1.1 Mechanical Vibration Sources

Mechanical vibration sources can be categorized as continuous, impulsive and intermittent. A continuous vibration source refers to the condition where amplitude is constant with time. Impulsive vibration source (such as in shocks) refers to the condition where amplitude of each event reaches the peak and then decays sharply. An intermittent vibration source refers to the condition where amplitude is varying with time. Among these different types of sources, the most attractive one for energy harvesting is continuous vibration with high acceleration. Examples of typical vibration sources are listed in Table 1.1:

Table 1.1: Examples of vibration sources[3]

Continuous vibration	Impulsive vibration	Intermittent vibration
Industrial machinery, steady road traffic, construction activity, manufacturing assembly lines, water flow, breeze, human walking motion.	Occasional drop of heavy equipment, occasional loading and unloading, shock waves, impact machines on the oil drilling sites, pipelines near heavy traffic, acoustic noise.	Trains, passing heavy vehicles, forging machines, impact pile driving, jack hammers, highway traffic in tunnel, bag pack motion, waist pouches.

Table 1.2 shows the magnitude of peak frequency and acceleration for various common vibration sources.

Table 1.2: Magnitude of acceleration and frequency for common sources[4,5]

Vibration source	**Acceleration (m/s^2)**	**Peak Frequency (Hz)**
Car engine compartment	12	200
Base of 3-axis machine tool	10	70
Blender casing	6.4	121
Clothes dryer	3.5	121
Person nervously tapping their heel	3	1
Car instrument panel	3	13
Door frame just after door closes	3	125
Small microwave oven	2.5	121
HVAC vents in office building	0.2-1.5	60
Windows next to a busy road	0.7	100
CD on notebook computer	0.6	75
Second story floor of busy office	0.2	100

One of the most commonly available and attractive source of mechanical energy is human. Resonance frequency of human body is in the range of 4 to 200 Hz [6] with acceleration of approximately 2 g (where g = 9.8 m/s^2) when human walk normally on a tread mill at constant speed of 4 km/h.[7]

1.1.1 Power spectral density (PSD) curve

Random vibrations contain excitation of various frequencies within the specified frequency band. In order to characterize the random vibration, a log-log plot of g_d^2/Hz (y-axis; where g_d is the input acceleration) as a function of frequency in Hz (x-axis) is constructed (power spectral density (psd) curve). The square root of the area under the curve represents the root mean square (rms) of the acceleration (g_{rms}):

$$\sqrt{Area} = \sqrt{\frac{g_d^{\ 2}}{Hz} x\, Hz} = g_{rms} \tag{1}$$

The spectral density curves can also be plotted in units of decibels (dB) as:

$$dB = 10\log\frac{g_d^{\ 2}/f}{g_d^{\ 2}r/f} = 20\log\frac{g_d/\sqrt{f}}{g_r/\sqrt{f}} \tag{2}$$

where g_dr/f is a given reference value of power spectral density, usually the maximum specified value. Overall acceleration level for a flat PSD curve can be given as

$$g_{rms} = \left[(f_2 - f_1)g_d\right]^{1/2} \tag{3}$$

Bands of spectra with non-flat, but straight line (log-log), acceleration density characteristics can substitute the following equation for overall acceleration

$$g_{rms} = \left[(\frac{g_1}{g_2})\frac{f_2^{\ s+1} - f_1^{\ S+1}}{S+1}\right]^{1/2} \tag{4}$$

where g_{rms} is overall acceleration, f_1 and f_2 is band frequencies, g_1 and g_2 is band limit levels, and S is $\log(g_2/g_1)/\log(f_2/f_1)$ or S is 0.3322(Db/oct). The displacement (D) can be found from the expression:

$$D^2{}_{rms} = 95.6\sum_{f1}^{f2} g_d \frac{\Delta f}{f^4} \tag{5}$$

1.2 Power estimation from spring mass system, Electrical Energy, and Energy harvesting

1.2.1 Power estimation from spring mass system

The general model for conversion of vibration energy into electrical energy was developed by Williams and Yates[8]. The assumptions in this model are that the mass of vibration source is much greater than the seismic mass of generator and that the vibration source is an infinite source of power. The second order differential equation describing the system with housing vibration and relative motion of mass is given as:[9]

$$m\ddot{z}(t) + c_p\dot{z}(t) + k_s z(t) = -m\ddot{y}(t) \tag{6}$$

where m is the seismic mass, c is the damping constant and k is the spring constant. The total power dissipated in the damper under sinusoidal excitation can be expressed as:[10]

$$P(\omega)\frac{m\varsigma Y_o^{\,2}(\frac{\omega}{\omega_h})^3\omega^3}{\left[1-\left(\frac{\omega}{\omega_n}\right)^2\right]+\left[2\varsigma\left(\frac{\omega}{\omega_n}\right)^2\right]} \tag{7}$$

where ω^2_n=k/m is the system resonance frequency and ζ is the damping ratio. If we assume that the vibration frequency and resonance frequency are identical then maximum power can be obtained as:

$$P_{\max} = \frac{mY_o^{\,2}\omega^3{}_n}{4\varsigma} \tag{8}$$

1.2.2 Simple equivalent circuit model

The load dependence of piezoelectric generator can be computed by using the equivalent circuit representation shown in Figure 1.2. This equivalent circuit is only valid in the frequency range far from the resonance.[11] In this circuit the voltage source is taken as the open circuit voltage across the piezoelectric generator. The voltage across the load can then be expressed as:

$$V_{Load} = V_{OC}\left|\frac{R_{Load}}{R_{Load} + \frac{1}{j\omega C} + R_S}\right| \quad (9)$$

where R_S is the series resistance and C is the damped capacitance of the piezoelectric transducer. The equivalent circuit parameters can be determined from the impedance analyzer HP 4194A. The average power delivered to the load can then be found using the expression:

$$P = \frac{V_{Load}^2}{2R_{Load}} \quad (10)$$

The power reaches maximum at an optimum load (R_{Load}^{opt}) which for the equivalent circuit shown in Fig. 1.2 is given as:

$$R_{Load}^{opt} = \left|R_S + \frac{1}{j\omega C}\right| \quad (11)$$

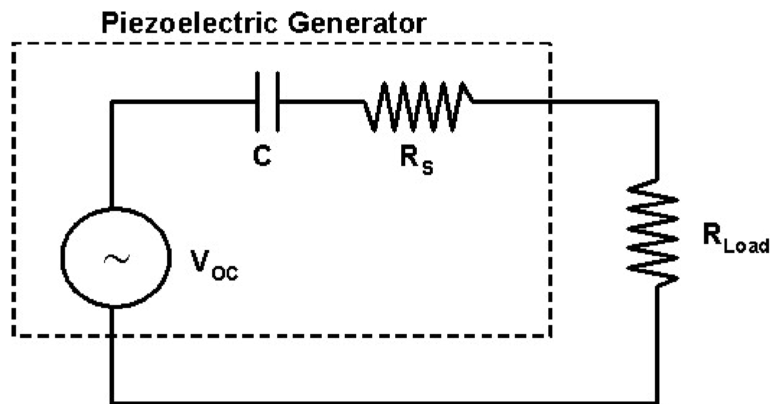

Figure 1.2: Equivalent circuits for measuring voltage and power

1.2.3 Energy density of capacitor

Energy stored in a capacitor is given by Eq. (12) as:

$$U = \frac{q^2}{2C} = \frac{1}{2}CV^2 \quad (12)$$

where U is the energy stored in a capacitor, C is capacitance, q is charge, and V is voltage. Energy density, u, is defined as:

$$u = \frac{Potential\,energy}{Volume} = \frac{1}{2}\frac{CV^2}{Ad} = \frac{1}{2}\varepsilon\varepsilon_o(\frac{V}{d})^2 = \frac{1}{2}\varepsilon\varepsilon_o E^2 \qquad (13)$$

where A is the area of capacitor, d is distance between electrodes, ε is permittivity of medium, ε_o is permittivity of free space, and E is electrical field.

1.3 Energy Harvesting Circuit

A simple energy harvesting circuit consists of a diode rectifier (AC/DC) and a DC-DC converter, as shown in Fig. 1.3. The addition of DC-DC converter has been shown to improve energy harvesting by a factor of 7. The efficiency of the step-down converter was between 74 to 88%. Through the exploitation of discontinuous conduction mode operation of the DC-DC converter, a stand-alone energy harvesting system with significantly simplified control circuitry has been proposed.[12]

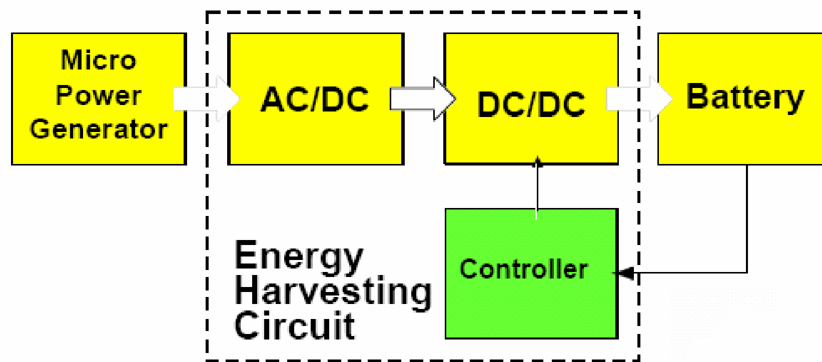

Figure 1.3: Block diagram for the energy harvesting circuit.

1.3.1 Rectification (AC / DC conversion)

A diode allows current to flow in only one direction and currents is blocked in other direction. Figure 1. 4 shows the I-V curve of diode.

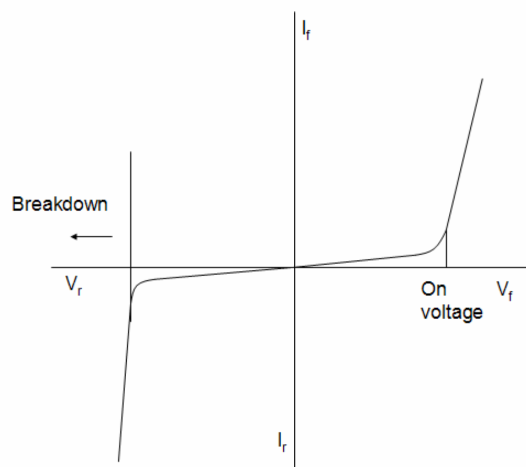

Figure 1.4: I-V curve of diode

A bridge rectifier makes use of four diodes to achiever full wave rectification. This is a widely used configuration both with individual diodes wired as shown in Fig. 1.5 and with single component bridges where the diode bridges are wired internally. The voltage drop across the Si diode at room temperature is of the order of 30%. Figure 1.5 (a) & (b) shows the full bridge rectifier and rectified signal output.

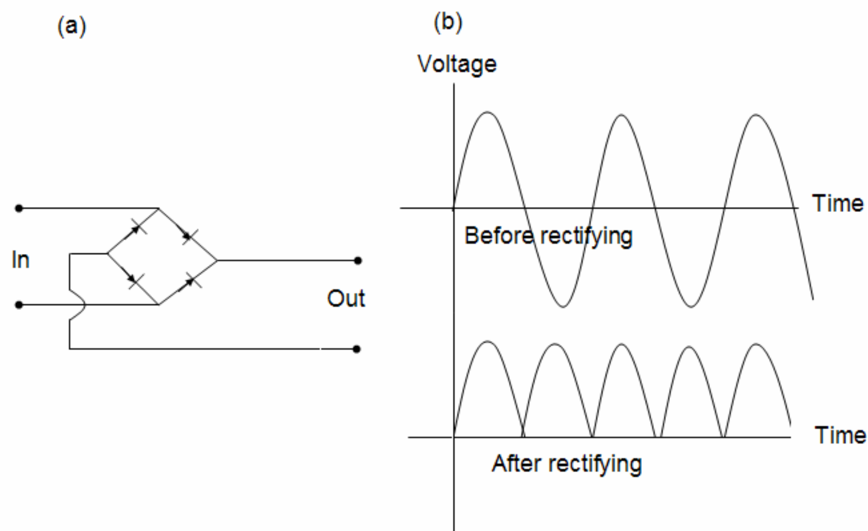

Figure 1.5: (a) Bridge rectifier circuits (b) raw & rectified signal

1.3.2 Filter capacitor

Capacitors are used to smooth the voltage of DC signal. Required capacitance for smoothing output voltage can be calculated from Eq. (14) as:

$$C = \frac{i_L T}{2V_r} \tag{14}$$

where i_L is average load current, T is time period of input voltage, and V_r is peak to peak regulated voltage.

1.3.3 Buck converter (Step down): A simple description of DC/DC Conversion

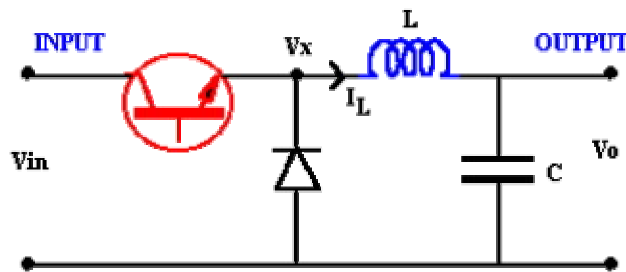

Figure 1.6 Buck converter

In order to know the voltages in this circuit we should consider the changes in inductor current over one cycle. From the relation:

$$V_\chi - V_0 = L\frac{di}{dt} \tag{15}$$

The change of current satisfies Eq. (16)

$$di = \int_{ON} (V_X - V_O)dt + \int_{OFF} (V_X - V_O)dt \tag{16}$$

In steady state operation, the current at the start and end of a period T will not change. In order to get a simple relation between voltages, we assume that there is no voltage drop across

transistor or diode while being ON. Thus during the ON time V_X=V_{in} and in the OFF time V_X=0.

Thus,

$$0 = d_i = \int_0^{t_{ON}} (Vi_n - V_o)dt + \int_{t_{ON}}^{t_{ON}+t_{OFF}} (-V_O)dt \tag{17}$$

This simplifies to

$$(Vi_n - V_o)t_{ON} - V_O t_{off} = 0 \tag{18}$$

or

$$\frac{V_O}{V_{in}} = \frac{t_{ON}}{T} \tag{19}$$

The “duty cycle” is given as:

$$D = \frac{t_{ON}}{T} \tag{20}$$

Thus, the voltage relationship becomes V_O=D V_{in} since the circuit is lossless and the input and output power must match on the average V_0 x I_O = V_{in} x I_{in}. Thus, the average input and output current must satisfy I_{in}=D $I_{O.}$

1.3.4 *Energy storage in a capacitor*

If we assume energy harvesting device can generate 8 A and 12 V, then power will be 8 A x 12 V= 96 W. The required energy capacity for the capacitor is 96 W x 2 seconds = 192 J. From this, we can calculate capacity which is need for the capacitor as C = $2E_{store}/V^2$ = 2 x $(192)/12^2$ = 2.67 F. Since the commercial capacitors have limitation of 2.5 V, 5 capacitances in series are required to get the needed voltage of 12V:

$$C = \frac{1}{\frac{1}{C} + \frac{1}{C} + \ldots \frac{1}{C}} = \frac{C}{n} = \frac{C}{5} \tag{21}$$

1.4 Piezoelectric Materials

1.4.1 Piezoelectricity

An excellent review of piezoelectric crystals and ceramics has been conducted by Jaffe[14]. Piezoelectric effect was discovered by Pierre and Jacques Curie in 1880. It is observed in non-centro symmetric crystals which have dipole moment. There are thirty-two point groups, of which twenty-one are non-centrosymmetric. Out of these 21 non-centrosymmetric groups, twenty exhibit direct piezoelectricity (leaving point group 432). The direct piezoelectric effect implies generation of charge due to application of mechanical stress. The converse piezoelectric effect implies generation of stress or strain due to application of an electric field.

Piezoelectric effect is defined as a linear relationship between a mechanical variable (strain S or stress T), and an electric variable (electric field E or electric displacement D) as following[13]:

$$D_i = d_{ijk} T_{jk} \quad (22)$$

where d_{ijk} is the piezoelectric charge constant or piezoelectric strain coefficient. The converse piezoelectric effect is expressed as[13]:

$$S_{ij} = d_{kj} E_k \quad (23)$$

where S_{ij} is the strain developed in material under the applied electric field E_k. For a given composition, piezoelectric constant d_{kij} is numerically identical for both the direct effect (C/N) and converse effect (m/V).

A subclass of piezoelectric materials is pyroelectric materials that can be spontaneously polarized. Pyroelectric materials have a unique polar axis in the unstrained condition. In quartz crystal, the dipoles are arranged in several compensating directions such that no net charge is observed when material is subjected to uniform heating. $PbTiO_3$ and (Ba, Sr) TiO_3 are typical examples of pryoelectric materials[14].

Ferroelectric materials are subclass of pryoelectric materials that exhibit reverse polarization on application of an electric field in the opposite direction[13]. Figure 1.7 shows the relationship between piezoelectric, pyroelectric, and ferroelectric materials.

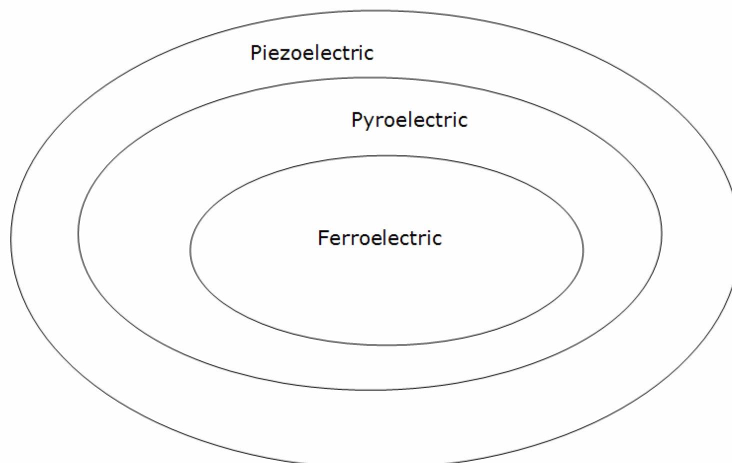

Figure 1.7: Relationship among the piezoelectric, pyroelectric and ferroelectric material

PZT (Lead zirconate titanate) and BT (Barium titanate) are good examples of commonly used piezoelectric ceramics. In the as-deposited state, the domains in piezoelectric materials are randomly oriented cancelling the net polarization. However, if an electric field of enough strength (higher than coercive field) is applied to the thin film, the dipoles reorient themselves in the direction of the field and the film exhibits net polarization as shown in Figure 1.8. Poled ceramics are used in several applications such as force or displacement sensors, ultrasonic motors and various actuators that require precise positioning and manipulation[15].

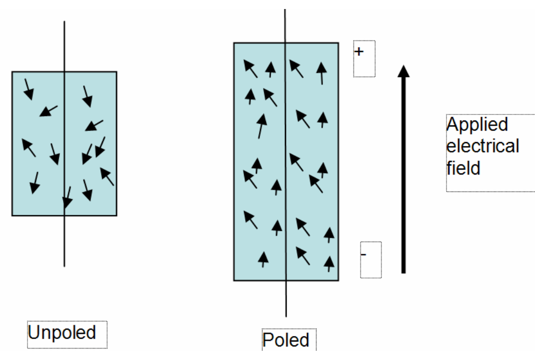

Figure 1.8 Unpoled and poled ferroelectric domain orientations (Copyright: APC international, Permission granted by R. Staut) [15]

Figure 1.9 shows a typical dielectric displacement versus applied electrical field hysteresis loop[16].

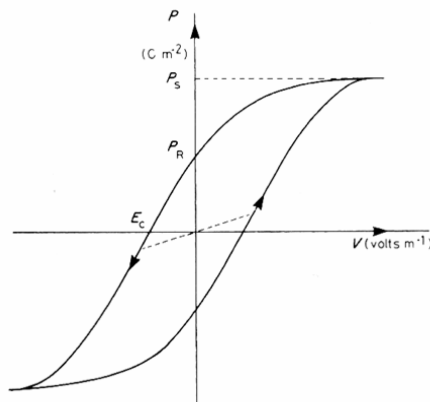

Figure 1.9 Typical hysteresis curves for a ferroelectric ceramics (Data source: B. Jaffe, W. R. Cook, and H. Jaffe, Piezoelectric ceramics 1971[16]).

Piezoelectric ceramics loses its spontaneous polarization and piezoelectric characteristics in the paraelectric state which occurs beyond the Curie temperature (T_c) generally characterized by the maximum in dielectric constant. Above T_c, piezoelectric ceramic material is cubic and the central cation in perovskite lattice shows no net displacement. Above Curie temperature, the dielectric constant follows the Curie behavior given as[17]:

$$\varepsilon_r = C/T\text{-}To \qquad (24)$$

where C is Curie constant, T is absolute temperature (K), and T_o is the Curie-Weiss temperature (K). The transition from ferroelectric to paraelectric phase and corresponding changes in crystal structure and properties for $BaTiO_3$ ceramics are shown in Fig 1.10.

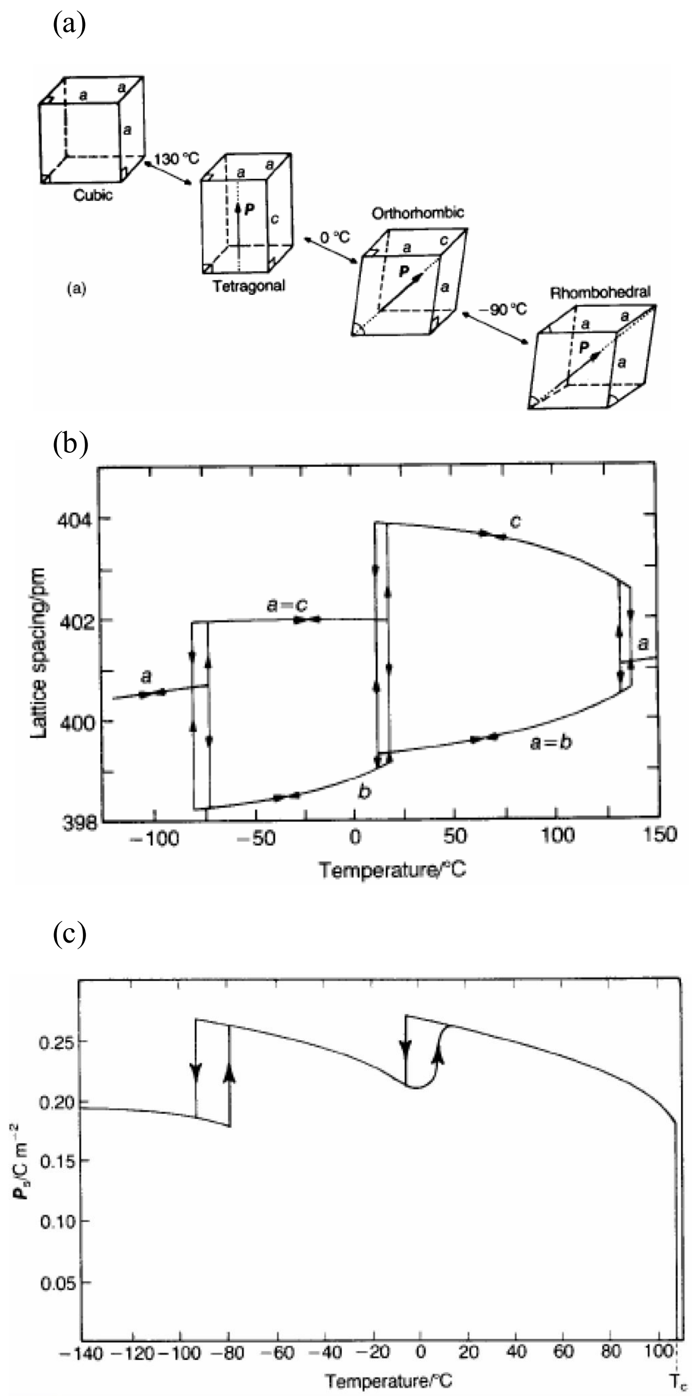

Figure 1.10 Phase transition and related changes in properties for $BaTiO_3$ with temperature (a) crystal structure (b) lattice spacing, and (c) spontaneous polarization [Data taken from: Piezoelectric Ceramics, B. Jaffe, W. R. Cook, and H. Jaffe, 1971][18].

1.4.2 Electromechanical factors

The important parameters of piezoelectric materials for energy harvesting are high piezoelectric charge constant (d, C/N), high piezoelectric voltage constant (g, Vm/N), high elastic compliance (s, m^2/N), and a high electromechanical coupling factor (k). The piezoelectric charge constant, d, is defined as charge generated per unit of applied mechanical stress or the mechanical strain generated per unit applied electric field. A material which has a higher piezoelectric charge constant can generate higher electric field. The piezoelectric voltage constant is the electric field generated by a piezoelectric material per unit of applied mechanical stress. Elastic compliance is reciprocal of the modulus of elasticity or Young's modulus. Electromechanical coupling factor is indicator of the effectiveness with which a piezoelectric material converts electrical energy into mechanical energy, or mechanical energy into electrical energy. Under static or near-static conditions (input frequencies far below the resonance frequency), either electrical to mechanical or mechanical to electrical conversion can be expressed as[19]:

$$k^2 = \text{converted energy / input energy} \quad (25)$$

In tensor form, the coupling coefficients of poled ceramics for longitudinal, transversal, and shear mode are[20]:

$$k_{33}^{\ 2} = d^2{}_{33} / S^E{}_{33}\varepsilon^T{}_3 \quad (26)$$

$$k_{31}^{\ 2} = d^2{}_{31} / S^E{}_{11}\varepsilon^T{}_3 \quad (27)$$

$$k_{15}^{\ 2} = d^2{}_{15} / S^E{}_{44}\varepsilon^T{}_1 \quad (28)$$

where ε^T is the dielectric permittivity of given material at constant stress, d is the piezoelectric charge constant, and S is the strain.

1.5 Current status of piezoelectric macro-generators

Several commercial prototypes of mechanical energy harvesting devices have been launched in this decade as summarized in Table 1.3. Perpetuum has introduced electric energy generator series using electromagnetic mechanism (PMG)[21]. PMG devices can generate 0.1~0.4 mW power at 25 mg acceleration and 2~5 mW at 100 mg acceleration. Ferro solution has also demonstrated energy harvester based on electromagnetics[22] that can generate 0.4 mW at 20mg and 9.3 mW at 100 mg acceleration. Cedrat's APA400M-MD utilizes amplified piezoelectric actuators (APAs) to generate 40 mW power at 110 Hz.[23]. MIDE' Volture is based on Quickpack piezoelectric actuators that can generate 1mW power at 240 mg acceleration and 120 Hz resonance frequency[24]. Figure 1.11 shows pictures of the commercialized products (downloaded from the respective company websites).

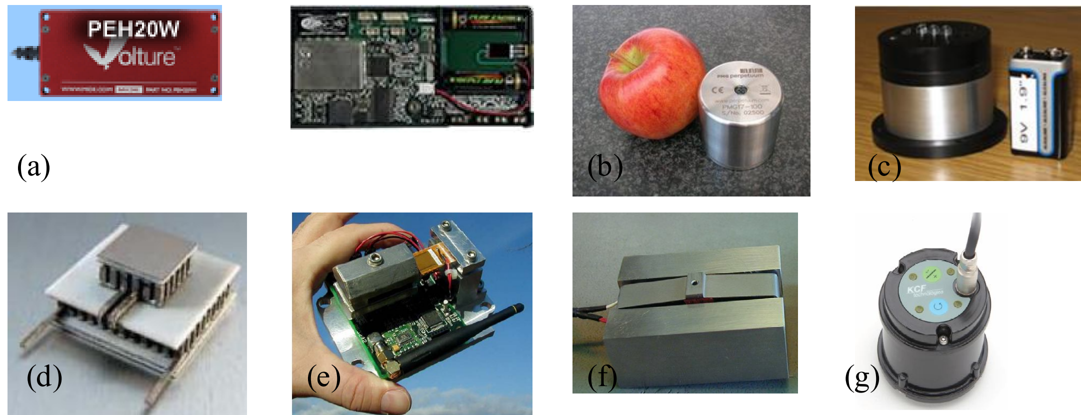

Figure 1.11 Commercialized energy harvesting devices[32~41] (a)MIDE http://www.mide.com/products/volture/volture_catalog.php (b) POWERCAST http://powercastco.com/ (c) PMG Perpetuum http://www.perpetuum.co.uk/ (d) FERRO Solutions http://www.ferrosi.com/products.html (d) Hi-Z technology, INC. http://www.hi-z.com/ (e) MicroStrain http://www.microstrain.com/ (f) Cedrat http://www.cedrat.com/en/technologies/mechatronic-systems/ (g) KCF Technologies

Table 1.3: Summary of the prototypic devices available commercially [21, 22,23,24,25]

Commercial vendor	Conversion mechanism	Power or Current	Volume (mm)	Frequency	Acceleration
MIDE	Piezoelectric	8 mW	92.7 x 43.8 x 9.9	50 Hz	1 g
Perpetuum	Electromagnetic	0.1~0.4 mW	26.6 Φ x 23	NA	100 mg
Ferro solutions	Electromagnetic	0.4 mW	45.7 Φ x 45.7	NA	20 mg
Powercast	Electromagnetic	98.9 ~ 694.6 μW	5.08 x 2.54 for WPT, 2.54 x 1.27 for WPR	2.4 GHz ~ 905.8 MHz	NA
HiZ Technology	Thermal energy harvester	300 mW	29 x 29 x 5.1	NA	NA
Kryotherm	Thermal energy harvester	485 μW	30 x 30 x 3.6	NA	NA
Microstrain	Piezoelectric	~ 2.8 mW	50 mm length	~60 Hz	NA
Smart material	Piezoelectric	500 V_{DC}	28 x 14 x 3 ~ 85 x 57 x 3	< 10 kHz	NA
Cedrat	Piezoelectric	95 mW	50 x 32 x 22	110 Hz	NA
KCF Technologies	Piezoelectric	0.3 ~4.1 mW	63 Φ x 76mm	58~374 Hz	0.2~2.6g

1.6 Laser micro-machining

Several applications have been reported in literature for femto second laser ablation. Gattass and Mazur have demonstrated laser ablation of transparent materials using femtosecond laser[42] for nano surgery, material processing and micro fluidic devices. Xia and Tu[43] have investigated processing of 3D micro or nanostructures. Uppal et al.[44] have demonstrated laser micro machining of PZT and proposed the rapid prototyping of PZT based 3D micro components and devices.

Beam width is the most important parameter for laser beam profile used in micromachining[42]. In optics, a Gaussian beam is electromagnetic radiation whose transverse electric field and intensity distributions are described by Gaussian function. The Gaussian distribution of laser power intensity $P_{x,y}$ at location (x, y) is given by[43]

$$P_{x,y} = \frac{2P_{tot}}{\pi r^2_b} \exp(-\frac{2r^2}{r^2_b}) \tag{29}$$

where $r=(x^2+y^2)^{1/2}$ is the distance measured from the laser beam center and r_b is the laser beam radius; $P_{tot}=nP_{incident}$, where P_{tot} is the total absorbed power, $P_{incident}$ is the incident laser power, and n is the average absorption of the work piece material. The diameter of the damaged area, can be calculated by using the following expression:[44]

$$D^2 = 2\omega_o^2 \ln(\frac{F_i}{F_{TH}}) \tag{30}$$

where D is the spot diameter of damage, F_i is the peak value, F_{th} is the threshold fluence, and ω_0 is $1/e^2$ of beam radius. The beam spot size, $2\omega_o$ of the focused beam is calculated by using following expression[44]:

$$2\omega_o = (\frac{4\lambda}{\pi})(\frac{f}{D_u}) \tag{31}$$

where λ is the laser wavelength, f is the focal length of the focusing lens, and D_u is the beam diameter of the unfocused laser beam.

1.7 Principle of Sol- Gel synthesis

$BaTiO_3$ thin films can be deposited by several methods such as RF magnetron sputtering[45] , PLD (Pulsed Laser Deposition)[46], MOCVD (Metal-Organic chemical vapor deposition)[47], hydrothermal[48], and CSD (Chemical Solution Deposition)[49,50,51,52] Among these different techniques, CSD can provide stoichiometric and textured thick films. This process is inexpensive relative to other methods. There are several routes for synthesizing deposition solution. Most of these methods for titanates use non-aqueous systems due to the rapid hydrolysis of titanium precursor with water and condensation of alkoxide agents as shown by chemical reactions below[53]:

Hydrolysis:

$$M(OR)_n + H_2O \rightarrow M(OR)_{n-1}(OH) + ROH \tag{32}$$

Condensation (water elimination):

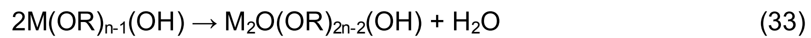

$$2M(OR)_{n-1}(OH) \rightarrow M_2O(OR)_{2n-2}(OH) + H_2O \tag{33}$$

Condensation (alcohol elimination):

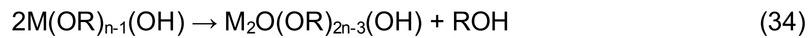

$$2M(OR)_{n-1}(OH) \rightarrow M_2O(OR)_{2n-3}(OH) + ROH \tag{34}$$

Hydrolysis is the reaction of water molecule with alkoxide, resulting in formation of a hydroxyl metal alkoxide ($M(OR)_{n-1}OH$) and alcohol molecule (ROH). Condensation is reaction of two hydroxyl metal alkoxides to form a polymeric species with metal-oxygen-metal (M-O-M) bonds. The degree of hydrolysis reaction can be controlled by controlling the amount of water added for hydrolysis[54]. For a general sol-gel process, the hydrolysis reaction occurs readily and precipitation of hydroxide species may occur. To avoid this problem, dry chemical and inert

atmosphere are required for synthesis of solution and to minimize the reaction between Titanium iso-propoxide and moisture[55]

.

1.8 Textured piezoelectric thin film

Textured piezoelectric thin film can be synthesized by promoting heterogeneous nucleation. Generally, heterogeneous nucleation occurs at the film/substrate interface while homogeneous nucleation initiates inside of the film[56]. The energy barriers for homogeneous and heterogeneous nucleation ΔG* and their dependence on the driving force ΔG_V, can be described as[57]:

$$\Delta G^*_{\hom o} = \frac{16\pi r^3}{3(\Delta G_V)^2} \tag{35}$$

$$\Delta G^*_{hetero} = \frac{16\pi r^3}{3(\Delta G_V)^2} f(\theta) \tag{36}$$

Where γ is the interfacial energy and f(θ) is a function related to the contact angle, θ. For a hemispherical nucleus, f(θ) can be expressed as:[58]

$$f(\theta) = \frac{(2 - 3\cos\theta + \cos^3\theta)}{4} \tag{37}$$

The difference between homogeneous and heterogeneous nucleation is the surface energy, γ. Hence it is critical to minimize driving force ΔG_V and manipulate $f(\theta)$. There are two main factors to achieve textured films, namely (i) rapid crystallization at high temperature[59], and (ii) modification of surface contact angle.

1.9 Domain engineering

Domain engineered configuration is achieved by poling the oriented crystal along the direction different from that of spontaneous polarization direction[60]. In case of tetragonal 4mm crystal such as that of barium titanate at room temperature, there can be three orientations for

crystal cuts that can be easily obtained: $[111]_c$, $[101]_c$, and $[001]_c$ [61]. Wada et al.[62] have reported a longitudinal piezoelectric coefficient of 203 pC/N for barium titanate crystal oriented along (111) direction. This is two times higher than the single-domain value measured along the $<001>_c$ polar axis[63]. Yako et al.[64] have investigated longitudinal piezoelectric coefficient as a function of domain size. It was found that finer engineered domain configurations less than 10μm in size exhibited higher piezoelectric properties. Park et al.[65] have investigated piezoelectric properties of $BaTiO_3$ single crystal poled along [001] direction as a function of temperature and DC bias. <001> oriented orthorhombic $BaTiO_3$ crystals at 0°C showed d_{33} of 500 pC/N which is significantly larger than that of randomly oriented ceramics. This result indicates that by texturing the film along the non-polar direction, a large piezoelectric coefficient can be obtained.

1.10 Process flow for MEMS device

1.10.1 Etching process

Etching step has two important considerations: (i) remove desired material in a specific geometry, and (ii) specificity to a given material. Wet etching is generally chemical method using reagents such as KOH and NaOH. Wet etching can be isotropic or anisotropic depending upon the chemistry. Dry etching is physical method, for example, RIE (Reactive Ion Etching) and ion milling. This etching is generally anisotropic using reactive gases.

1.10.1.1 Anisotropic and isotropic etching

Anisotropic etching means that etch rate along x, y, and z axis is different, while isotropic etching refers to the case where etching rate is same along each direction. Figure 1.12 (a) and (b) illustrate the isotropic and anisotropic etching process.

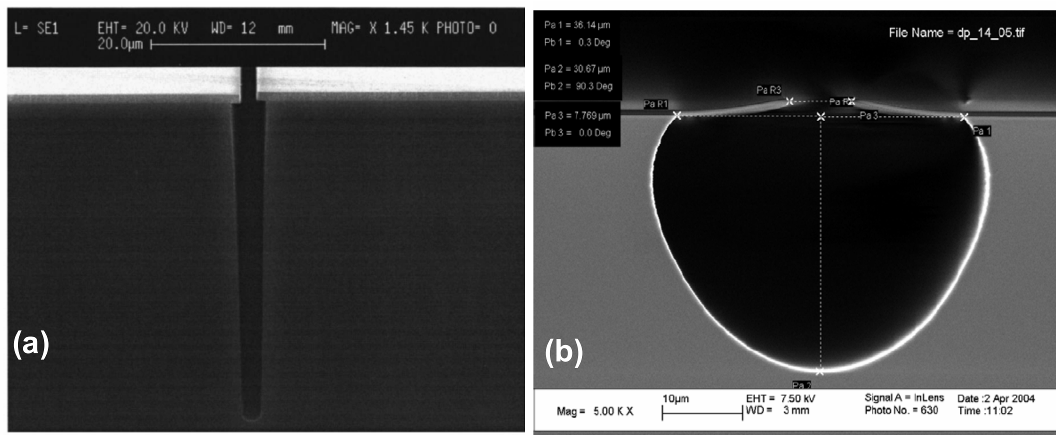

Figure 1.12(a) Anisotropic etching[66] (Reprinted with permission from AACHBOUN et al., Copyright 1999, American Vacuum Society) (b) Isotropic etching[67] (Reprinted with permission from IOP Publishing, @2005)

1.10.1.2 Wet etching and dry etching

Etching processes are generally characterized by three parameters; etch rate, selectivity, and uniformity. Etch rate is defined as the material thickness removed per unit time. Etch selectivity is a measure of how effective the process is in removing the specific material without affecting the surrounding. Quantitatively, etch selectivity can be expressed as the ratio between the etch rate of the material to be removed and mask materials on the wafer[68]. Wet chemical etching involves three steps; the reactants are transported by diffusion to the surface to be etched where chemical reactions take place. The reaction products are transported away from the surface by diffusion. Wet chemical etching of Si gives higher degree of selectivity in comparison to dry etching techniques[69]. Wet etching is faster with rate of a few microns to tens of microns per minute for isotropic enchants and about 1um/min for anisotropic enchant[70].

A large number of dry etch processes are available to pattern various materials. The process spectrum ranges from physical etching via sputtering and ion milling to chemical plasma etching. Two processes, reactive ion etching (RIE) and reactive ion beam etching (RIBE) combine aspects of both physical and chemical etching. In general dry etch processes utilize a plasma of ionized gases along with neutral particles to remove material from surface. Reactive ion etching is the most commonly used process to pattern Si using fluorinated

compounds such as CF_4, SF_6, and NF_3 or chlorinated compounds such as CCl_4 and Cl_2 mixed with He, O_2 or H_2 [74.] The RIE process is highly directional enabling direct pattern transfer from the masking material to the etched Si surface. The selection of masking material is dependent on the etch chemistry and desired etch depth. For MEMS applications, PR and SiO_2 thin films are often used. Si etch rates in RIE process are typically less than 1um/min, so dry etching is mostly used to pattern layers on the order of several microns in thickness.

1.10.2 Patterning or photolithography

Lithography is the process by which patterns are formed in a chemically resistant polymer deposited by spinning on to the silicon wafer[71]. A pattern transfer process is accomplished by using a lithography exposure tool that emits radiation. The performance of tool is determined by three properties; resolution, registration, and throughput. Resolution is defined as the minimum feature size that can be transferred with high fidelity to a resist film on the surface of wafer. Registration is a measure of how accurately patterns of successive masks can be aligned with respect to previously defined patterns on a wafer. Throughput is the number of wafers that can be exposed per hour for a given mask level. Depending on the resolution, several types of radiation including electromagnetic (e.g. ultraviolet and X rays) and particulate (e.g. electrons and ions) may be employed[72]. Optical lithography uses UV radiation (~0.2-0.4µm) with resolution of approximately 1µm[73]. The resolution of optical lithography is limited by diffraction, but this can be overcome by electron beam lithography where wavelengths of 0.2-0.5 angstroms are utilized[74].

1.10.3 Packaging

Packaging is the last stage in MEMS device fabrication. It comprises of several sequential processes. The first step is inspection and testing of wafer, followed by dicing of wafer, die attach, wire bonding, and sealing or molding. The role of packaging is to protect the sensor or device from external influences and environmental effects. Since MEMS inherently

include micro scale mechanical components, the integrity of device must be protected against physical damage arising from mechanical shock, vibration, temperature cycling, and particle contamination[75]. The electrical aspects of the device such as bond wires and electrical properties of interconnect must be protected against external influences and environmental effects. In addition to protecting the sensor, the packaging must prevent contamination in potentially sensitive environments. Importance of packaging can be found in medical devices consisting of sensors that will be implanted within the body.

1.11 MEMS (Micro-Electromechanical system) energy harvesting device

Previously, Jeon et al. have demonstrated MEMS based piezoelectric energy harvesting device[76]. The cantilever beam was formed from a membrane consisting layers of thermally grown or PECVD silicon oxide, silicon nitride and sol-gel deposited zirconium dioxide which acts as a buffer layer. The top PZT layer of thickness 0.58μm was deposited using a sol-gel process. The beam was released by undercutting the deposited films using a XeF_2 vapor etch. Figure 1.15(a) shows their fabricated energy harvesting device. The advantage of this device is the adoption of interdigitated Pt/Ti electrode utilizing d_{33} mode. This electrode configuration enables use of d_{33} and g_{33} coefficients of PZT. These coefficients are almost 2X higher than the d_{31} and g_{31} mode. The reported generator had a fundamental resonance frequency of 13.9 kHz generating power of 1.01 μW.

Fang et al.[77] have reported a MEMS based harvester with large tip mass utilizing d_{31} mode. The process started with wet thermal oxidation of SOI wafer followed by deposition of Ti/Pt layers using sputtering. PZT film of 1.64μm thickness was spin coated using sol-gel process. Next, Ti/Pt top electrode was sputtered and front side was patterned by wet etching (HF: HCl: H_2O=1:25:74) and RIE. In order to etch bulk Si, KOH was used. RIE process was utilized to release the composite cantilever beam. The final step consisted of attaching a tip mass made of nickel using glue. Figure 1.15(b) shows the fabricated cantilever beam. This device generated 2.16 μW power at the resonance frequency of 608Hz.

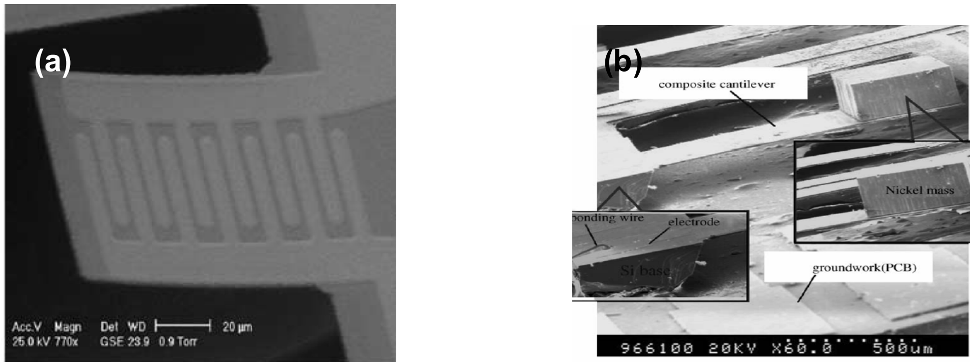

Figure 1.13(a) d_{33} mode energy harvesting device (Used with permission from Elsevier, License No: 1971191064688) (b) d_{31} mode energy harvesting device (Used with the permission from Elsevier, License No: 1971190704094)

An interesting mechanical energy harvesting device has been reported by Shen et al.[78] In this work, an embedded Silicon mass was utilized in order to automate the fabrication process. This device was found to generate 2.15 µW at 2g acceleration and 461Hz frequency.

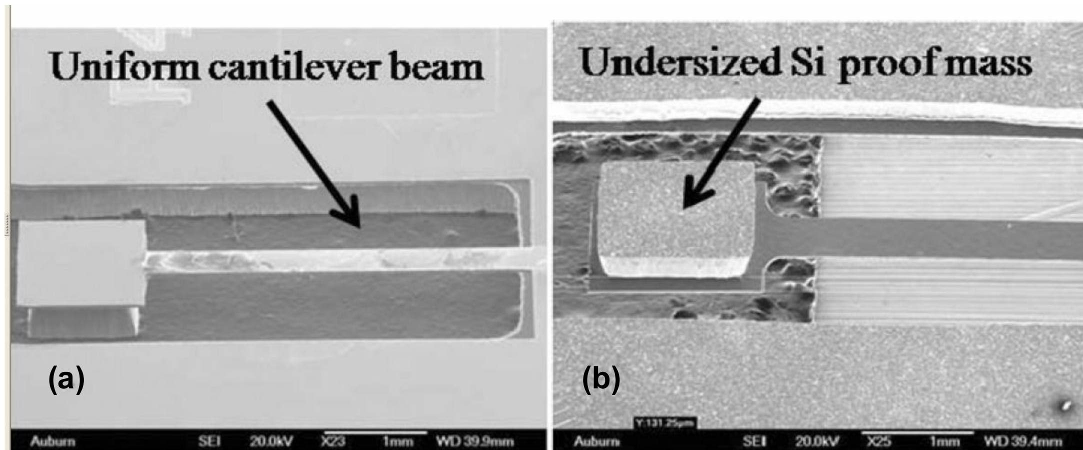

Figure 1.14(a) SEM image of front side and (b) back side of energy harvesting device of embedded Si Proof mass (Reprinted with permission from Shen et al., Copyright: IOP Publishing, 2008)

1.12 Current status of piezoelectric micro-generator

In general, mechanical to electrical energy conversion at resonance can be modeled using the second-order spring-mass system with damping. The power conversion (P) at resonance is given as:

$$P = \frac{m\varsigma A^2}{8\pi f \varsigma_T^{\ 2}} = \left(\frac{\varsigma_e}{\varsigma_T^{\ 2}}\right)\left(A^2 / 8\pi f\right) \qquad (38)$$

where m is the seismic mass, A is the acceleration of the excitation; f is the frequency of the excitation equivalent to system resonance frequency, and ς_e and ς_T are the electrical and total damping ratios. This expression illustrates that the generated power from the harvester is dependent upon the excitation ratio, $\Omega = (A^2/8\pi f)$, assuming that the working frequency is close to the resonance. Let's use the excitation ratio as a metric to draw comparison among the existing prototypes. Table 1.4) shows the data from literature for various mechanical energy harvesters utilizing piezoelectric, electromagnetic, and electrostatic mechanisms.

Table 1.4 Compilation of the power density and operating condition for various mechanical energy harvesting devices.

Power(uW)	f(Hz)	a(m/s^2)	Power density(uW/mm^3)	Excitation ratio(m^2/s^3)	Method	Ref
2.1	80.1	2.3	125	2.63 x10^{-3}	Piezoelectric	[79]
210	120	2.5	1000	2.07 x10^{-3}	Piezoelectric	[80]
375	120	2.5	1000	2.07 x10^{-3}	Piezoelectric	[79]
0.3	4400	382	5.4	1.319	Electromagnetic	[81,82]
180	322	2.7	840	9x10^{-4}	Electromagnetic	[83]
4000	100	0.4	30000	6.366x10^{-4}	Electromagnetic	[84]
3.7	30	50	750	3.315	Electrostatic	[85]
6	10	3.9	800	0.0605	Electrostatic	[86]
1052	50	8.8	1800	0.0616	Electrostatic	[87]
1.13	870	78.4	3.75	0.02811	Piezoelectric	[88]
46	52	0.59	150	2.663 x 10^{-4}	Electromagnetic	[89]
830	110	95.5	1000	3.298	Electromagnetic	[90]
0.584	60	8.829	150	0.05169	Electromagnetic	[91]

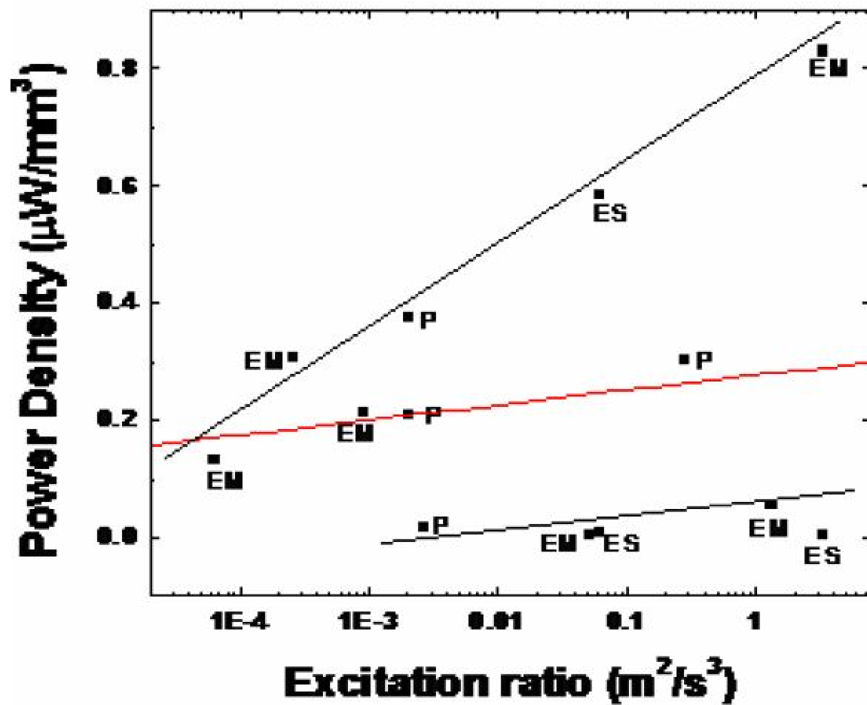

Figure 1.15 Plot of power density as a function of excitation ratio for various mechanical to electrical energy conversion devices reported in literature.

Figure 1.15 shows the variation of power density as a function of excitation ratio (note the log scale on X-axis). Various prototypes can be divided into three regions which are represented by linear lines. The difference between the three categories can be related to the difference in the working frequency compared to the resonance frequency, total volume, and damping factors.

CHAPTER 2

ENERGY HARVESTING DEVICE FABRICATED BY LASER MICROMACHINING OF Pb $(Zr_{0.52}Ti_{0.48})O_3$-$Pb(Zn_{1/3}Nb_{2/3})O_3$ CERAMICS

Results have been reported on thin film based piezoelectric devices for harvesting vibration mechanical energy as mentioned in the previous chapter. Jeon et al.[80] have reported the results on piezoelectric cantilevers having dimensions of 100 x 60 x 0.48 μm^3 with inter-digitated electrodes (d_{33} mode). At the resonance frequency of 13.9 kHz, the output power was measured to be 1.01μW across a 5.2 MΩ load. Reilly et al.[92] have conducted modeling of a PZT film based energy harvesting structure and reported a power density of 80μW/cm^3 at the operating frequency of 800 Hz based on the simulation. Beeby et al.[93] have recently reviewed the power density of vibration to electric converters. The power density of piezoelectric micro energy harvesting devices ranges between 0.01 - 0.4 μW/mm^3 in the acceleration range of 2.3 – 78.4 m/s^2 and the frequency range of 0.08 – 1 kHz. Naturally, the question that comes to mind is: "How can the power density of piezoelectric energy harvesters be increased at small scale?" The power generated from vibration to electric converters can be approximated at the resonance frequency of the system by Eq. (39) as:[94]

$$P_{res} = \frac{mY_o^2\omega_n^3}{4\varsigma} \qquad (39)$$

where ω_n^2 = k/m is the system resonant frequency, m is the seismic mass, k is the spring constant, Y_o is the amplitude of vibration and ς is the damping ratio. Equation (39) implies that the power is inversely proportional to the damping ratio which should be minimized through proper selection of materials and and design. The damping ratio is combined effect of the mechanical and electrical quality factors. Thus, if all the factors remain unchanged than the power of energy harvester can be increased by increasing the

electrical quality factor. This implies that a piezoelectric material with higher quality factor should be selected for fabrication. In terms of acceleration (a), the above expression can be written as:

$$P_{\max} = \frac{ma^2}{4\omega_n \varsigma} \qquad (40)$$

which implies that output power is proportional to the square of acceleration. Another important conclusion that can be drawn from Eq. (40) is that the output power is directly proportional to proof mass of the system and therefore reducing the size of converter reduces the conversion efficiency. The efficiency (η) of the vibration to electric conversion process was shown to be given by Eq. (41)[95]:

$$\eta = \frac{1}{2}\frac{k^2}{1-k^2} \Big/ \left(\frac{1}{Q_m} + \frac{1}{2}\frac{k^2}{1-k^2} \right) \qquad (42)$$

where k is the electromechanical coupling factor, and Q_m is the quality factor. Thus, the answer to the question posed earlier is that power density of piezoelectric energy harvester can be increased by maintaining the high magnitude of material parameters, such as k and Q_m in the fabricated device.

In this study we report on a fabrication technique which will allow design of the small scale structures with high precision. The fabrication technique utilizes pulsed laser to machine any given structure from a piezoelectric wafer, providing the freedom of selecting any desired piezoelectric composition. The difficulty with prior approaches remains the complex synthesis techniques which involve multiple steps, clean room conditions, and limits the piezoelectric composition. Recently, we have reported a high energy density piezoelectric composition in the system $Pb(Zr_{0.52}Ti_{0.48})O_3$-$Pb(Zn_{1/3}Nb_{2/3})O_3$ with a magnitude of 80.84 mJ/cm^3 [96]. As improvements continue to occur in material composition, the energy harvester can be improved by incorporating better material. The overall objective of this chapter is to realize a miniature, low resonance frequency and cost effective energy harvesting device which is fully packaged and can be easily mounted on a given platform.

2.1 Fabrication process

A soft piezoelectric material in the Pb $(Zr_{0.52}Ti_{0.48})O_3$-$Pb(Zn_{1/3}Nb_{2/3})O_3$ system was synthesized using conventional ceramic processing technique[102]. The wafers of the sintered ceramic were fabricated by grinding and polishing with 500μm finish papers. The wafers were electroded using Ag/Pd paste electrode and fired at 650°C. Poling was done at 80°C by applying a DC field of 3kV/mm. A YAG laser with wavelength of 1064nm and pulse width on the order of ~1ns with high power was used for machining. The time for the whole machining process was about 3hr 10mins. The smallest feature that can be machined using the nano second pulse is on the order of 75μm. Figure 2.1 and Figure 2.2 show pictures of the laser machined cantilever beam.

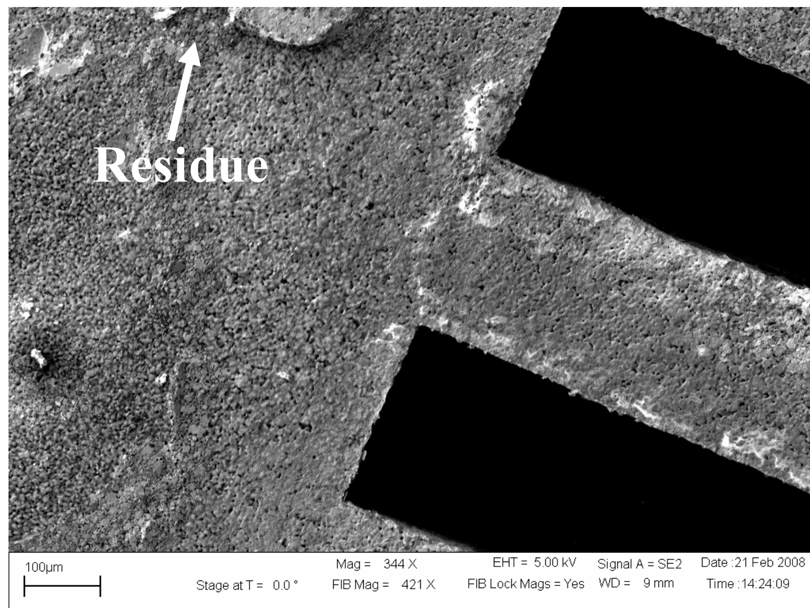

Figure 2.1 Laser machined cantilever beam (SEM picture)

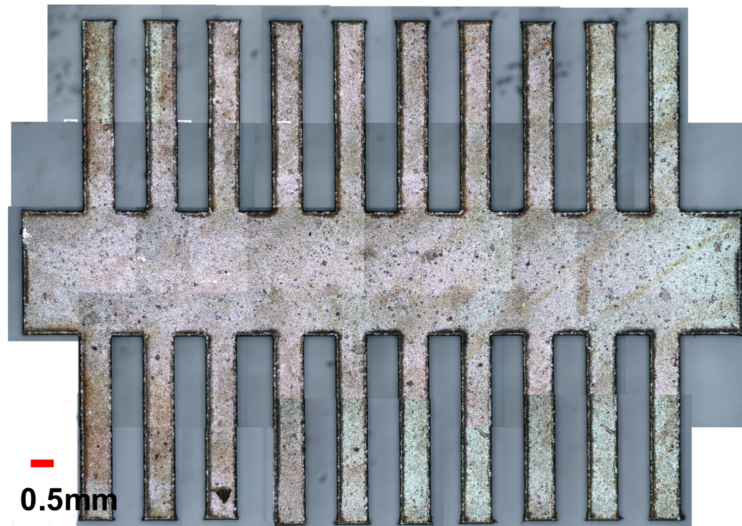

Figure 2.2 Laser machined cantilever beam (optical picture)

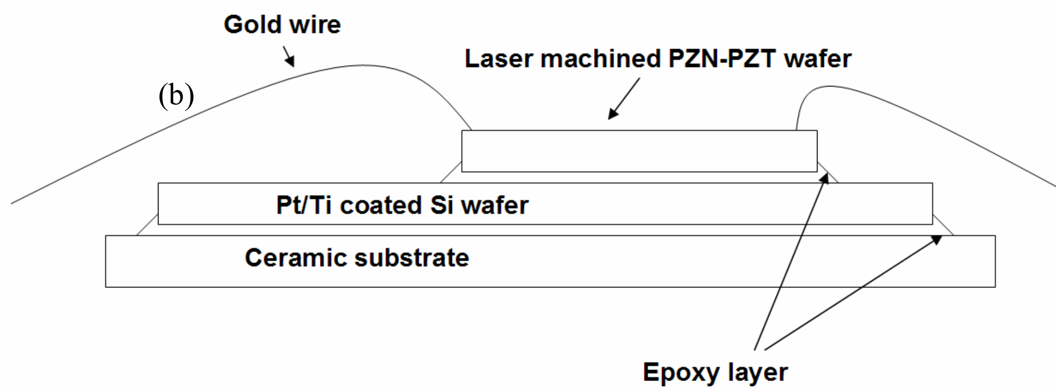

Figure 2.3 Schematic of side view of stacked wafer

A conventional micro-electronics packaging process was adopted to mount the cantilever beams. For the bottom die bonding, non-conductive thermal curing epoxy was used as the attachment. For the top PZT cantilevers beam bonding, conductive epoxy with silver filler was used. Gold wire (1.0mil diameter) was bridged for the electrical connection between top silver electrodes and bonding pad of CERDIP (Ceramic Dual In-line Package). Two types of wire bonding parameter were used to compare the thermal effect on the output voltage of device. In the first case, temperature of the wire bonding chuck was maintained at 150 °C. The material for the tip mass was selected as Sn/Pb solder ball with 0.7mm diameter and mass of 4.2mg. This solder is commonly used for the BGA (Ball Grid Array) microelectronics package. The tip mass was attached using resin and cured at 170 °C / 20min on the hotplate to form inter-metallic between top silver electrode and solder ball. In the second case, low

temperature was used to decrease the degree of depoling. Temperature of wire bonding chuck was maintained at 130°C and instant glue was used for attaching the tip mass. Sn/Pb solder ball were used as tip mass with diameter and mass of 0.5mm and 1.53mg. There were ten cantilevers on both side of the bridge, five of them with tip mass and five without tip mass. We used tip mass alternately so that the cantilevers vibrate with different resonance frequency providing voltage response over a wider frequency range. The laser machined cantilever beam and assembled energy harvesting device is shown in Fig. 2.4.

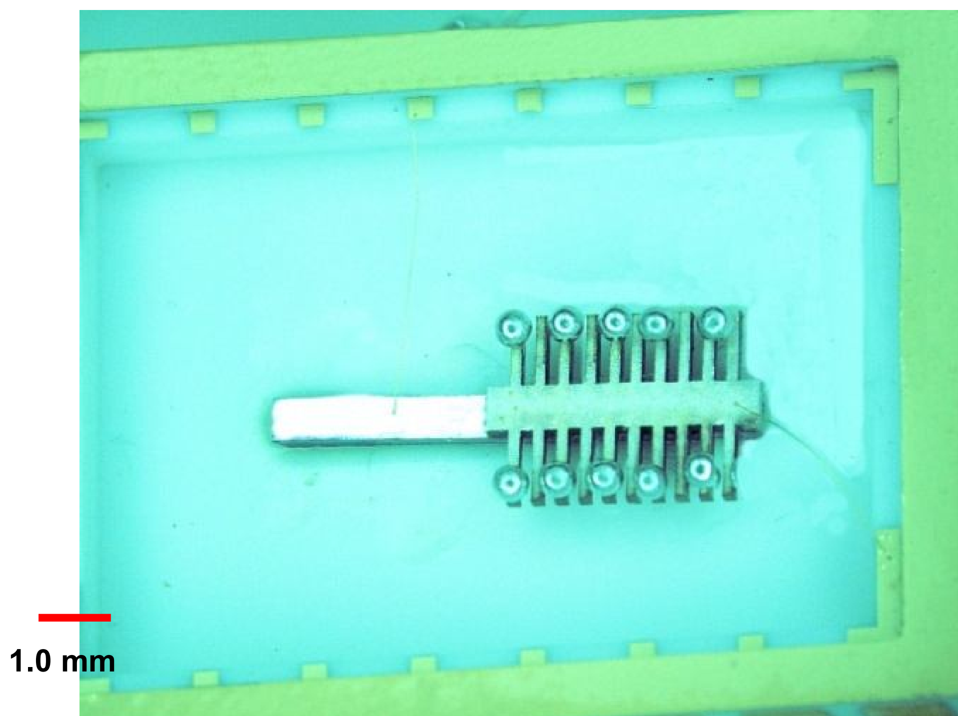

Figure 2.4 Assembled energy harvesting device

2.2 Experiment setup

A mechanical shaker obtained from Unholtz Dickie Coporation (Model No. TA30-5PM) was used to conduct the test at varying frequency and vibration amplitudes. Figure 2.5 ~Figure 2.7 show the mounting package and accelerometer on the shaker with experimental setup for characterizing the performance of the harvester.

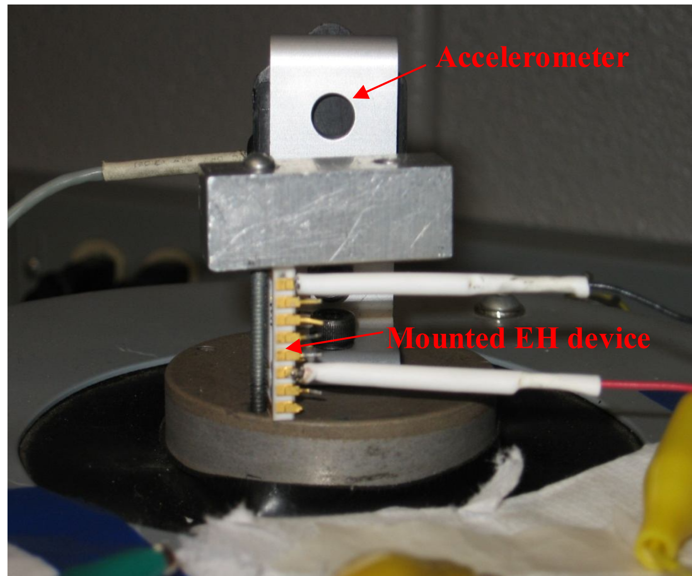

Figure 2.5 Mounted EH device on the shaker

Figure 2.6 Oscilloscope for the acceleration (top) measurement and Lock-in amplifier for voltage (bottom)

Figure 2.7 Shaker (Left) and amplifier (Right).

The magnitude of acceleration was fixed using ADXL 150EM-1 accelerometer from Analog Devices. The output voltage from the piezoelectric energy harvester was measured using a lock-in amplifier (Model No. SR810). Assembled samples were tested with displacement occurring in the vertical direction of the mounting package. In the case of vertical mounting, the width and thickness of the cantilever are given as w=0.5mm and t=0.25mm, while for horizontal mounting the width and thickness of the cantilever are as w=0.25mm, and t=0.5mm. Hence, the vertical mounting is more effective way to achieve higher deflection. We will discuss more about this in the section 2.3.

2.3 Result and Discussion

The voltage response was measured over a wide frequency range of 50-1000Hz and acceleration was fixed at 8g. Figure 2.8 shows the open circuit output voltage in two different mounting conditions. High voltage response was found at frequency of 870Hz. The high voltage output at this frequency is related to the mechanical response of the whole package based on the calculations for cantilever. As can be seen from Fig. 2.2, there are ten cantilevers on both side of the bridge. In most of the expressions derived for cantilever beam, it is assumed that one end is fixed and force is being applied at the other. However, in our case the whole package was mounted on top of the shaker. Thus, the expression derived for cantilever beams are not directly applicable here. For simplicity we will use the

conventional case to estimate the natural resonance frequency. The resonance frequency of the cantilever beam is given in Eq. (43)

$$\omega = 2\pi f = \sqrt{\frac{k}{0.236m + m_{tip}}} \tag{43}$$

where m and m_{tip} are the mass of the cantilever and tip respectively.

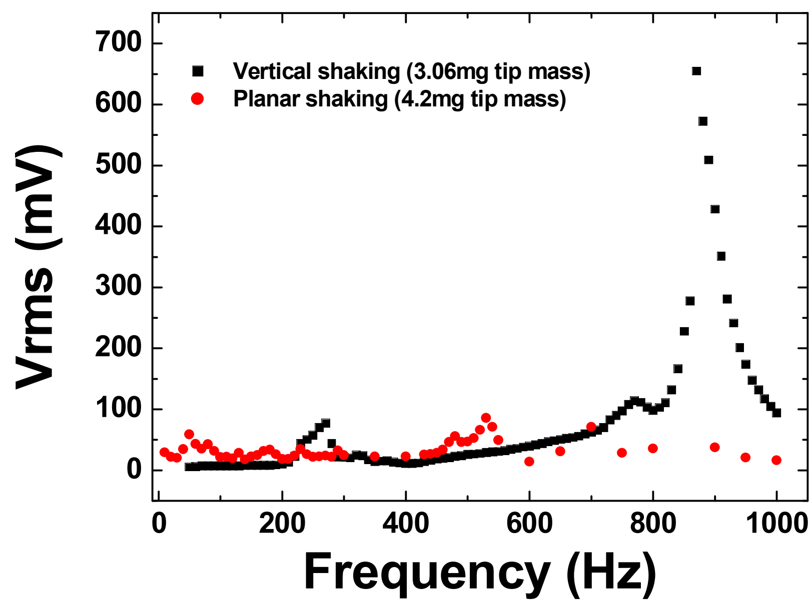

Figure 2.8 Output voltage (Vrms) in the open circuit condition as a function of frequency for the fabricated energy harvester in two different mounting conditions.

The force constant k can be approximated by Eq. (44)

$$k = \frac{3EI}{L^3} = \frac{Ew}{4}\left(\frac{t}{L}\right)^3 \tag{44}$$

where I is the moment of inertia=$wt^3/12$, w is the cantilever beam width, t is the thickness and L is the length of the cantilever beam. In our case, the elastic modulus is approximately 5.1 x 10^{10} N/m^2, w=0.5mm, and t=0.25mm, so k is 29.51 x 10^3 N/m. The resonance frequency for the cantilever with and without tip mass can be calculated to be 47.1 kHz and 14.8 kHz respectively (density of PZT ~7.6 g/cm^3, m_{tip}= 3.06 mg). These frequencies are far from the peak observed at 870Hz. The PZT cantilever structure

used here has asymmetric loading, as the tip mass is attached at the side rather than at the top. Thus, longitudinal stress applied to the PZT may result in some low frequency flexure mode but this will be higher than the 870 Hz. FEM simulation conducted using ATILA software on the machined cantilever did not show any evidence of low frequency flexure as shown in Figure 2.9. The input voltage used in the simulation was 5V.

We expect that the peak at 870Hz is correlated to the rocking or bouncing mode of the chip package, as it is held together by an aluminum bar as shown in figure 2.3 a). The weight of aluminum bar was 16.86g and the dimensions were 38.23mm x 13.43mm x 12.80mm. This mode could also be influenced by the buckling of the chip package occurring as a result of loading from aluminum bar, as schematically depicted in Fig. 2.10.

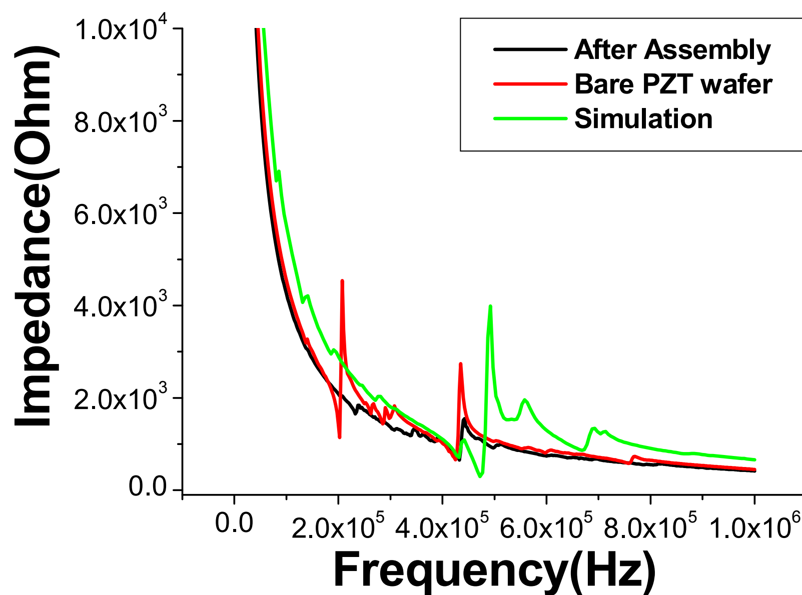

Figure 2.9 Impedance spectrum of the PZT wafer before and after laser machining. After laser machining the wafer was mounted onto chip package and wire bonded for measuring the spectrum. FEM Simulation was conducted on the laser machined wafer attached to package.

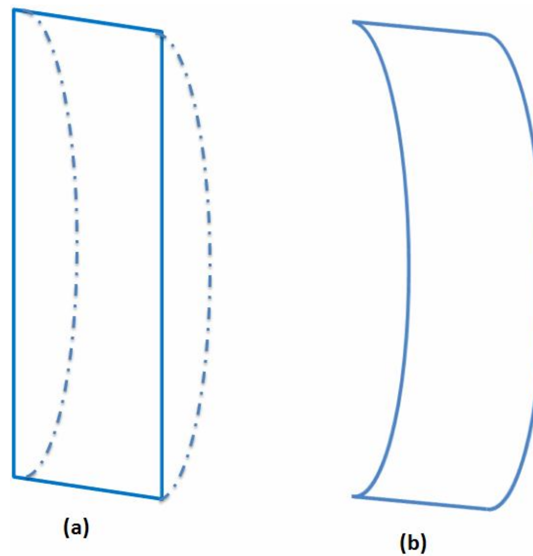

Figure 2.10 Schematic depiction of the buckling of the chip package under the loading of the aluminum bar (exaggerated) (a) Initial state and (b) Final state.

The maximum V_{rms} voltage was measured to be 655 mV at 870Hz with a tip mass of 3.06 mg attached using the process described for the low temperature wire bonding. Another low frequency peak was found at 270Hz. Since there are no low frequency peaks in the impedance spectrum, we assume this peak is correlated with the mounting assembly, which was comprises of the mounting package, connectors, piezoelectric cantilever structure with tip mass and holders. Figure 2.11 (a) and (b) shows the variation of the output voltage and power as a function of load for two different frequencies. A maximum power of 1.13 μW was measured across the matching load of 288.5kΩ at 870Hz. At the frequency of 270Hz, the maximum power obtained was 0.06μW across the matching load of 949kΩ. The power was calculated using Eq. (10).

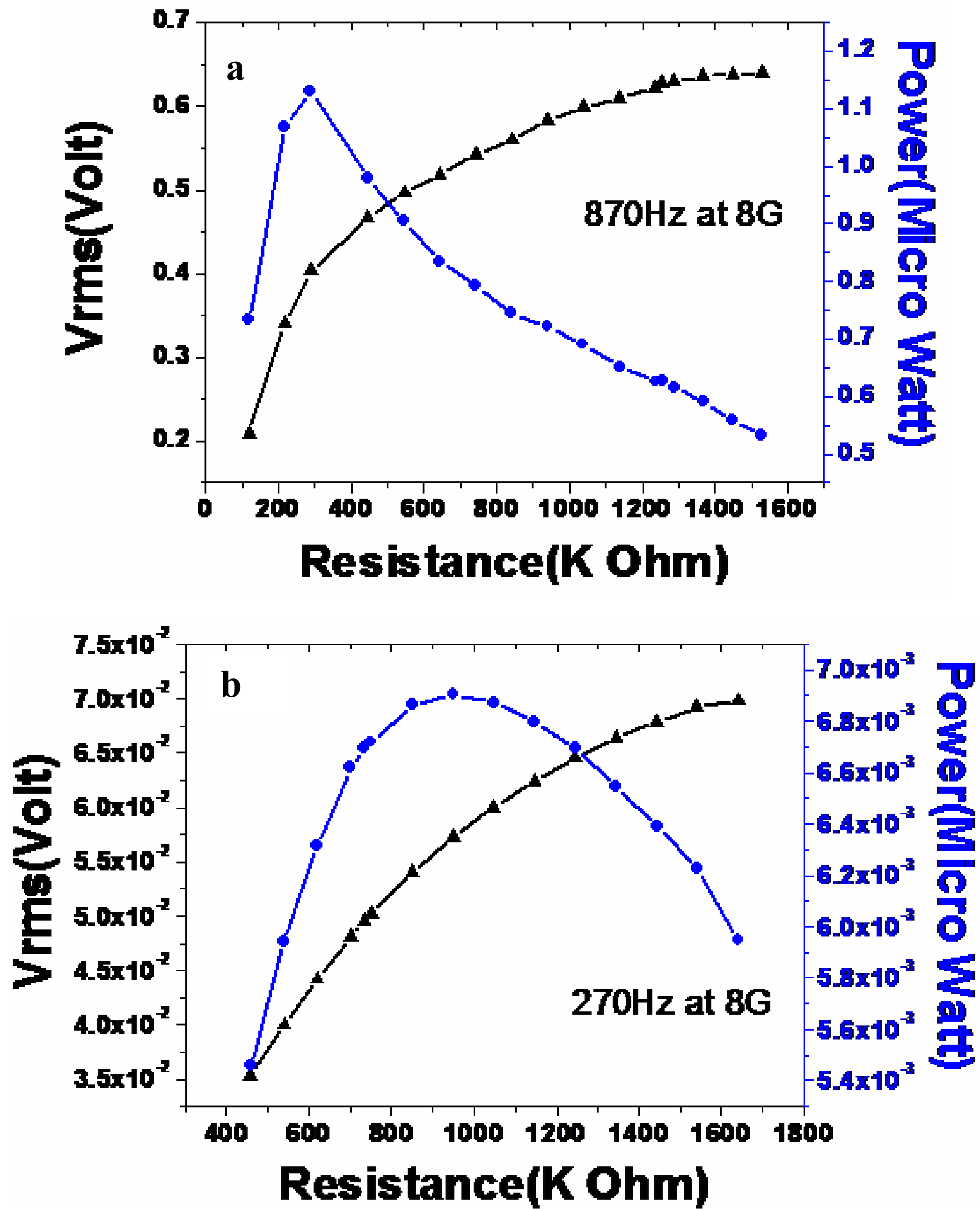

Figure 2.11 (a) Variation of the output power & voltage as a function of load at frequency of 870Hz under 8g acceleration, (b) Variation of the output power & voltage as a function of load at frequency of 270Hz under 8g acceleration.

2.4 Summary

In this study, we report results on a piezoelectric material based mechanical energy harvesting device which was fabricated by combining laser machining with microelectronics packaging technology. It was found that the laser machining process did not have a significant effect on the electrical properties of the piezoelectric material. The fabricated device was tested in the low frequency regime of 50 – 1000 Hz at the constant force of 8g (where g = 9.8m/s^2). The device was found to generate continuous power of 1.13μW at 870 Hz across a 288.5 kΩ load with a power density of 301.3 μW/cm^3.

CHAPTER 3

BARIUM TITANATE THIN FILMS FOR LEAD-FREE MICRO-POWER GENERATOR

Prior research has been focused on fabrication of piezoelectric energy harvesting device using PZT[97, 98]. However, current trend in the world is on developing environment friendly materials and elimination of Pb from household devices. Thus, there is need for an alternative to PZT however the success has been very limited. Out of all the possible choices, $(K_XNa_{1-x})NbO_3$ (KNN) based ceramics (e.g.- solid solution of KNN-$LiNbO_3$, KNN-$LiTaO_3$, KNN-$LiSbO_3$, KNN-$Li(Nb,Ta,Sb)O_3$, KNN-$BaTiO_3$, KNN-$SrTiO_3$, and KNN-$CaTiO_3$ etc) have been found to be promising, mainly two reasons: (i) piezoelectric properties exist over a wide range of temperature, and (ii) there are several possibilities for substitution and addition of element. Thin film deposition of alkali based system is challenging due to evaporation of Na. On the other hand, $BaTiO_3$ thin films have been widely studied for several applications including sensors and multilayer capacitors. In comparison to KNN system, BT has a lower value for the piezoelectric coefficient and the Curie temperature however it is more stable. The other piezoelectric candidate for energy harvester is zinc oxide (ZnO), but it possesses low value for the piezoelectric coefficient. Table 3.1 shows the properties of lead free candidates for thin films based energy harvesters. This table shows that BT films posses much higher dielectric and piezoelectric constants compared to ZnO and AlN[99].

Table 3.1: Piezoelectric properties of lead free piezoelectric candidates ($BaTiO_3$ value is for (111) epitaxial thin film).

	$e_{31,f}$ (C/m^2)	$d_{33,f}$ (Pc/N)
ZnO [10, 11]	-1.0	5.9
AlN [10, 11]	-1.05	3.9
$BaTiO_3$ [10]	-23	124

The effective piezoelectric coefficients are given by Eq. (45):[100,101]

$$e_{31,f} = \frac{d_{31}}{s_{11}^E + s_{12}^E} = e_{31} - \frac{c_{13}^E}{c_{33}^E} e_{33}$$
$$d_{33,f} = \frac{e_{33}}{c_{33}^E} = d_{33} - \frac{2s_{13}^E}{s_{11}^E + s_{12}^E} d_{31} \tag{45}$$

Yako et al.[102] have reported that (111) oriented tetragonal $BaTiO_3$ single crystal has higher longitudinal piezoelectric constant than that of (001). Jun et al.[103] have shown through calculations that piezoelectric constant $e_{31.f}$ and $d_{33.f}$ have their maximum values along the axis close to the (111) direction. These results indicate that (111) oriented $BaTiO_3$ thin films can provide large piezoelectric coefficients and serve as a suitable candidate for lead-free energy harvesting MEMS device. Similar results have been calculated and measured for the PZT film. Du et al.[104] have shown that rhombohedral PZT (60/40) composition has maximized piezoelectric response along 57° and 51° canted from the spontaneous polarization direction.

3.1 $BaTiO_3$ sol-gel synthesis

$BaTiO_3$ solution was synthesized using the method reported by Lee et al[105]. Barium acetate (Sigma Aldrich) was used as the barium precursor, 50wt% Titanium bis (ammonium lacto) dihydroxide (Sigma Aldrich) was used as the titanium precursor, and acetic acid (Sigma Aldrich) was used as a solvent. PVP (Polyvinyl pyrrolidone) (Sigma Aldrich) was added in order to decrease film stress during the annealing process. The initial solution consisted of 1:1 (Ba: Ti) molar ratio which was modified later as 1:1:0.5 (Ba: Ti: PVP), where mole ratio of PVP was calculated based on the repeating unit of PVP chain as shown in Fig. 3.1. The average molecular weight of PVP used in experiment was 360,000.

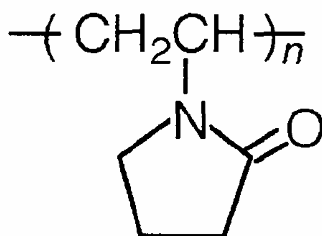

Figure 3.1 PVP (Polyvinylpyrrolidone)

For the synthesize of barium titanate solution, 4gm of barium acetate was dissolved into 36.2ml of acetic acid and stirred until all barium acetate particles were dissolved. Next 7.70 mℓ of titanium bis (ammonium lacto) dihydroxide was added into the dissolved solution followed by 0.8gm of PVP. Acetic acid was added to this mixture to realize a 0.45M/L solution. The resulting solution was heated to ~100°C and stirred with reflux for 12hrs. Figure 3.2 shows the block diagram of $BaTiO_3$ solution synthesis process.

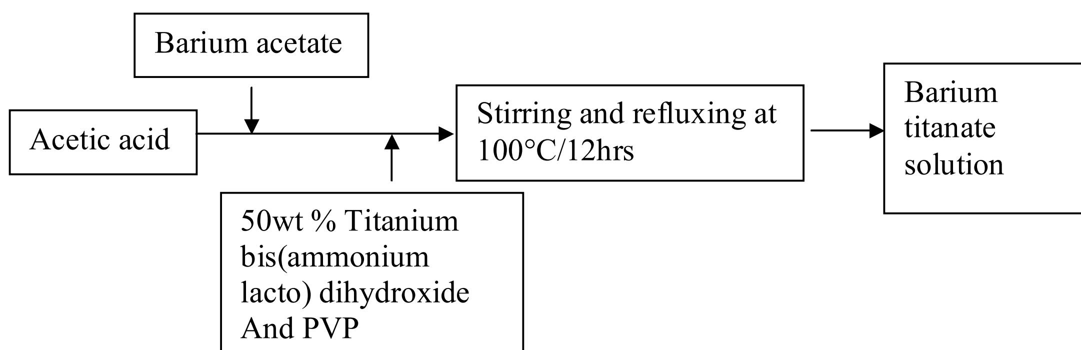

Figure 3.2 Barium titanate solution synthesis flow chart.

TGA and DSC analysis was conducted in air with 10°C/min ramp-up rate to clarify pyrolysis and crystallization temperature. Figure 3.3 shows the TGA and DSC result of 1mole ratio solution without PVP. Zone 1, which is the range from 150 to 200°C, is the regime of water and acetic acid evaporation. Zone 2, which is the range from 200°C to 500°C, is the pyrolysis of barium and titanium chelating agent. It can be seen from this figure that phase change from amorphous to crystalline state occurs around 500°C to 600°C[105]. After finishing the TGA and DSC analysis, XRD measurement was done on the same powder. The XRD pattern clearly exhibited the peaks for barium titanate.

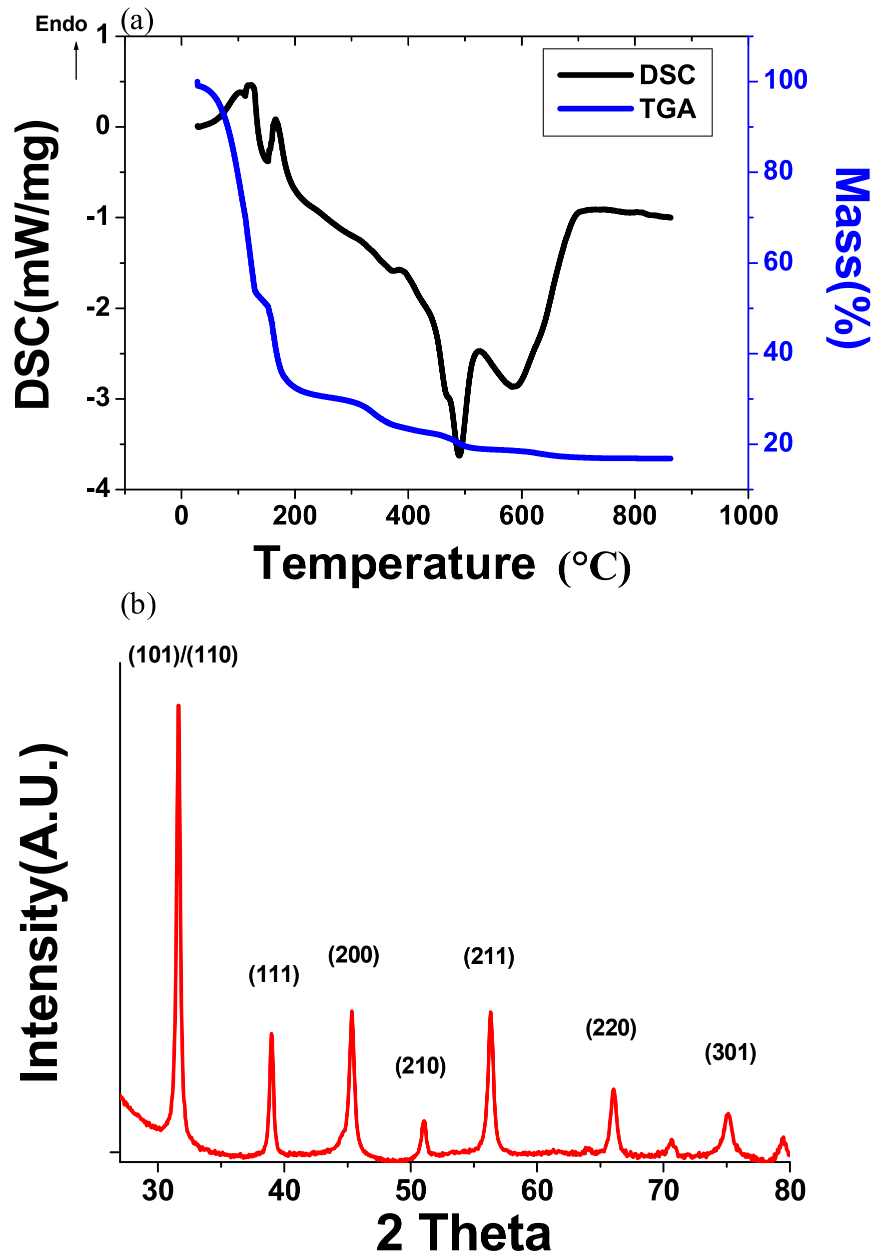

Figure 3.3 (a) TGA and DSC of the barium titanate solution, (b) XRD pattern after TGA/DSC measurement (Data measured after heating the solution for 4hrs at 100°C).

3.2 $BaTiO_3$ thin film characterization

3.2.1 Effect of annealing temperature and time on ferroelectric property

The first step in thin film deposition was cleaning the $Pt/Ti/SiO_2/Si$ wafer with acetone using ultrasonic bath. The thickness of each layer was 150nm (Pt), 20nm (Ti), 20nm (SiO_2) and 500~550μm (Si). PWM32-PS-R790 spin coater was used to deposit the barium titanate thin film on the surface of cleaned wafer with coating parameters of 4000rpm / 30sec. The deposited film was semi-pyrolyzed on hot plate at 185°C/10mins. This process was repeated several times to increase the thickness of film. Rapid thermal annealing (RTA) was used to fully pyrolyze and crystallize the film. In order to study the effect of annealing temperature and time on the ferroelectric properties of $BaTiO_3$ thin film, one variable was varied at a given time. The parameters c/a ratio, dielectric constant, resistivity, and polarization were measured at the end of each experiment. In order to measure these properties, Au/Cr top electrode and Pt/Ti bottom electrode combination was used as the Metal-Insulator-Metal structure. The top electrode size was 0.8 mm x 0.8 mm. Capacitance was measured using an HP LCR meter, while the resistivity and P-E loop were measured with a PLC (Radiant Technology Inc.). The breakdown electric field for the deposited films was found to be 300kV/cm. Figure 3.3 (a) – (d) summarizes the result of experiments.

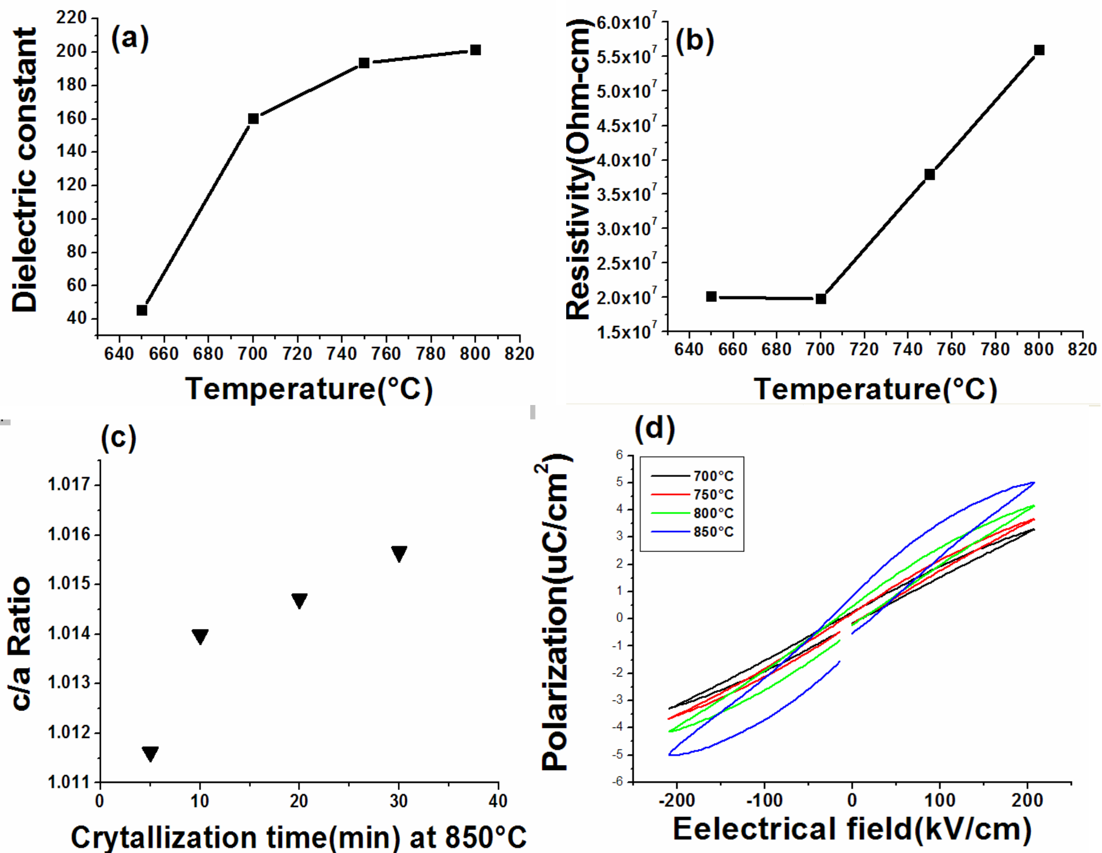

Figure 3.4 (a) Temperature dependence of dielectric constant with 5 min crystallization time (b) Temperature dependence of resistivity with 5 min crystallization time (c) Crystallization time dependence of c/a ratio at 850°C (d) Temperature dependence of polarization with 5min crystallization time (at 1kHz)

It can be seen from above figure that dielectric and ferroelectric properties of the film increased with crystallization temperature. The ferroelectric polarization loop exhibited high sensitivity to the crystallization temperature as Pr increased 2X with increase of temperature from 700°C to 850°C. The time dependence of c/a ratio showed similar trend increasing with time. In summary, the process parameter for crystallization were found to be as 850°C/5~10mins. The pyrolysis and crystallization in RTA was studied with these steps: 180°C/10mins drying on the hotplate, 300°C/10mins, 400°C/10mins, 500°C/10mins, 600°C/10mins, 700°C/10mins and 800°C/10mins. Figure 3.5 shows the process flow chart of barium titanate thin film deposition.

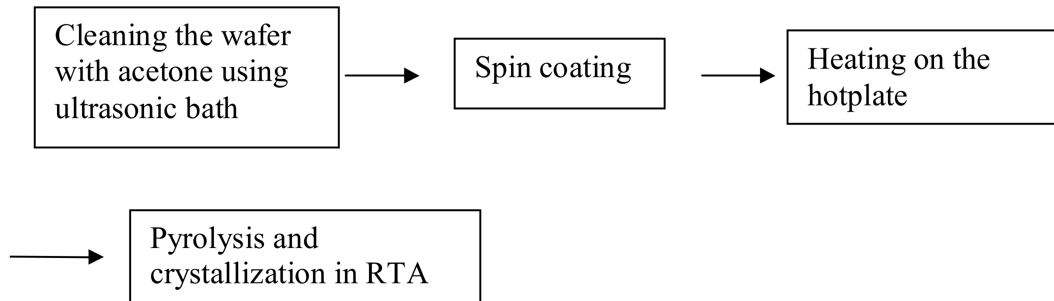

Figure 3.5 Process flow of the barium titanate thin film deposition and crystallization

3.2.2 $BaTiO_3$ thin film with sub surface treatment using oxygen plasma

In order to achieve higher electrical properties such as dielectric constant, resistivity and Pr, it is essential to avoid formation of cracks in the film. The defects in the film could increase the leakage current between the electrodes leading to poor electrical properties and low resistivity. A plasma treatment was applied on the Pt/Ti/Si wafer to increase the surface energy on Pt surface. The magnitude of piezoelectric property is strongly related to ferroelectric domain switching and dielectric property.[118] Thus, by reducing the leakage current of Metal-Insulator-Metal structure, it is possible to get a higher piezoelectric property.

The critical thickness of film required to avoid crack formation can be expressed by Griffith fracture model[106] as:

$$t_c \cong 2E\gamma / \sigma^2 \quad (46)$$

Fracture occurs when $t > t_c$, where t and t_c are the film thickness and critical thickness. In Eq. (46), E is the Young's modulus, γ is the surface energy of the substrate, and σ is the film stress. Thus, by manipulating the surface energy of the substrate, resulting stress in the film can be changed leading to crack-free films. We used an oxygen plasma treatment to change the surface energy of Pt surface of $Pt/Ti/SiO_2/Si$ wafer. By utilizing the oxygen plasma treatment and enhancing the wetting characteristics through the addition of acetic acid, we found that crack free films up to thickness of 170nm~200nm could be fabricated. The process of plasma treatment was conducted by using a Technics Micro-RIE series 800 Plasma system for

5~10mins. The base pressure of the plasma chamber was ~20mTorr. Oxygen gas was introduced into the chamber with 20sccm while maintaining the pressure at ~230mTorr, and power at 150W. Figure 3.5 shows the crack free film on a plasma treated substrate. Table 3.2 shows the experimental matrix which was used for optimization of plasma condition.

Table 3.2 Experiment table for plasma and spin coating condition

Batch No.	Spin coating RPM / Time	Plasma condition (With O_2 gas)
1	4000 / 30s	150W / 10 min
2	5000 / 40s	150W / 20 min
3	4000 / 30s	150W / 30 min
4	5000 / 40s	150W / 30min

From these experiments, it was found that the surface condition is a crucial factor to obtain crack free film. Cracks were observed in Batch No. 3 and Batch No. 4 under the optical microscope, indicating that severe plasma treatment can have a deteriorative effect.

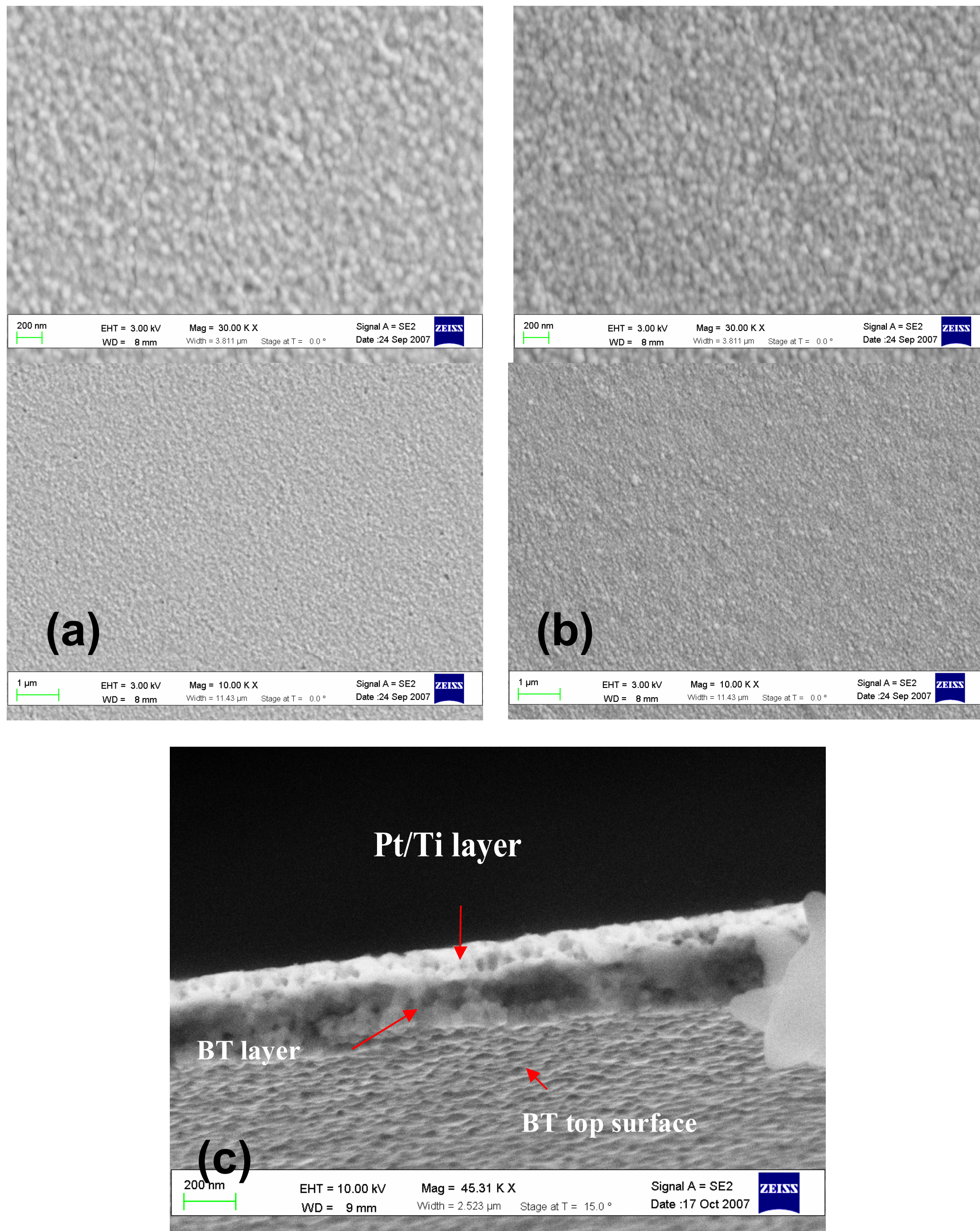

Figure 3.6 (a) Top view (Crack free) batch No 1 (b) Top view (Crack free) batch No 2 (c) Side view (Crack free)

3.2.3 (111) oriented crack free $BaTiO_3$ thin film with PVP

The multilayers were found to exhibit micro cracks on the surface. In order to resolve this problem, mixing of a stress relaxation agent was employed. It is well known that the chelating agents and diols are effective in increasing the critical thickness of a thin film[107,108]. Kosuka[109] has explained the mechanism and role of PVP during the formation of a film. In the precursor solution, PVP is thought to be hybridized with metalloxane polymers through hydrogen bonding, retarding condensation and promoting structural relaxation in films when subjected to heat treatment. Among these stress relaxation agents, PVP was selected owing to the simplicity in adaptation to the current aqueous sol-gel synthesis process. The film stress can be calculated from the differential curvature using Stoney's equation[110]:

$$\sigma = \frac{1}{3}\frac{E_s}{1-\upsilon_s}\frac{t^2{}_s}{t_f}\frac{\delta}{r^2} \tag{47}$$

where E_s, v_s and t_s are Young's modulus, Poisson's ratio and thickness of the substrate, respectively, t_f is the thickness of film and δ is the deflection of the substrate at a distance r from the center of substrate. Several researchers have shown that deflection of substrate is proportional to the temperature.[124, 125] Strain induced by thermal expansion coefficient mis match can be calculated by Eq. (48).[111]

$$\varepsilon = \Delta T(\alpha_A - \alpha_B) \tag{48}$$

where α is thermal expansion coefficients of material, ε is the strain induced by thermal mismatch, and ΔT is the difference between room temperature and growth temperature. Thus, in this experiment a lower annealing temperature was applied in order to minimize film stress.

It is reported that the high heating rates promotes heterogeneous nucleation[112] as briefly discussed in chapter I. Based on this information, as-deposited $BaTiO_3$ solution was placed on the 100°C hotplate for 10 seconds. Heat treatment was conducted using RTA (rapid thermal annealing) at 350°C for 30mins to evaporate the organics from solution. Subsequently, film crystallization was conducted at 650°C/5mins to provide seed layer. The hot plate heat

treatment was repeated after every three deposition steps. The final step was same as that used for seed layer which was 650°C/5mins. After repeating the deposition steps 4 times, the film thickness was found to be approximately 600nm with (111) preferred orientation. Figure 3.7 & 3.8 show the XRD pattern of seed and 600nm thick $BaTiO_3$ film. Figure 3.9 shows the SEM of a tilt view of a crack free $BaTiO_3$ thin film.

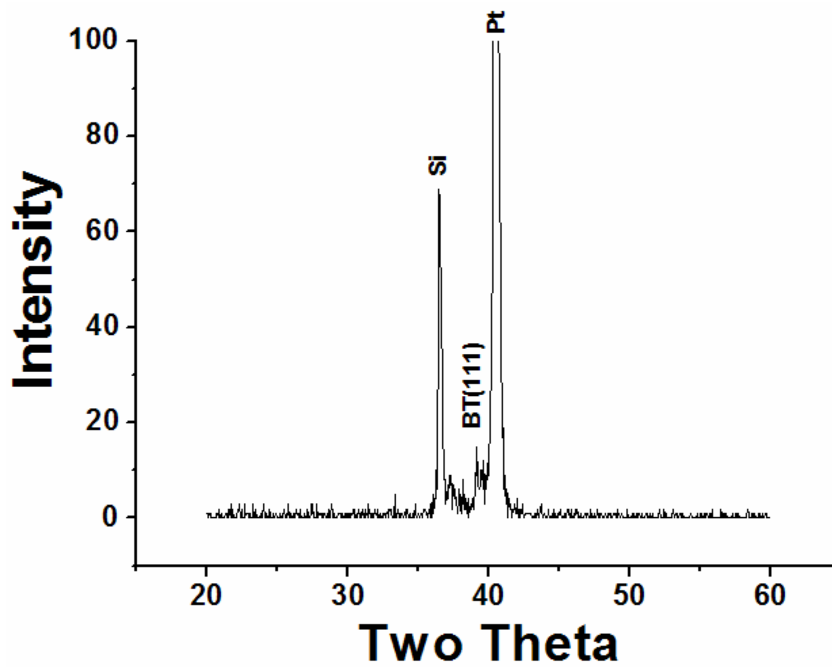

Figure 3.7 XRD of (111) preferred orientation seed layer

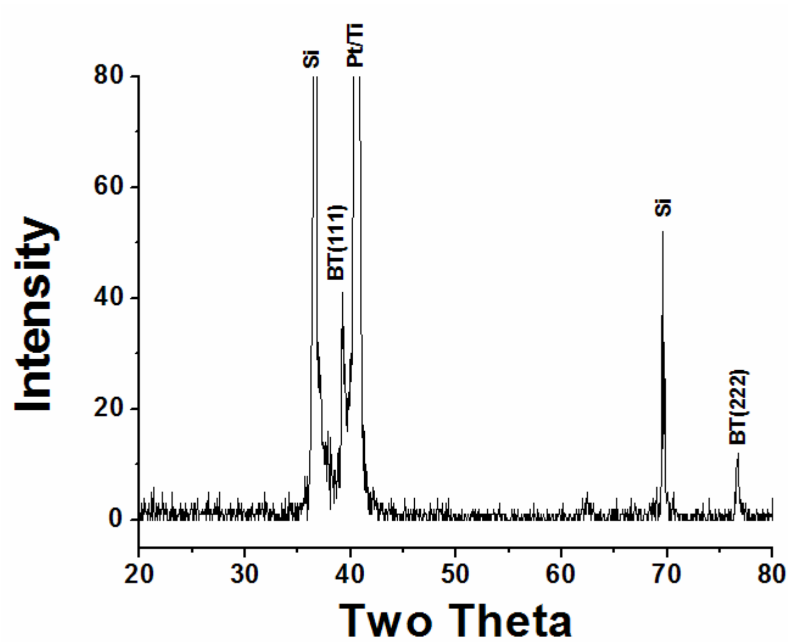

Figure 3.8 XRD of (111) preferred orientation 600nm thickness $BaTiO_3$ thin film

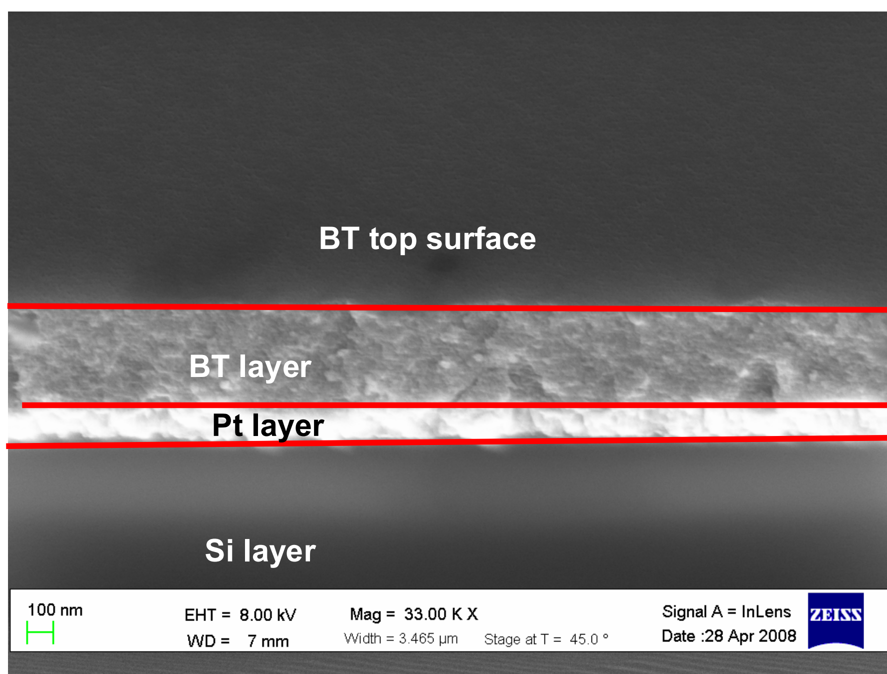

Figure 3.9 SEM tilt view of crack free 600nm $BaTiO_3$ thin film

3.2.4 Effect of BT sol-gel synthesis temperature on ferroelectric property

In order to get higher degree of polymerization in sol-gel solution, displayed hot plate temperature was increased to 130°C from 100°C. Other processes were identical except peak annealing temperature and time. Peak annealing temperature and time was 650°C/5mins using RTA. We did not anneal BT film for a long time because strain through thermal expansion could lead to crack formation. Effect of synthesis temperature on electrical properties is shown in Fig 3.10 and 3.11. Thickness of BT film was approximately 320 nm at 130°C synthesis temperature and 560nm at 100°C synthesis temperature. Fig 3.12 shows the P-E loop of BT film for initial synthesis temperature of 130°C. This result indicates that initial solution synthesis temperature is one of the factors influencing the ferroelectric property of film. Figure 3.13(a) and (b) shows the microstructure of the film.

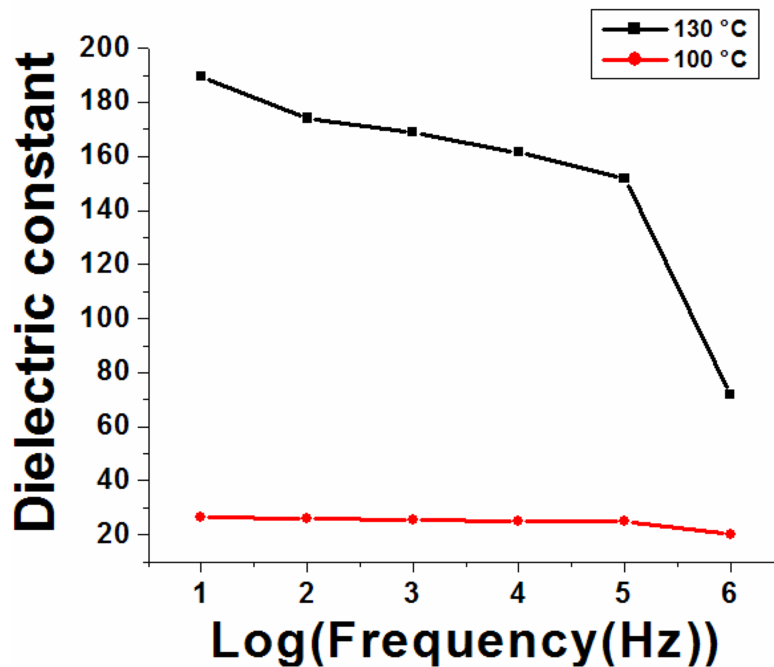

Figure 3.10 Dielectric constant vs frequency (Hz) at 1V

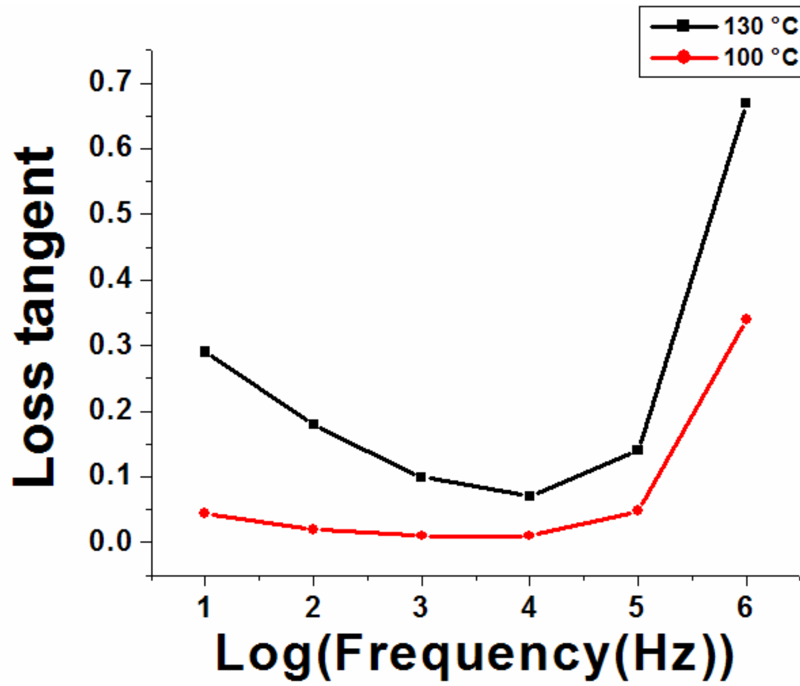

Figure 3.11 Loss tangent vs. frequency (Hz) at 1V

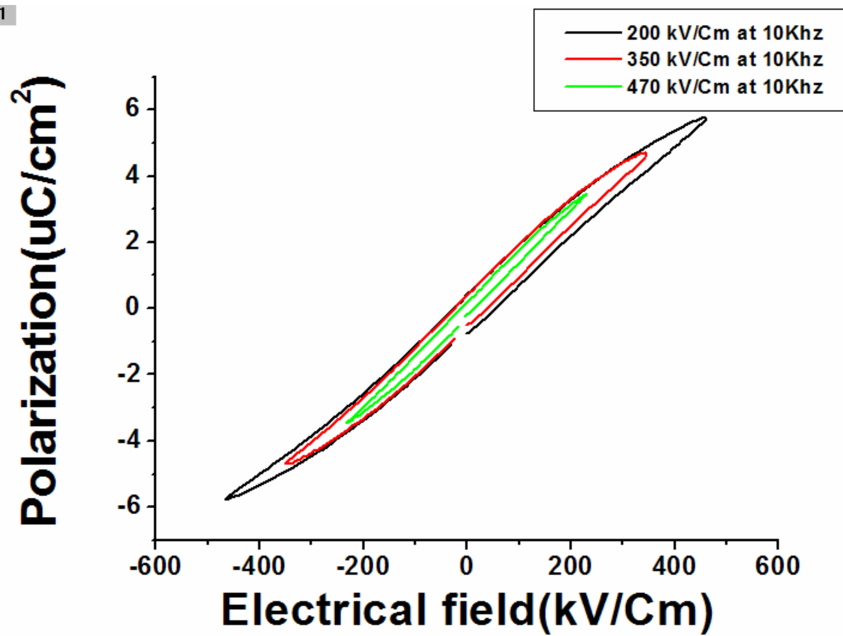

Figure 3.12 P-E loop of BT thin film from 130°C initial synthesis temperature

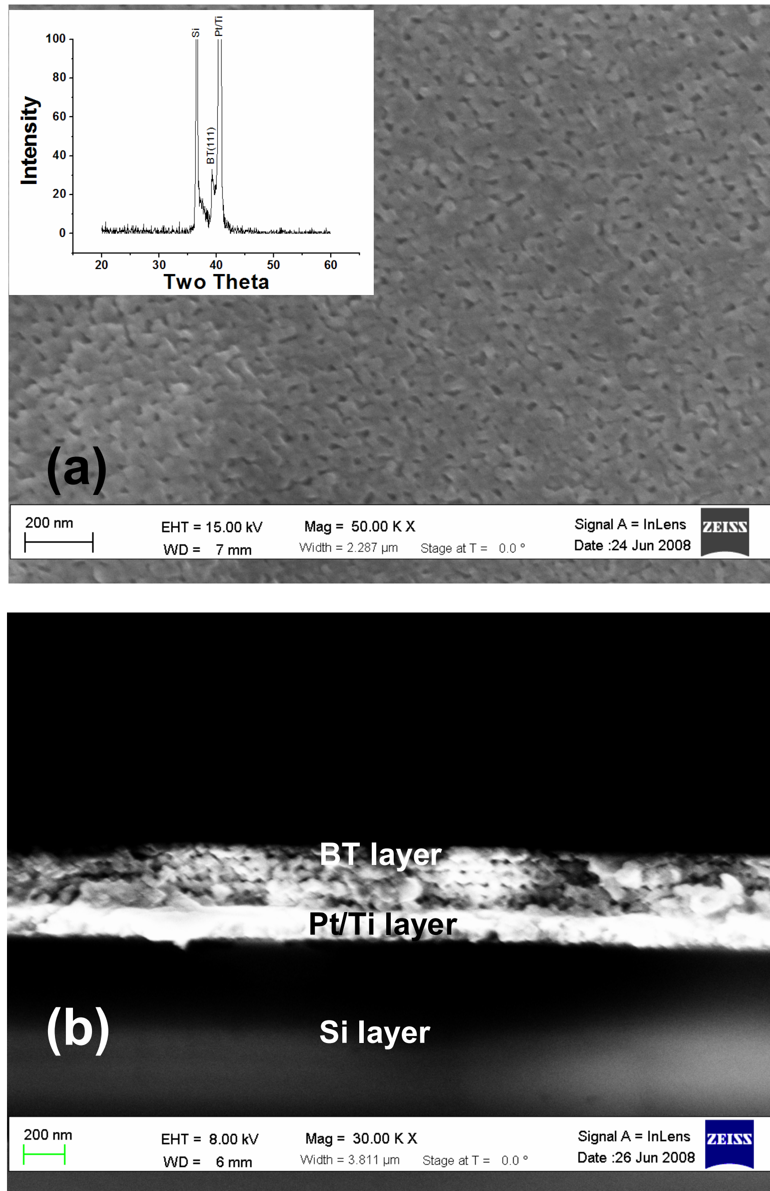

Figure 3.13 SEM image of BT thin film with 130°C initial synthesis temperature (a): top view; inset shows the XRD peak of BT thin film , and (b) side view.

CHAPTER 4

FABRICATION OF MEMS ENERGY HARVESTING APPLICATION USING LEAD FREE BARIUM TITANATE THIN FILM

One of the structures that have been commonly used in mechanical energy harvesting devices is cantilever beam with large tip mass. The operating frequency of this structure can be tuned by changing mass at the tip, dimensions, and curvature of the beam. There are three parameters that can be modified during fabrication (i) addition of tip mass, (ii) increasing mass of the cantilever beam itself, and (iii) decreasing spring constant of cantilever beam. The goal in MEMS device is to utilize all these techniques and lower the resonance frequency to 1 kHz range.

4.1 Selection of electrode design and cantilever beam layout

An energy harvesting device requires a rectifier for converting the AC signal to a DC voltage. The rectification step consumes a significant fraction of the generated voltage and thus it is required to design a structure that generates as high voltage as possible. Keeping this consideration in mind, an interdigital electrode pattern was chosen to utilize d_{33} mode. Equation (49) shows the relationship between stress, σ, and the output voltage, V, as: [113]

$$V_{3i} = \sigma_{\chi\chi} g_{3i} L_i \qquad (49)$$

where V_{3i} is the open circuit voltage, g_{3i} (Vm/N) is the piezoelectric voltage constant and L_i is the distance between electrodes. If there are ten electrode pairs, the output voltage will be 10X higher as compared with that using the d_{31} mode. Since the piezoelectric charge constant of g_{33} is about 2X higher than that of g_{31} it is expected that a 20X higher voltage, compared to the d_{31} mode can be obtained. Figure 4.1(c) shows the d_{33} mode electrode configuration. If each cantilever beam is connected in series the output voltage will be further increased as shown in Fig. 4.1 (a). The output voltage difference can be expressed as: [114, 115]

Series connection: $V_{total} = \Sigma V_i$ (50)

Parallel connection: $1/V_{total} = \Sigma 1/V_i$ (51)

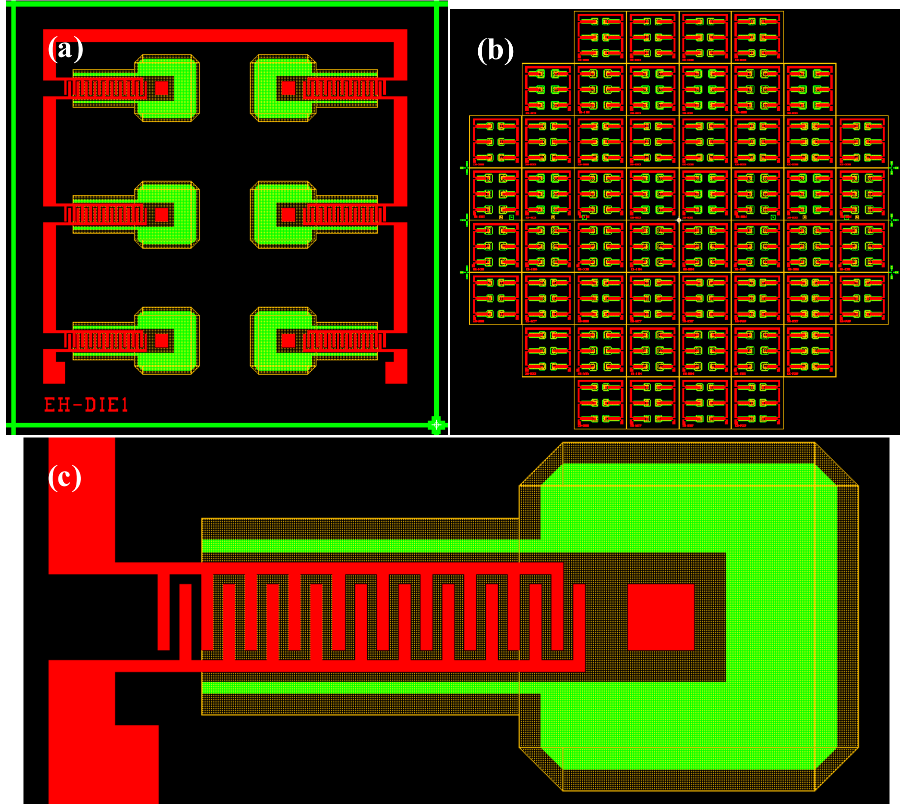

Figure 4.1 Designed devices: (a)Layout of six micro-cantilever energy harvesting beams, (b) layout of 4" wafer, and (c) close-up of a d_{33} mode cantilever beam.

4.2 Resonance frequency of cantilever beam

A composite cantilever beam resonance frequency can be calculated by using the theory developed in thesis of Sood[116]. For a composite beam, the effects of difference in modulus of each layer must be merged together to find the neutral axis $(\overline{Y})$ using Eq. (52) as:[117]

$$\overline{Y} = \frac{\Sigma Y_i A_i E_i}{\Sigma A_i E_i} \quad (52)$$

where Y_i is the height of centroid for composite layer i with corresponding cross sectional area A_i, and Young's modulus E_i. The spring constant k of the beam can be computed from the moment of inertia (I) given as:[118]

$$I_i = \frac{b_i \times h_i^3}{12} \quad (53)$$

where h_i is the height of the cross section and b_i is the width of beam. The moment of inertia needs to be adjusted for each material layer according to Eq. (54):[119]

$$\overline{I_i} = I_i + A_i \times \overline{h_i}^2 \quad (54)$$

where h_i is defined as $\overline{Y_i}$-$\overline{Y}$. In order to obtain the total stiffness of composite beam, we have to merge the contributions from each individual layer according to Eq. (55) as: [120]

$$EI_{Total} = \Sigma(E_i \times I_i) \quad (55)$$

Once EI_{Total} is known, the spring constant of beam can be calculated using the following expression[121]:

$$k = \frac{8 \times EI_{Total}}{L^3} \quad (56)$$

Using Eq. (73) and (74), we can estimate the natural frequency of composite cantilever beam by combining with Eq. (61) given in chapter 2. The dimensions of micro-cantilever beams for EH MEMS device are listed in Table 4.1.

Table 4.1 Dimension of micro cantilever beams

Parameter	**Value**
Width of a beam	0.6mm
Length of a beam	2.4, 2.6, 2.8mm
Thickness of cantilever beam	11µm (10µm silicon + 1µm barium titanate)
Number of interdigitated electrode pairs	10
Gap between electrodes	50, 60, 70, 80µm
Tip mass	1.53mg

The Young's modulus of Si and barium titanate was taken as: 107 x 10^9 Pa (N/m^2) [122] and 67 x 10^9 Pa (N/m^2)[123] respectively. The springs constants of three types of EH cantilever beam were found to be 19.25 N/m, 15.1 N/m, and 12.07 N/m. The mass of each cantilever beam was found to be 3.36 x10^{-8}kg, 3.63 x 10^{-8}kg, and 3.91 x10^{-8}kg which gives the working frequencies of 564 Hz, 498Hz, and 447Hz respectively. Figure 4.2 provides all the dimensional details.

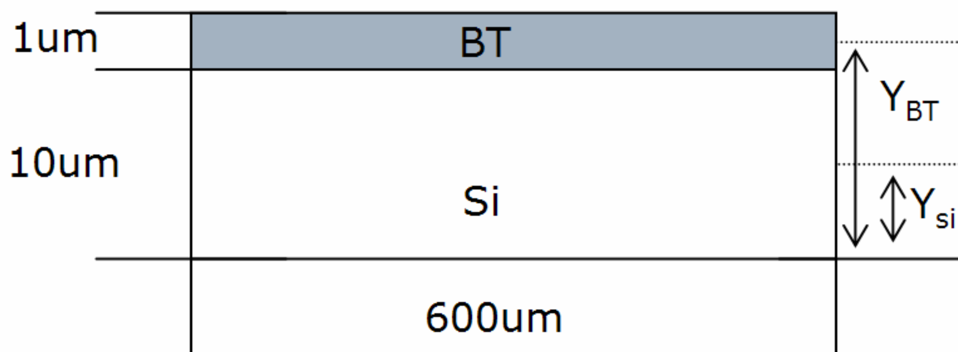

Figure 4.2 Neutral axis of each layer of cantilever beam

4. 3 Fabrication process design

Planning stage: We planned to start with a 4" <100> SOI (Silicon On Insulator) wafer. The thicknesses of the device, handle, and buried oxide layers were taken to be 10 μm, 500 μm, and 1 μm, respectively. The first step for EH device fabrication will be wet thermal SiO_2 deposition. The process temperature for this step will be 1100°C/5 hrs. A SiO_2 layer with 1.5 μm thickness will be grown in the oxidation furnace for KOH solution or DRIE etching mask. After removing top side thermally grown SiO_2 layer with RIE, BT film will be deposited using sol-gel process. After this step, top Cr/Au interdigitated electrodes will be deposited using thermal evaporation (NRC thermal evaporator) and lithography will be followed. PR1-2000A (Futurrex) resist will be deposited up to 4μm thickness using spin coater. Chrome was selected because it is a good adhesion layer between BT and gold layers. During metal deposition, the process chamber pressure will be maintained at 4 x 10^{-7} torr and the process current will be fixed at 40 A

for the Cr deposition and 120 A for Au deposition. After the lift-off process, the thickness of each layer will be 70 nm and 50 nm. A 2% HF solution will be used in order to etch BT layer and DRIE (Trion) will be used to etch 10µm thick Silicon layer. In order to fabricate the back side hard mask, DRIE (Trion) will be used. A Teflon chuck will be employed to protect the front side electrode and barium titanate thin film during KOH etching. The remaining and buried oxide will be etched out to release micro-cantilever beams using DRIE. As the last step, Sn/Au/Cu solder balls will be attached using glue to act as a tip mass. Figure 4.3 shows the planned process flow for EH device fabrication.

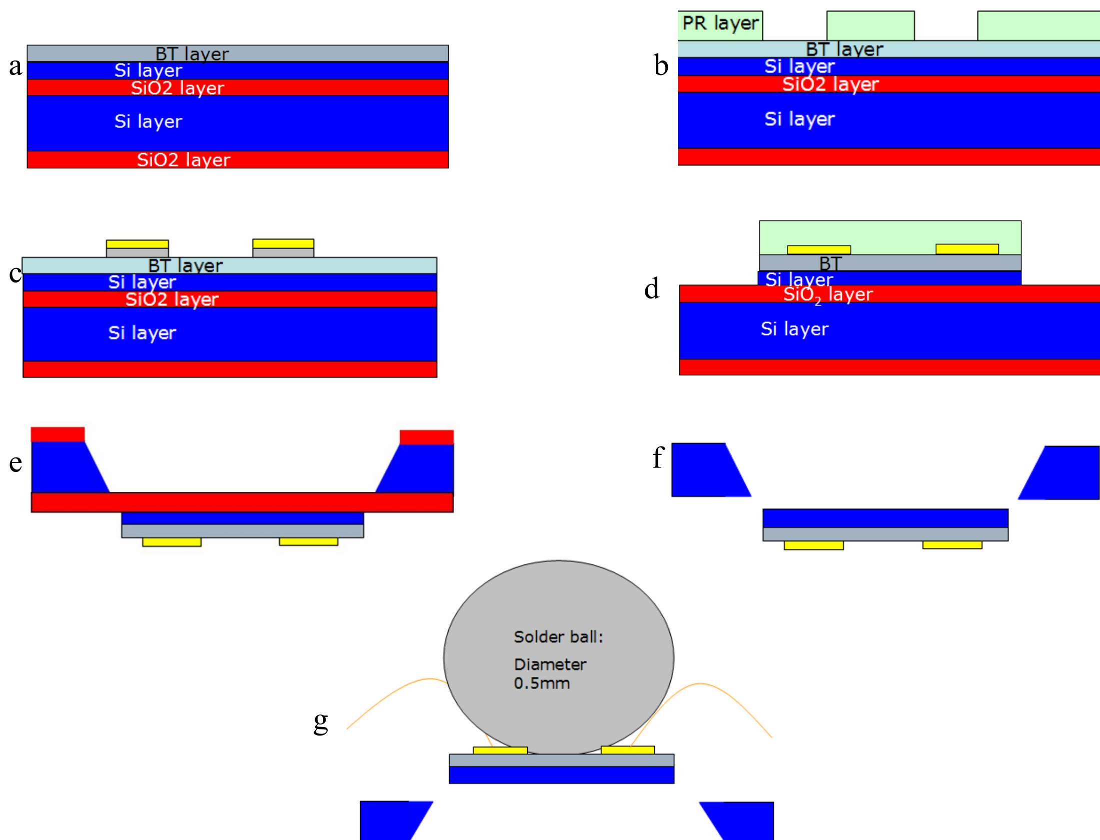

Figure 4.3 Designed EH MEMS fabrication process flow: (a) barium titanate deposition using sol-gel, (b) lithography, (c) Au/Cr IDT deposition & Lift-off, and (d) Wet etch of BT film with 2% HF & Si DRIE, (e) Thermal SiO_2 DRIE & Si etch with KOH or Si etch with DRIE, (f) SiO_2 dry etching using RIE, and (g) Wire bonding, tip mass attach & poling

4.3.1. Etching feasibility test of barium titanate polycrystalline thin film

The first trial in order to etch barium titanate polycrystalline thin film was dry etching using Micro RIE with CF_4, Ar and O_2 gas mixture. Applied power was 150W and mixture ratio was 9/36/5 sccm[124]. However, the etching effect after 20 min was negligible. The average etching rate was as small as 4.5nm/min. Figure 4.4 shows the profile of surface after RIE with Ar/CF_4/O_2 gas mixture (150W).

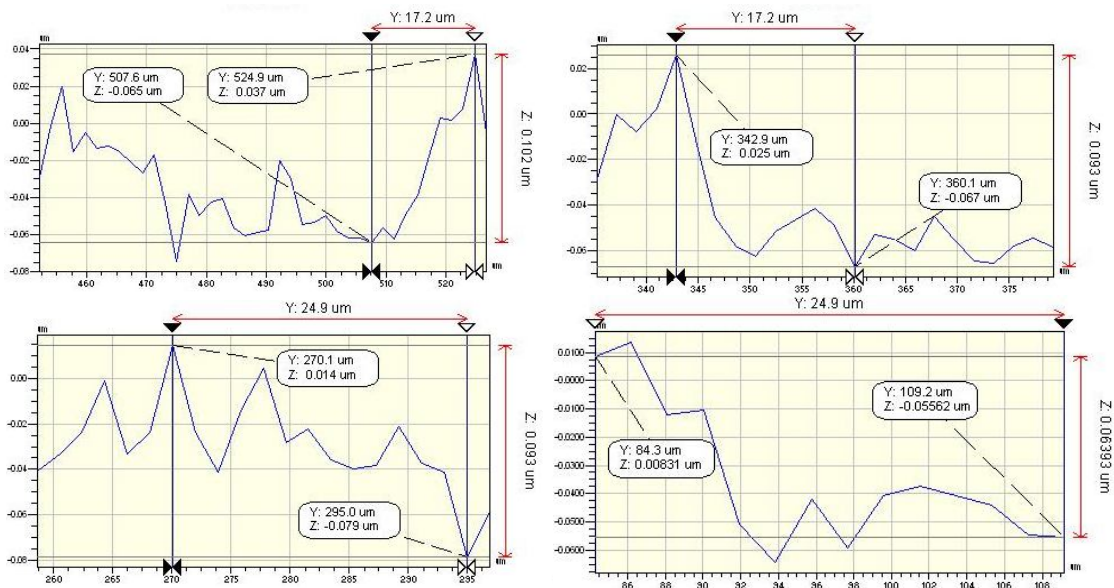

Figure 4.4 Profile of surface after RIE with Ar/CF_4/O_2 gas mixture (150W).

Next, we switched to wet etching method with 2% HF solution. Etch rate with 2% HF was in the range of 187nm/min to 86nm/min, as measured from Alpha step. The crystallized barium titanate thin films were etched for 5mins in 2% HF solution. The large variance of etching rate can be minimized by using a suitable etch stop layer. The products of the surface reactions between barium titanate thin film and HF can be expressed as:

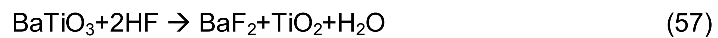

$$BaTiO_3 + 2HF \rightarrow BaF_2 + TiO_2 + H_2O \quad (57)$$

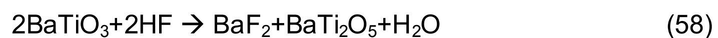

$$2BaTiO_3 + 2HF \rightarrow BaF_2 + BaTi_2O_5 + H_2O \quad (58)$$

During the second reaction, fluorine reacts with barium and produces BaF_2 and a Ba-polytitanate phase ($BaTi_2O_5$) with a low content of Ti. Figure 4.5 shows the etched $BaTiO_3$ layer after the feasibility test with 2%HF.

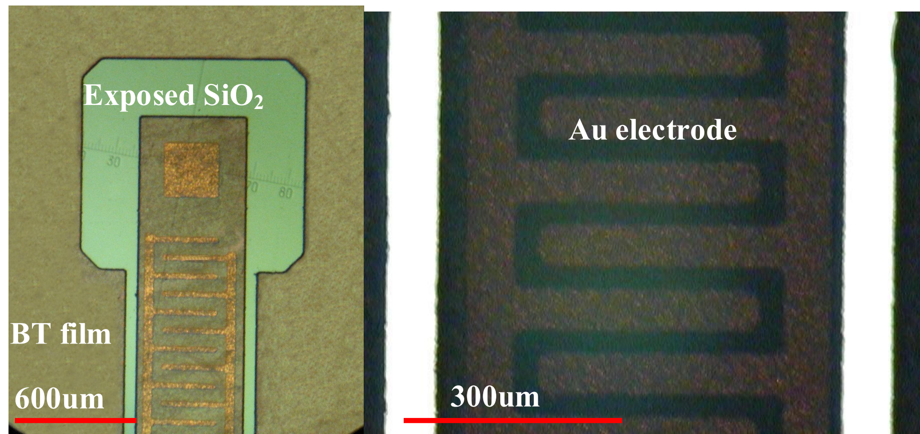

Figure 4.5 Optical microscopy after front side wet etching with 2% HF.

4.3.2. 500um Si wet etching feasibility test

Figure 4.6 shows the etch rate of Si <100>. Generally, <100> has the highest etching rate followed by <110> and than <111> in KOH/IPA solution.

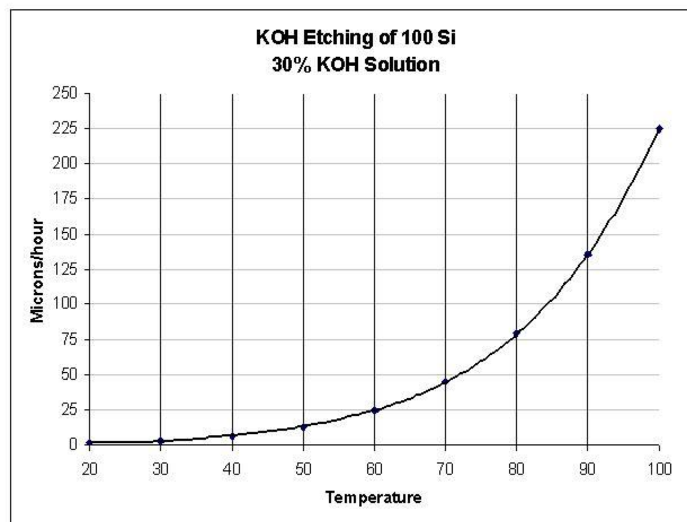

Figure 4.6. 30 wt% KOH etching of (100) Si[140] (Reproduced with permission from Electrochemical Society).

A 30wt% KOH solution was made by mixing 350g of KOH pellets (Sigma Aldrich) and 190ml of DI water (de-ionized water) on warm hotplate (~50°C). Isopropyl alcohol (IPA) in amount of 200ml was added into this solution. It is well known that isopropyl alcohol can enhance anisotropy of silicon etching solution. This 30 wt% KOH solution with IPA was heated to 80°C. Wafer was placed at bottom of Teflon chuck and to protect the front side, another Teflon chuck was placed on top of wafer with screw sealing. Etching time was fixed at 8 hrs 30min considering deviation of etching rate. Due to the evaporation of DI water and IPA during silicon etching, there was change in the concentration which required addition of more DI water in order to maintain 30 %wt KOH concentration. Figure 4.7 shows tilt view after etching with 30 wt % KOH solution.

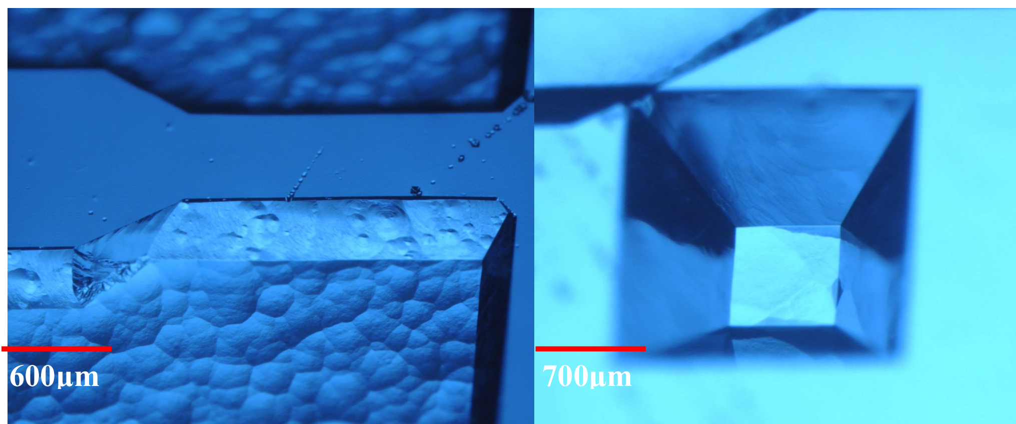

Figure 4.7 Optical microscopy after 500µm Si backside etching with 30 wt% KOH.

4.3.3. 500µm Si dry etching feasibility test with DRIE

In Bosch™ process which is also known as deep reactive ion etching (DRIE), plasma is cycled between a highly reactive SF_6 gas and hydrogen C_4F_8 species, creating high aspect ratio vertical cavities[125]. Since reactive etch has significantly high selectivity to the silicon than the silicon dioxide, it is possible to get 500µm thick deep cavity. The selectivity of Si to thermal SiO_2 is around 300:1[126]. Etching rate with DRIE was found to be 3µm/mins. Figure 4.8 explains the working principle of DRIE process and Fig. 4.9 shows the backside of wafer after DRIE.

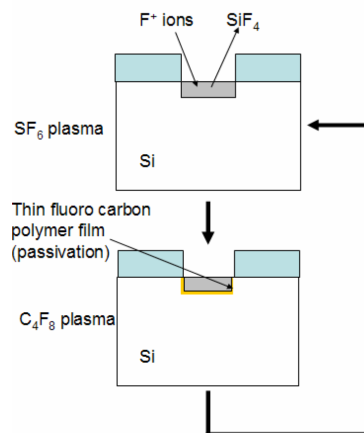

Figure 4.8 Working principle of DRIE process

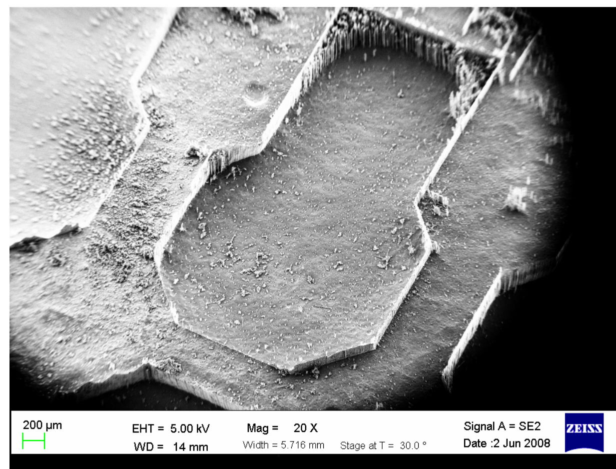

Figure 4.9 Backside of the energy harvesting device after DRIE process.

4. 4 Implementation of the fabrication process

4.4.1. EH (Energy Harvesting) device fabrication step1 and step 2

The process flow steps 1 and 2 are schematically depicted in Fig. 4.10.The first step consisted of deposition of BT (Barium Titanate) thin film on top of 4 inch SOI (Silicon On Insulator) wafer. It was found that the thicker is the PR, the easier is the lift-off process in acetone. Thus, a 4 µm thick PR was deposited on BT film with spinner parameter of 1000 rpm / 30 sec. After PR deposition (Futurrex PR1-2000A), OAI 806 aligner was used for lithography. A Cr/Au layer was deposited as top electrode and patterned as shown in Fig. 4.10(b) after lift-off.

(a)

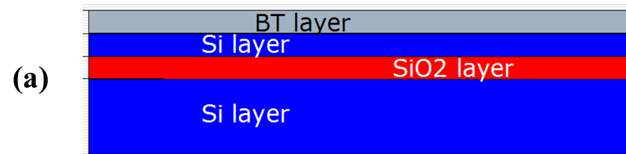

(b)

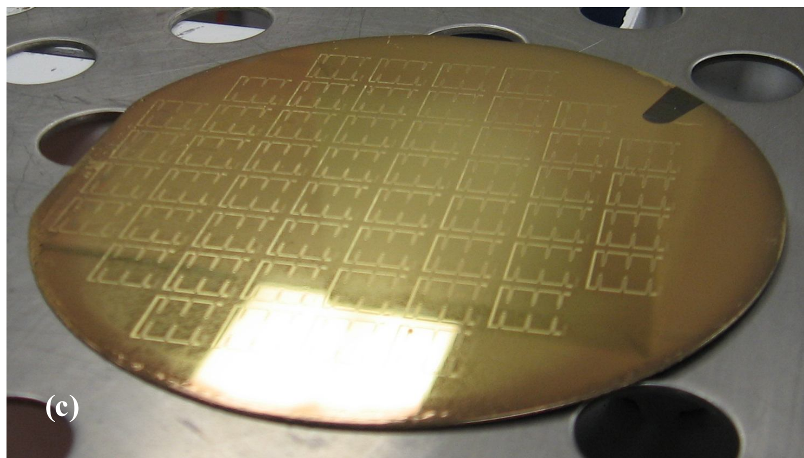

Figure 4.10 Schematic of fabrication process: (a) steps 1 (BT deposition using Sol-gel method on top of the 4 inch SOI wafer) & (b) step 2 (Cr/Au IDT electrode deposition on top of BT layer after lithography process), and (c) EH wafer after the Cr/Au top electrode deposition

4.4.2. EH (Energy Harvesting) device fabrication step 3 and step 4

The process flow steps 3 and 4 are schematically depicted in Fig. 4.11.The third step was PR deposition in order to protect electrodes during front side etching process. Lithography was done with OAI 806 mask aligner with exposure time of 18sec and the intensity of UV lamp was set at the default value of the aligner (same as step 2).

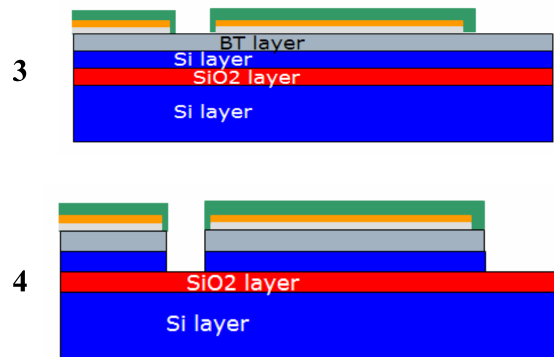

Figure 4.11 Schematic of process: step 3 (Photoresist deposition and lithography) & 4 (Barium titanate wet etching with 2% HF and Si device layer etch with DRIE)

The next step was wet etching of BT layer with 2% HF. After rinsing with DI wafer, a 10μm thick device layer was etched vertically with DRIE (Trion). Process parameters were 50 mTorr of pressure, 3000 W of ICP power and 50 W of RIE power. The gas flow rate of O_2 and SF_6 were 500 sccm and 50 sccm respectively. In order to cool down wafer during the DRIE process, Ar and He gas were infused on the bottom of wafer at 200 sccm flow rate. With these process parameters, etching rate of <100> was found to be 2 μm/min. The results are shown in Fig. 4.12.

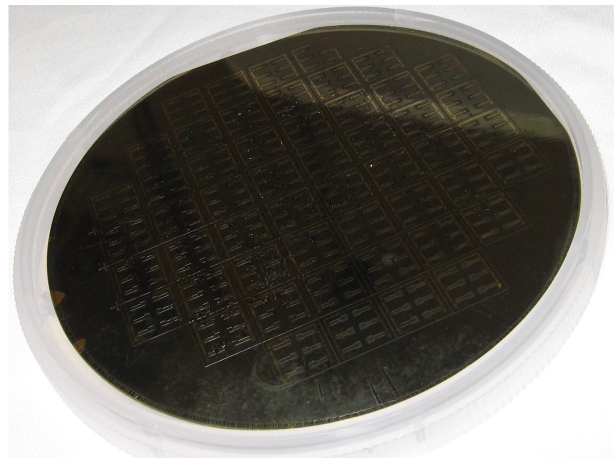

Figure 4.12 EH wafer after steps 3 & 4

4.4.3. EH (Energy Harvesting) device fabrication step 5 and step 6

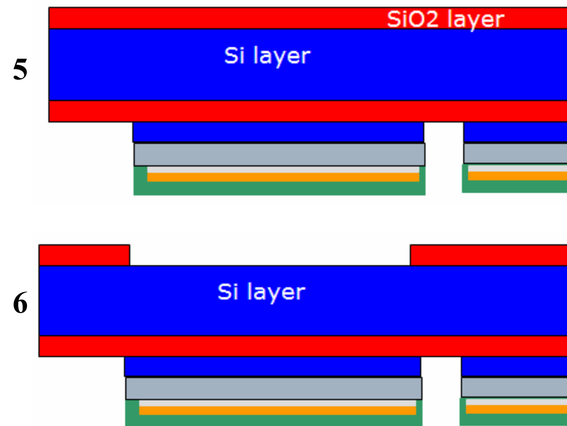

Figure 4.13 Schematic fabrication process flow: step 5 (PECVD SiO_2 deposition on the backside of the wafer) & 6 (SiO_2 hard mask pattern)

The process flow steps 5 and 6 are schematically depicted in Fig. 4.13. In practical fabrication processes, thermal SiO_2 growth has been avoided. During the SiO_2 growth with thermal oxidation, approximately 1 µm of Si can be consumed to make 2 µm thick SiO_2 mask. Hence, Trion PECVD tool was utilized to grow back side hard mask. ICP power was set at 300 W and temperature of the wafer holding chuck was maintained at 350 °C. The gas flow rate of N_2O, N_2 and SiH_4/Ar were fixed at 180 sccm, 250 sccm and 10 sccm respectively. With these parameters, the SiO_2 deposition rate was found to be 16.2 nm/min. The next stage in the fabrication was process step 5. In order to pattern PECVD SiO_2 hard mask, PR was deposited on top of the SiO_2 layer again. At this step, mask no. 3 was placed on OAI aligner and DRIE was used with 50 sccm CF_4 gas to etch SiO_2 hard mask. The results are shown in Fig. 4.14.

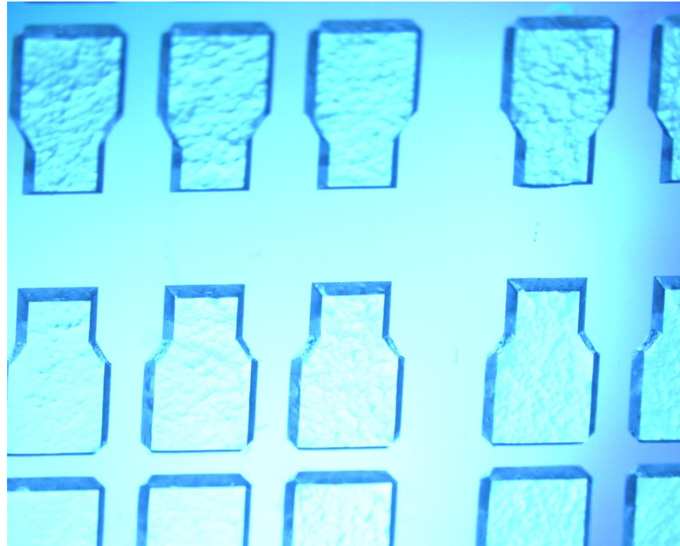

Figure 4.14 Patterned backside of the EH wafer

4.4.4. EH (Energy Harvesting) device fabrication step 7 and step 8

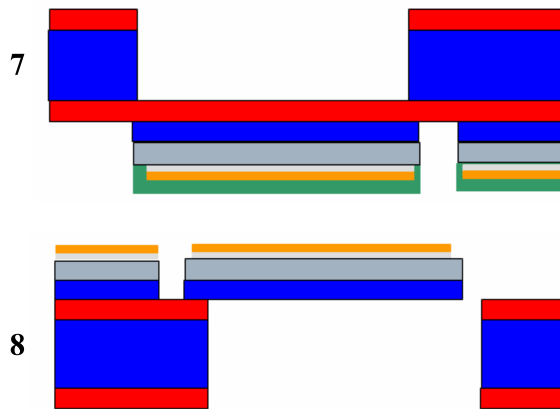

Figure 4.15 Schematic of process flow: step 7 (Back side 500 μm thickness Si DRIE) & step 8 (cantilever beam release by removing SiO_2 layer with DRIE)

Figure 4.15 schematically describes the processing steps 7 and 8. The BOSCH^{TM} process was selected instead of KOH for etching 500μm thick Si. BT film and electrodes on front side of wafer cannot endure heated KOH for long time even though this method is easy and suitable for laboratory. Individual EH die were separated using laser owing to mechanical weakness of wafer after the BOSCH ^{TM} process as shown in Fig. 4.16 and 4.17.

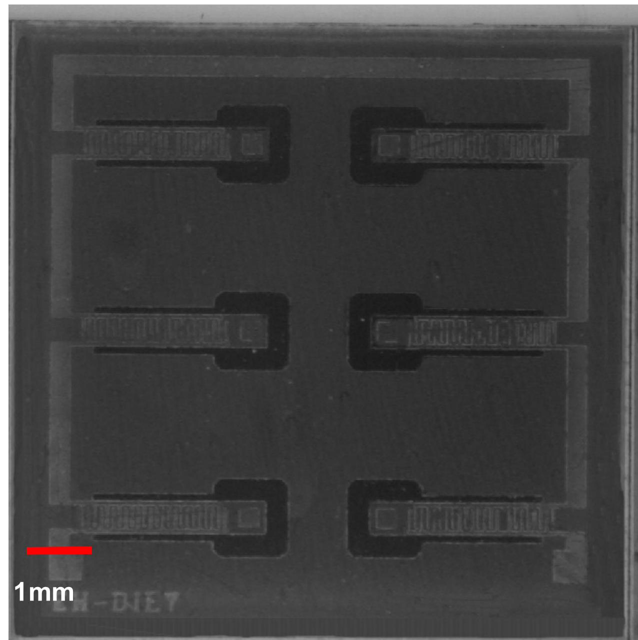

Figure 4.16 Energy harvesting device after laser wafer saw process (Front side)

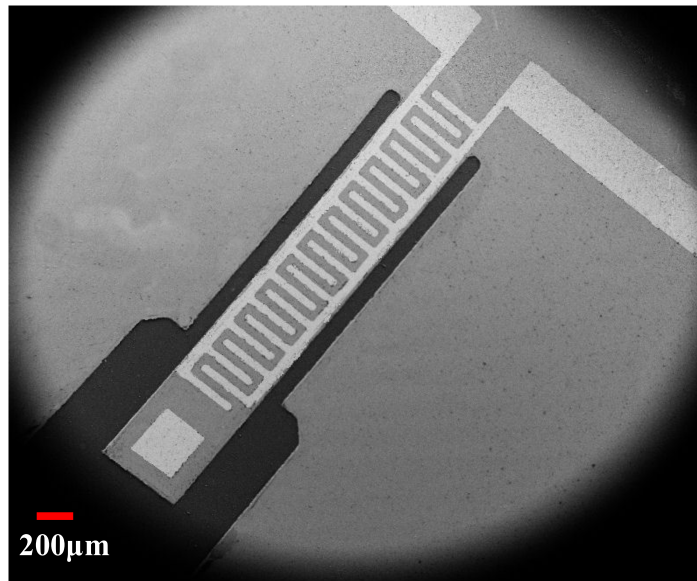

Figure 4.17 SEM image of the cantilever beam (Front side)

In order to release the cantilever beam, DRIE was used again. Figure 4.18(a) and (b) shows the SEM image of released cantilever beam.

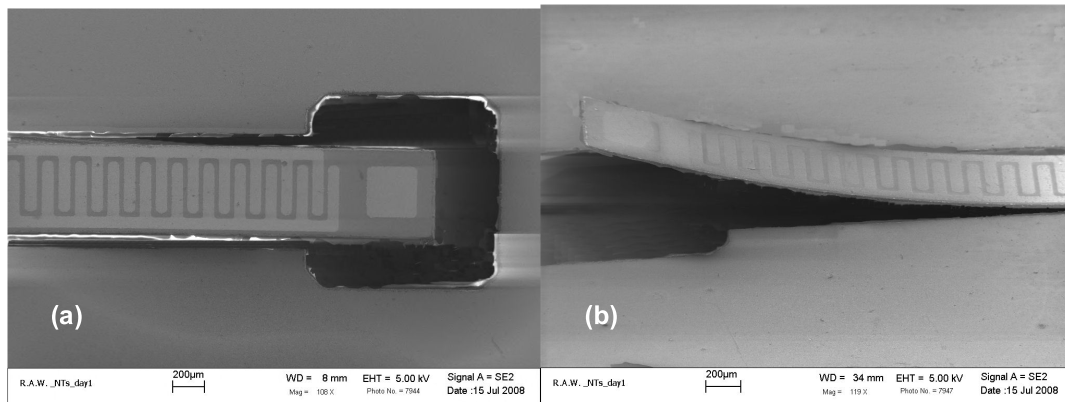

Figure 4.18 (a) Top view of released cantilever beam, and (b) Tilt view of released cantilever beam.

4.4.5. EH (Energy Harvesting) device fabrication final steps

Final steps of the EH device fabrication were packaging and poling process. After die attach using non-conductive epoxy, wire bonding was done on ceramic package. Figure 4.19 shows the packaged EH device. Poling process was conducted under 15V DC for 3 mins on the heated hotplate at 100 °C.

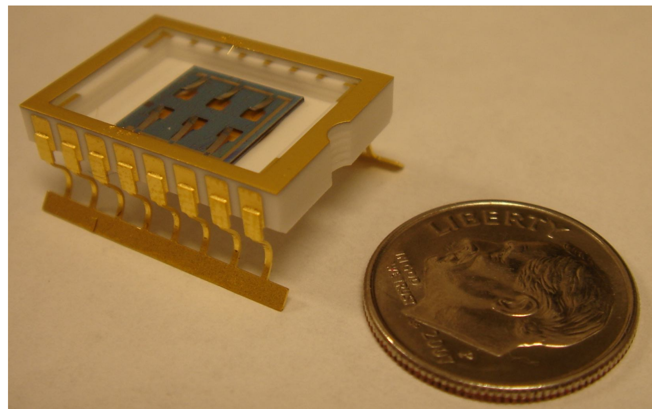

Figure 4.19 Packaged EH device

4. 5 Problems of fabrication process

During above device fabrication, there were several problems especially during back side mask alignment. Owing to movement of aligner mask, misaligned wafer was loaded into the DRIE chamber several times. By changing back side aligner equipped with IR scope from UCSB (University of California at Santa Barbara), it was possible to see well aligned device. Figure 4.20 shows mis-aligned die after laser dice saw process.

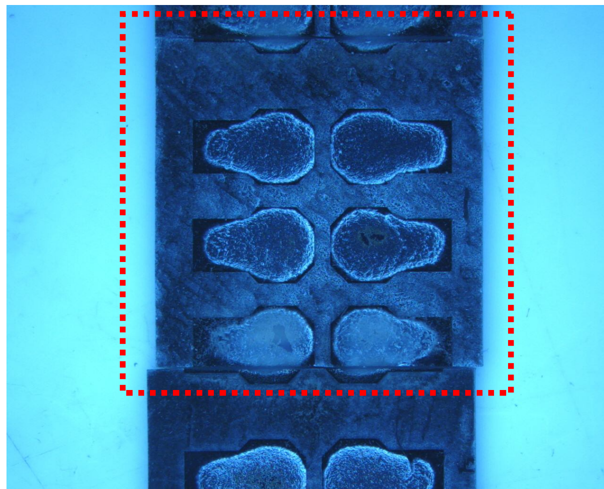

Figure 4.20 Backside mask mis-aligned device

Another problem that we experienced is related to back-side etching method. It was found that KOH solution attacks BT layer and thus DRIE should be used. Figure 4.21 shows the BT film damaged by KOH etching solution. We tried to use Teflon chuck in order to protect BT film layer during KOH etching process but Teflon chuck was deformed owing to the exposure to high temperature for long time.

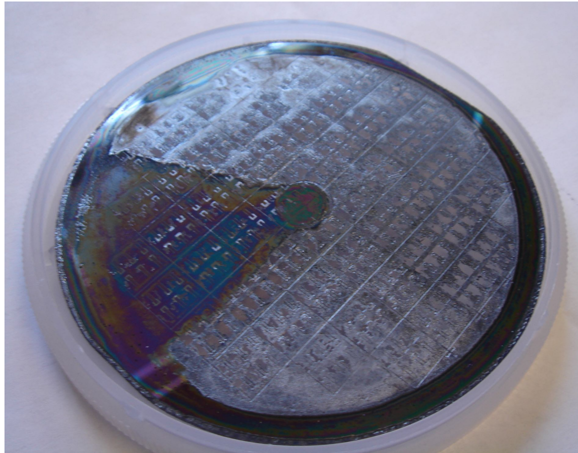

Figure 4.21 Damaged BT film on SOI wafer by exposure to KOH solution.

There was also challenge with the wire bonding process. We used thermal evaporation method to deposit top Cr/Au electrode layer. It is well known that adhesion of film using thermal evaporation is relatively weak and this is why Cr layer is used to increase the adhesion. However, the thickness of electrode was too thin to do wire bonding leading to peeling-off of electrode during wire bonding process. Figure 4.22 shows the peeled off wire bonding pad.

Figure 4.22 Peeling of wire bonding pad by wire bonder capillary.

4.6 Summary

The device fabricated in this study did not generate any significant voltage when tested under acceleration of 200 mg over a wide range of frequency up to 10 kHz. The reasons for this failure could be attributed to various reasons including (i) poor piezoelectric properties of BT film, and (ii) contamination of BT layer during the processing.

APPENDIX A

ATILA SIMULATION, THIN FILM SYNTHESIS, EH (ENERGY HARVESTING) MEMS DEVICE FABRICATION TOOL INFORMATION

(i) Chemicals from Sigma Aldrich

Website info:

http://www.sigmaaldrich.com/

Contact info:

Tel: 800-325-3010

- Barium acetate:

Product Number: B8767

- Titanium (IV) bis (ammonium lactate) dihydroxide solution with 50 wt. % in H_2O:

Product Number: 388165

- Acetic acid:

Product Number: 320099

- Potassium hydroxide (Semiconductor grade, 99.99% trace metals basis)

Product Number: 306568

- Isopropyl alcohol

Product Number: I9030

(ii) Chemicals from Futurrex Inc.

Web site info:

http://www.futurrex.com/

Contact info:

Tel: 973-209-1563

Fax: 973-209-1567

E-mail: info@futurrex.com

-PR1-2000A (Positive photoresist)

-RD 6 (Developer)

(iii) Gold pellet, Cr rod, and boat from Kurt J. Lesker company.

Web info:

http://www.lesker.com/newweb/menu_depositionmaterials.cfm?CFID=1305736&CFTOKEN=85820022

Contact info:

Tel: 412-387-9128

Fax: 412-384-2745

E-mail: systemscustomerservice@lesker.com

- Gold pellet

Part No: EVMAU40QXQ

- Chromium-plated Tungsten rods

Part No: EVSCRW1

- Alumina coated Boat

Part No: EVSME9AOMO

(iv) SOI (Silicon On Insulator) wafer from ultrasil corporation

Web info:

http://www.ultrasil.com/

Contact info:

Tel: 510-266-3700

Fax: 510-266-3720

E-mail: jdancovich@ultrasil.com

(v) MEMS process equipment

PWM32-PS-CB15PL spin coater

Website information:

http://www.headwayresearch.com

Contact information:

Tel: 972-272-5431

Fax: 972-272-7817

AG associates heatpulse210 : Rapid thermal annealing system

Website information:

http://www.ag-rtp.com/AG%20210.htm

Contact information:

sales@ag-rtp.com

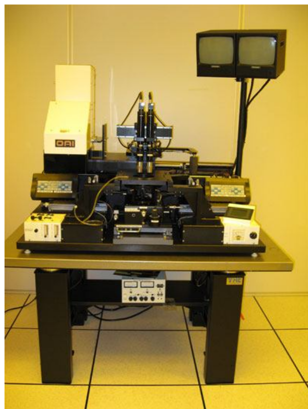

OAI model 806 manual front/backside

contact mask aligner

Website information:

http://www.oainet.com/

Contact information:

Tel: 408-232-0600

Fax: 408-433-9904

Technics Micro-RIE series 800

Website information:

http://www.sitekprocess.com/

Contact information:

info@technicsworldwide.com

NRC thermal evaporator

N/A

TRION Deep Reactive Ion etching(DRIE) System

Web information:

http://www.triontech.com

Contact information:

Tel: 727-461-1888

Fax: 727-461-1858

TRION ORION II PECVD system

Web information:

http://www.triontech.com

Contact information:

Tel: 727-461-1888

Fax: 727-461-1858

Kulicke & Soffa Model 4524 Ball bonder

Web information:

www.kns.com

Contact information:

Tel: 215-8=784-6000

Fax: 215-784-6001

Teflon fixture for front side protection during the KOH backside silicon etching

(vi) Lasi mask design software (Freeware)

Website information link:

http://lasihomesite.com/download.htm

(vii) Mask fabrication

Website information link:

http://www.outputcity.com/index.html

Contact Info:

CAD/Art Services, Inc.

Tel: 541-347-5315

Fax: 514-347-6810

E-mail: cas@outputcity.com

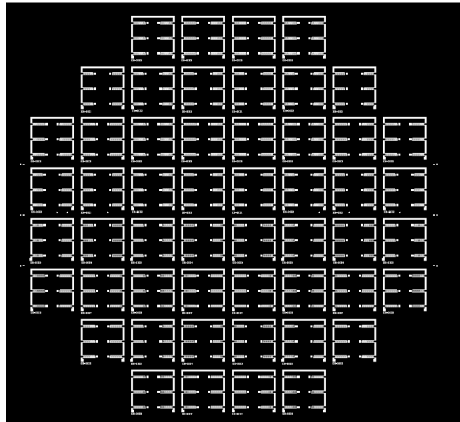

POSITIVE MASK FOR THE ELECTRODE DEPOSITION (MASK No.1)

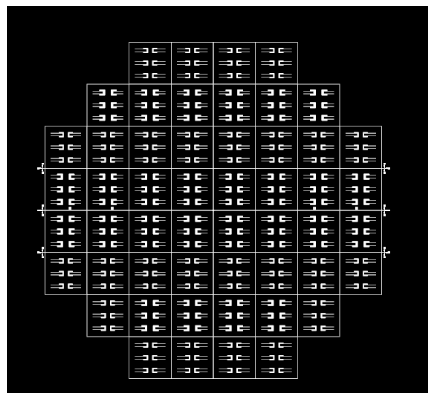

POSITIVE MASK FOR DEFINITION OF CANTILEVER BEAM (Mask No.2)

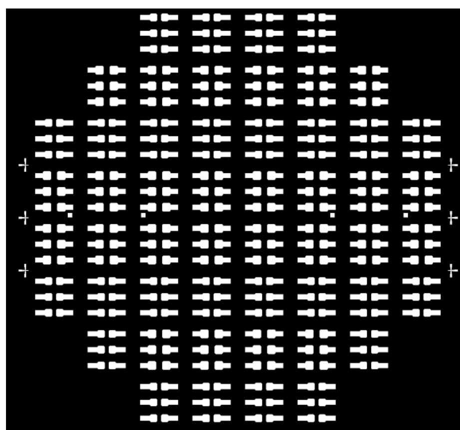

POSITIVE MASK FOR THE BACKSIDE ETCHING (MASK No.3)

(viii) NINN (National Nanotechnology Infrastructure Network)

University of California at Santa Barbara

Website information link:

http://www.nanotech.ucsb.edu/NanotechNew/nanotechhomepage.html

Contact information:

Jack Whaley

Tel: 805-893-8174

E-mail: whaley@ece.ucsb.edu

ATILA Simulation

Data used for simulation using ATILA:

Material Property	PZT	Silicon	Epoxy
Young's Modulus(GPa)		170	4.6
Poisson's Ratio		0.26	0.37
Density (kg/m^3)	7500	2300	1177
Elastic compliance (S_{11}^E, S_{12}^E, S_{13}^E, S_{33}^E, S_{44}^E, x 10^{-12} m^2/N)	12.3, -4.05, -5.31, 15.5, 39		
Piezoelectric charge constant (d_{15}, d_{31}, d_{33}, pC/N)	496, -123, 289		
Dielectric constant (ε_{11}, ε_{33})	1475, 1300		

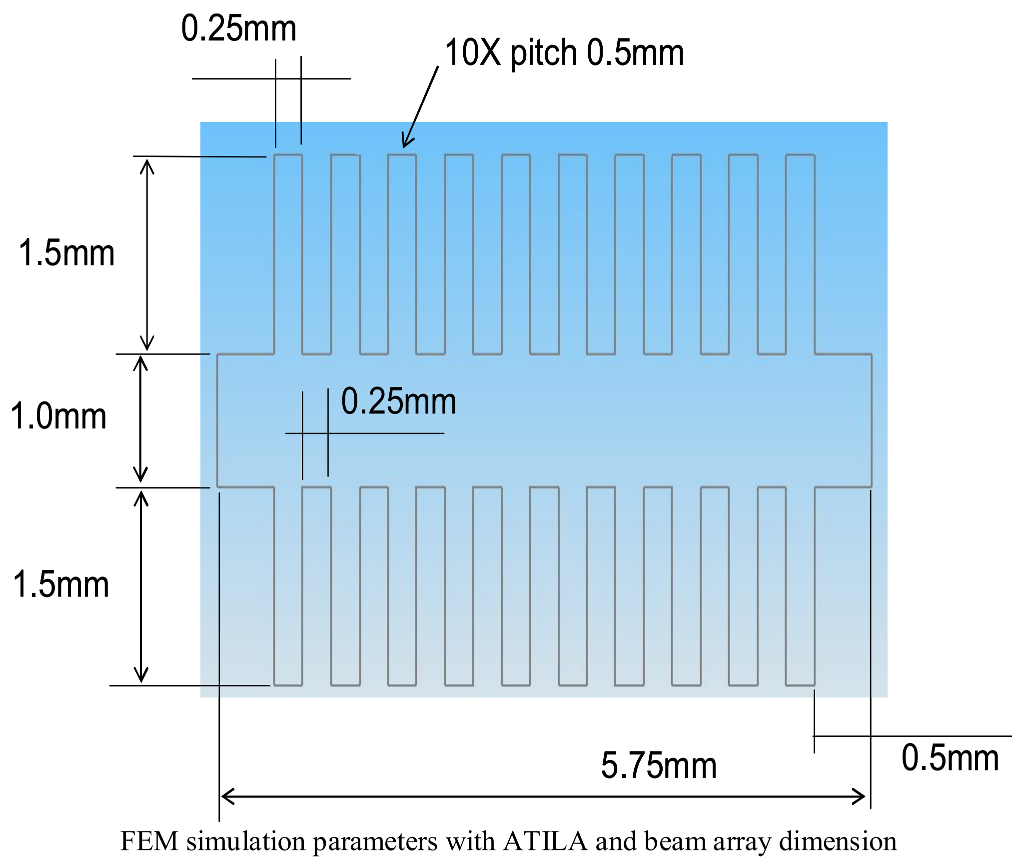

FEM simulation parameters with ATILA and beam array dimension

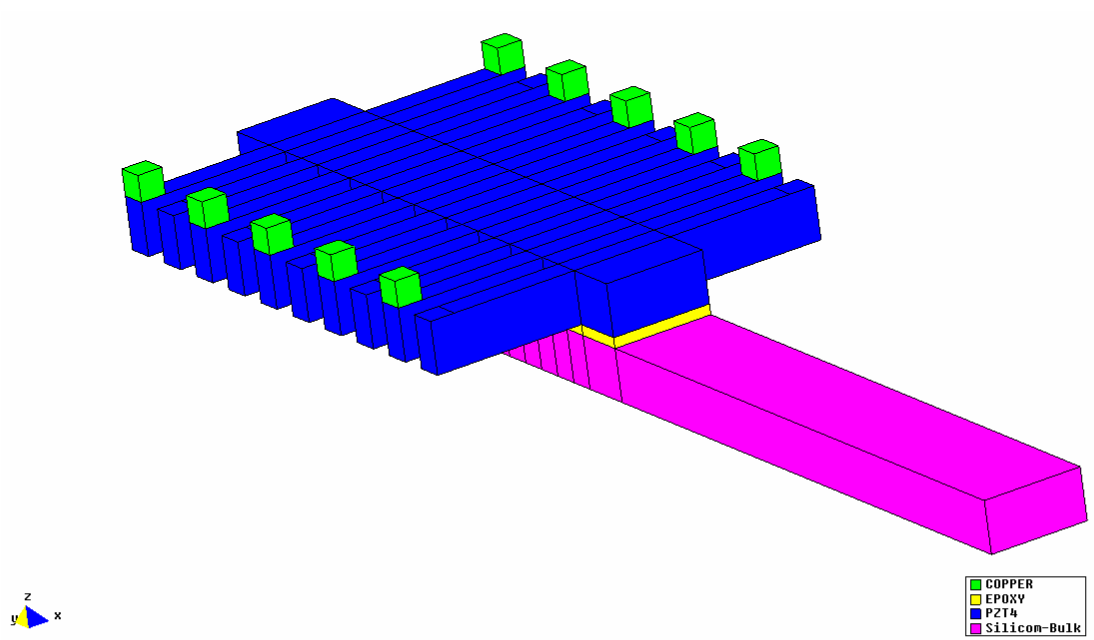

Simulation boundary consitions of mm scale energy harvesting device with ATILA

APPENDIX B

FIRST DRAFT OF STANDARD ON VIBRATION ENERGY HARVESTING

At the 2nd Annual Energy Harvesting Workshop held on January 30 – 31, 2007, Fort Worth, TX, a committee was formed consisting members from academia, industry, and federal labs. This committee was assigned the task of compiling current practices used to characterize the vibration energy harvesting devices and come up with a metric which can allow the comparison of all prototype harvesters. This first draft of standard is just a start and will be discussed in detail at the 4th Annual Energy Harvesting Workshop to be held on January 28 – 29, 2009, at Virginia Tech (http://www.cpe.vt.edu/ehw). Following is the list of the committee members:

Committee Members (alphabetical order)

Bob O'Neil, Morgan Electroceramics

Brad Mitchell, Boeing

Chris Ludlow, Mide Technology Corporation

Dan Inman, Virginia Tech

Farhad Mohammadi, Advanced Cerametrics, Inc.

J. K. Huang, Ferro Solutions

Jan Kunzmann, Smart Material

John Blottman, Naval Undersea Warfare Center

M. G. Prasad, Stevens Institute of Technology

Robert O'Handley, MIT / Ferro Solutions

Roger Richards, Naval Undersea Warfare Center

Shashank Priya, Virginia Tech

Energy harvesting: Energy recovery from freely available environmental resources. Primarily, the selection of the energy harvester as compared to other alternatives such as battery depends on two main factors: cost effectiveness and reliability. Another goal for energy harvesters has been to recharge the batteries in existing applications.

In recent years, several energy harvesting approaches have been proposed using photovoltaic, thermoelectric, electromagnetic, piezoelectric, and capacitive schemes. This first draft of standard addresses the issues related with the vibration energy harvesting which primarily utilizes electromagnetic, piezoelectric, and capacitive schemes. Most means of vibration energy harvesting (VEH) are based on a mechanically **resonant** device that is, hopefully, matched to the *vibration spectrum* of source. There are elements of various devices (inductive, piezo benders, magneto-electric) that are common, because they are all based on the forced, damped harmonic oscillator. Figure 1 shows the schematic of some of the common configurations used for piezoelectric harvesters consisting of cantilever, patches, and diaphragms.

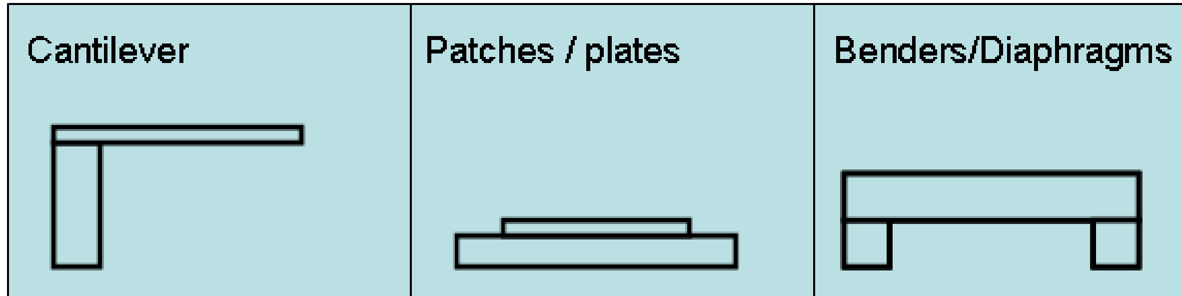

Figure 1: Common structures utilized for harvesting mechanical energy using piezoelectric transducers.

It is also possible to make **non-resonant** VEH devices. These fall into at least two categories: 1) mechanical systems that have *zero restoring force* (therefore $f_r = 0$) such as the shaker flashlights in which the freely-moving proof mass (the permanent magnet) essentially remains stationary while the flashlight case is shaken, and 2) systems designed to harvest *impact* or impulse forces.

1. Potential vibration sources for energy harvesting

Following is a list of vibration sources classified according to their elastic stiffness and Table I lists the sources according to the surrounding.

- stiff structures which make a movement by their own (ships, containers, mobile devices, housings of fans, escalators and elevators in public places, appliances, refrigerator, bridges, automobiles, building structures, trains)

- elastic structures which show an elastic deformation of their walls (rotor blades, wind mill blades, aircraft wings, pumps, motors, HVAC Ducts, rotorcraft)

- soft structures with very low elastic modulus and high deformation ratios (different textiles, leather, rubber membranes, piping with internal fluid flow)

Table I: Sources of energy available in the surrounding which are/can be tapped for generating electricity.

Human body	**Vehicles**	**Structures**	**Industrial**	**Environment**
Breathing, blood pressure, exhalation, body heat	Aircraft, UAV, helicopter, automobiles, trains	Bridges, roads, tunnels, farm house structures	Motors, compressors, chillers, pumps, fans	Wind

Walking, arm motion, finger motion, jogging, swimming, eating, talking	Tires, tracks, peddles, brakes, shock absorbers, turbines	Control-switch, HVAC systems, ducts, cleaners, etc.	Conveyors, cutting and dicing, vibrating mach.	Ocean currents, acoustic waves,

2. Parameters required to describe the source

(i) The **source of vibrations** should be described to clarify the extent to which the source is diminished or degraded by harvesting some of its energy. Sources undiminished by the VEH would be earth tremors or heavy machine vibrations while the sources diminished to some extent by VEH would include small machines or an energy harvester attached to the body.

(ii) The acceleration values for vibration source should be reported as peak to peak g level. The preferred unit for acceleration is in m/s^2 described in terms of "g" where 1g = 9.8 m/s^2. Acceleration can be further categorized as low (less than 10 mg), mid (10 – 100 mg) and high (above 100 mg).

(iii) The median frequency for vibration source should be reported in unit of Hz. Frequency can be categorized as low (less than 10Hz), mid (10 – 120 Hz) and high (above 120 Hz).

(iv) For non-resonant systems, the external vibration source needs to be described (by two of the four parameters *force, displacement, velocity, acceleration*) and the resulting motion of the VEH defined. For the impact systems, the impulse, $\int F(t)dt$, must be defined as best as possible and its frequency of occurrence or duty cycle specified.

3. Characterization of Vibration Energy Harvester

(i) Describe whether the VEH is uniaxial, biaxial or omnidirectional in its response.

(ii) In order to make the comparison of various types of vibration energy harvesters, a frequency of 60 Hz and acceleration of 1g is being set as the benchmark.

(iii) The direction of mounting for the optimum output should be specified. The type of mounting (using fasteners, glue based, permanent, nut-bolts, magnets) on the vibration source should be described.

(iv) Following table is being given here as an example to illustrate the parameters required for VEH. This is very crucial at this stage as it provides a method for comparison of various mechanisms and designs. In this table, the volume refers to the system volume which includes all the VEH components.

Table II: Compilation of the power density and optimum operating condition for various mechanical energy harvesting devices.

Power (µW)	f (Hz)	a (ms^{-2})	Volume (mm^3)	Power density (µW/mm^3)	Acceleration^2 (m^2/s^4)	Method	Mass (gm)
2	80	2	125	0.0168	4	Piezoelectric	10

Using this table a figure can be constructed in terms of energy density (Power density / frequency) and square of acceleration. In near future when the data becomes available we would like to start comparing all the VEHs on this one figure (see the reference in footnote).

(v) Describe the maximum operating temperature, range of acceleration and lifecycles at the rated frequency.

(vi) The testing of the VEH should include following three measurements: (i) RMS power as a function of vibration frequency at fixed acceleration (1g) and matching load, and (ii) power as a function of acceleration at fixed frequency (60 Hz) and matching load, and (iii) power as a function of load at fixed acceleration (1g) and frequency (60Hz).

4. Characterization of the Conditioning Circuit

(i) If the VEH being described is a system such that it includes power conditioning, then the rate at which conditioned power can be delivered to a defined load should be specified, namely, DC voltage level, load impedance, and current available to that load.

(ii) It should be mentioned that how much of the harvested power is consumed by the power conditioning circuit.

(iii) Describe the output on-time rating in X msec@Y mA.

REFERENCES

1. S. Roundy, P. K. Wright, and J. Rabaey, Comput. Commun, 26, 1131-1144(2003)
2. S. Roudny, B. P. Otis, Y.-H. Chee, J. M. Rabaey, and P. Wright, IEEE Int. Symposium on Low Power Elec. And Devices, Seoul, Korea, 25-27 August, 2003
3. http://www.enviroment.nsw.gov.au/noise/vibguide0643criteria.htm
4. S. Roundy, P. K. Wright, and J. Rabaey, Comput. Commun, 26, 1131-1144(2003)
5. S. Priya, J Electroceram, 19, 165-182(2007)
6. http://salamanca.khbo.be:8080/doks/do/files/FiSe8a8199820e31b83d010e65f7d7f20230/Human%2520Vibration%2520-%2520ba7054.pdf;jsessionid=3662E8F069842C4BC9E0BE803C8AE233?recordId=SKHB8a8199820e31b83d010e65f7d713022d
7. T. V. Buren, P. D. Micheson, T. C. Green, E. M. Yeatman, A. S. Holmes, and G. Troster, IEEE Sensors J. 6(1), 28-38 (2006)
8. C. B. Williams, R. B. Yates, in the 8th International Conference on Solid-state Sensors and Actuators, and Eurosensors IX, Stockholm, Sweden, 25-29 June, 369-372(1995)
9. C.B. Willimas, R. B. Yates, in the 8th International Conference on Solid state Sensors and Acutuators, and Eurosensors IX, Stockholm, Sweden, 25-29 June, 369-372(1995)
10. C.B. Williams, R. B. Yates, in the 8th International Conference on Solid state Sensors and Actuators, and Eurosensors IX, Stockholm, Sweden, 25-29 June, 369-372(1995)
11. S. Priya, Appl. Phys. Lett. 87(18), 184101(2005)
12. H. Kim, S. Priya, H. Stephanou, and K. Uchino, IEEE Trans. Ultrason. Ferroelec. Freq. Cntrl. 52, 1851-1859(2007)
13. B. Jaffe, W.R. Cook, W. R. Cook, and H. Jaffe “Piezoelectric Ceramics”, Academic press., (1971)
14. N. Setter “Piezoelectric materials in device”,2 (2002)
15. APC international Ltd “Piezoelectric Ceramics: Principles and Applications”, 7(2002)
16. B. Jaffe, W. R. Cook, and H. Jaffe “ Piezoelectric Ceramics”, Academic press, London, 36 (1971)
17. B. Jaffe, W. R. Cook, and H. Jaffe “ Piezoelectric Ceramics”, Academic press, London, 11-12 (1971)
18. B. Jaffe, W. R. Cook, and H. Jaffe “Piezoelectric Ceramics”, Academic press, London, 54-55 &77 (1971)
19. B. Jaffe, W. R. Cook, and H. Jaffe “Piezoelectric Ceramics”, Academic press, London, 54-55 &77 (1971)
20. B. Jaffe, W. R. Cook, and H. Jaffe “Piezoelectric Ceramics”, Academic press, London, 54-55 &77 (1971)
21. M. T. Penella, M. Gasulla, Proc. 2007 IEEE Instrumentation & Measurement Technology Confererence, 1807-1811, 2007
22. M. T. Penella, M. Gasulla, Proc. 2007 IEEE Instrumentation & Measurement Technology Confererence, 1807-1811, 2007
23. M. T. Penella, M. Gasulla, Proc. 2007 IEEE Instrumentation & Measurement Technology Confererence, 1807-1811, 2007
24. M. T. Penella, M. Gasulla, Proc. 2007 IEEE Instrumentation & Measurement Technology Confererence, 1807-1811, 2007

25. M.T. Penella, M. Gasulla, Proc. 2007 IEEE Instrumentation & Measurement Technology
32. http://www.smart-material.com/media/Publications/MFCdata%2013-3-web.pdf
33. http://www.cedrat.com/en/technologies/mechatronic-systems/energy-harvesting.html
34. http://www.kcftech.com/products/wirelesssensors.shtml
35. http://www.mide.com/products/volture/volture_catalog.php
36. http://powercastco.com/product/
37. http://www.perpetuum.co.uk/home.php?page_id=11
38. http://www.ferrosi.com/
39. http://www.hi-z.com/
40. http://www.enocean.com/en/enocean_modules/eco-100/
41. http://www.kryotherm.ru/
42. R. R. Gattass, and E. Mazur, nature photonic 2, 219-225(2008)
43. M. Xia, and Y. Tu, Prod. 2005 MEMS, NANO and Smart Systems, 296-300(2005)
44. N. Uppal, P. S. Shiakolas, and S. Priya, Ferro. Lett., 32, 67-77(2005)
45. J. P. Maria, S. Trollier-Mckinstry, D. G. Scholm, Prod. 10TH IEEE. Intl. Symp, Application of Ferroelectrics, 18-21 (1996)
46. M.G. Norton, K. P. B. Craknell, and C. B. Carter., J. Am. Cera. Soc., 75, 1999-2002(1992)
47. H. A. Lu, L. A. Wills, and B. W. Wessels, Appl. Phys. Lett. 64(22), 2973-2975(1994)
48. W. Zhu, S. A. Akbar, R. Asiaie, P. K. Dutta, J. Electroceram., 2:1, 21-31(1998)
49. M. N. Kamalasana, N. D. Kumar, and S. Chandra, J. Appl. Phys. 74(9), 5679-5686(1993)
50. B. Lee, J. Zhang, Thin Solid Films, 388, 107-113 (2001)
51. P. G. Clem, J. A. Voigt, E. R. Byhoff, M. V. Stry, T. J. Headley, and N. A. Missert, J. Am. Ceram. Soc., 82(9), 2359-2367(1999)
52. H. B. Sharma, H. N. K. Sharma, Thin Solid Films, 330, 178-182 (1998)
53. M. N. Rahaman, Ceramic processing and sintering, Marcel Dekker, INC, New York, 265 (2003)
54 M. H. Frey, Ph. D dissertation, Grain size effect on structure and properties for chemically prepared barium titanate, Universty of Illinois at Urbana-Champaign, 37(1996)
55. M. N. Rahaman, Ceramic processing and sintering, Marcel Dekker, INC, New York, 265 (2003)
56. G. W. Scherer, J. Sol-Gel. Sci. Tech, 8, 360(1997)
57. M. molttern, F. Tyholdt, A. Ulyashin, Antonius T. J. van Helvoort, H. Verweij, and R. Bredesen, Thin Solid Films, 515(7-8), 3921(2007)
58. M. L. Mottern, F. Tyholdt, A. Ulyashin, Antonius T. J. van Helvoort, H. Verweij, and R. Bredesen, Thin Solid Films, 515(7-8), 3921(2007)
59. M. L. Motern, F. Tyholdt, A. Ulyashin, Antonius T. J. van Helvoort, H. Verweij, and R. Bredesen, Thin Solid Films, 515(7-8), 3921(2007)
60. A. J. Bell, J. Appl. Phys. 89, 3907(2001)
61. M. Davis, D. Damjanovic, D. Hayem, and N. Setter, J. Appl. Phys 98, 014102(2005)
62. S. Wada et al., Jpn. J. Appl. Phys., Part 1 38, 5505(1999)
63. M. Zgonik et al., Phys. Rev. B 50, 5941(1994)
64. K. Yako, H. Kakemoto, T. Tsursumi and S. Wada, Mater. Sci. Eng., B, 120(1-3), 181-185(2005)
65. S-E. Park, S. Wada, L. E. Cross, and T. R. Shrout, J. Appl. Phys. 86(5), 2746(1999)
66. S. Aachboun, and P. Ranson , J. Vac. Sci. Technol, A17(4), 2271 (1999)
67. K. P Larsen, and J. T. Ravnkilde, J. Micromech. Microeng. 15, 875(2005)
68. J. W. Gardner, V. K. Varadan, Microsensors MEMS and Smart Devices, John WILEY & Sons Ltd, England, 23 (2001)
69. M. Gad-el-hak, MEMS design and fabrication, Taylor & Francis, New York, 3-40(2006)
70. G. Kelly, et al, J. Micromech, Microengy, 7, 99-103 (1997)
71. J.W. Gardner, V. K. Varadan, Microsensors MEMS and Smart Devices, John Wiley & Sons Ltd, England, 15-16 (2001)

72. J. W. Gardner, V. K. Varadan, Microsensors MEMS and Smart Devices, John Wiley & Sons Ltd, England, 16-17 (2001)
73. W.H. Ko, Proc. 4th Int. Conf. and Micro opto Mechanical systems and Components, Berlin, Germany, 477-480 (1994)
74. http://www.siliconfareast.com/lith_electron.htm
75. Rao R. Tummala “Fundamentals of Microsystems packaging”, McGraw-Hill professional, New York, 22(2001)
76. Y. B. Jeon, R. Sood, J-H. Jeong, and S-G. Kim, Sens. Act. A, 122, 16-22(2005)
77. H. B. Fang, J. Q. Liu, Z. Y. Xu, L. Dong, L. Wang, D. Chen, B. C. Cai, and Y. Liu, Microelectron. J., 37, 1280-1284(2006)
78. D. Shen, J-H. Park, J. Ajitsaria, S-Y Choe, H. C. Wikle III, and D-J Kim, J. Micromech. Microeng 18, 4(2008)
79. P. Glynne-Jones, S. P. Beeby, and N. M. White, IEEE. Proc.-Sci. Meas. Techno. 148, 68-72(2001)
80. S. Roundy, P. K. Wright, and J. Rabaye, Comput. Commun. 26, 1131-1144(2003)
81. C. B. Williams, C. Shearwood, M. A. Harradine, P. H. Mellor, T. S. Birch, and R. B. Yates, IEE Proc. Circuits Dev. Syst. 148, 337-342 (2001)
82. C. B. Williams, and R. B. Yates, Sens. Act. A 52, 8-11 (1996)
83. P. Glynne-Jones, M. J Tudor, S. P. Beeby, and N. M. White, Sens. Act. A 110, 344-349(2004)
84. www.perpetuum.co.uk
85. P. Mitcheson, B. Stark, P. Miao, E. Yeatman, A. Holmes, and T. Green, Proc. Eurosensors XVII, 30-31 (2003)
86. Y. Arakawa, Y. Suzuki, and N. Kasagi, Power MEMS Conference, Kyoto, Jpn, 187-190(2004)
87. G. Despesse, T. jager, J. Chaillout, J. Leger, A. Vassilev, S. Basrour, and B. Chalot, Proc. Design, Test, Integration and Packaging of MEMS and MOEMS, 386-390(2005)
88. H. Kim, V. Bedekar, R. Islam, W. Lee, D. Leo, and S. Priya, IEEE Ultrason. Freq. Ferroelect. Cntrl., (2008)(Accepted)
89. S. P. Beeby, R. N. Torah, M. J. Tudor, P. Glynn-Jones, T. O’Donnell, C. R. Saha, and S. Roy, J. Micromech. Microeng. 17, 1257-1265(2007)
90. N. N. H. Ching, H. Y. Wong, W. J. Li, P. H. W. Leong, and Z. Wen, Sens. Act. A 97-98, 685-690(2002)
91. S. Kulkarni, E. Koukharenko, R. Torah, J. Tudor, S. Beeby, T. O’Donnell, and S. Roy, Sens. Act. A, (2007)
92. E. K. Reilly, E. Carleton, P. K. Wright, Proc. Int’l. Workshop. Wearable & implantable body sensor networks(2006)
93. S. P. Beeby, M. J. Tudor, and N. M. White Mease, Sci. Technol. 17, R175-R195 (2006)
94. H. Kim and S. Priya, Proc. ISAF(2008)
95. C. D. Richards, M. J. Anderson, D. F. Bahr, and R. F. Richards, J. Micromech. Microeng., 14, 717-721(2004)
96. N. Uppal, P. Shikolas, S. Priya, Ferroelectric letters section, 32, 67-77(2006)
97. D. Shen et al., J. Micromech. Microeng, 18,2-7, (2008)
98 .E. K. Reilly, E. Caleton, P. K. Wright, Proc. Int’l Workshop on wearable and implantable body sensor networks, 38-41(2006)
99. S. Trolier-Mckinstry, and P. Murlat, J. Electroceram. 12, 7-17(2004)
100. P. Muralt, J. Micromech. Microeng. 10, 136-146(2000)
101. K. Lefki, and G. J. M. Dormans, J. Appl. Phys. 76, 1764-1767(1994)
102. K. Yako, H. Katemoto, T. Tsurumi, S. Wada, Mater. Sci. Eng., B, 120, 181-185(2005)
103. J. Ouyang, R. Ramesh, and A. L. Roytburd, Appl. Surf. Sci, 252(10), 3394 (2006)
104. X.-H. Du, U. Belegundu, and K. Uchino, Jpn. Appl. Phys. 36, 5580-5587(1997)
105. B. Lee, and J. Zhang, Thin Solid Films, 388, 107-113(2001)

106. K. E. Boggs, D. L. Wilcos, Sr., David A. Payne, and L. H. Allen, MCM, Proc. Of he 1994 Int'l con, 350-355(1994)
107. H. Schmidit, G. Rinn, R. Naβ and D. Sporn. Mat. Res. Soc. Symp., 121, 743(1988)
108. Y. L. Tu, M. L. Calzada, N. J. Phillips, and S. J. Milne, J. Am. Ceram. Soc., 79, 441(1996)
109. H. Kozuka, M. Kajimura, T. Hirano, and K. Katayama, J. Sol-Gel Sci. Tech., 19, 205-209(2000)
110. R. Glang, R. A. Holmwood, and R. L. Rosenfeld, Rev. Sci. Instrum. 36, 7(1965)
111. S. Heane, E. Chason, J. Han, J. A. Floro, J. Figiel, and J. Hunter, Appl. Phys. Lett, 74, No3, 356-358(2001)
112. W. G. Hu, X. L. Liu, C. M. Jiao, H. Y. Wei, T. T. Kang, P. F. Zhang, R. Q. Zhang, H. B. Fan and Q. S. Zun, J. Phys. D: Appl. Phys. 40, 7462-7466(2007)
113. Y. B. Jeon, R. Sood, J. H. Jeong, S. G. Kim, Sens. Act. A, 122, 16-22(2005)
114. http://www.daviddarling.info/encyclopedia/S/AE_series_connection.html
115. http://www.daviddarling.info/encyclopedia/P/AE_parallel_connection.html
116. R. K. Sood, Master's thesis, Dept of CSE, MIT, Cambridge, MA(2003)
117. R. K. Sood, Master's thesis, Dept of CSE, MIT, Cambridge, MA, 18(2003)
118. R. K. Sood, Master's thesis, Dept of CSE, MIT, Cambridge, MA, 19(2003)
119. R. K. Sood, Master's thesis, Dept of CSE, MIT, Cambridge, MA, 19(2003)
120. R. K. Sood, Master's thesis, Dept of CSE, MIT, Cambridge, MA, 19(2003)
121. R. K. Sood, Master's thesis, Dept of CSE, MIT, Cambridge, MA, 19(2003)
122. K. E. Petersen, Proc. IEEE., Vol. 70, No. 5, 421(1982)
123. APC international Inc "Piezoelectric Ceramics: Principles and applications" , APC international, 27(2002)
124. B. Zhang, Z. Quan, T. Zhang, and T. Cuo, J. Appl. Phys. 101, 014107(2007)
125. H. Seidel, L. Csepregi, A. h S, J. Electrochem. Soc. Vol 137, 11, 3612-3632 (1990)
126. C. Chang, Y-F. Wang, Y. Kanamori, J-J. Shih, Y. Kawai, C-K Lee, K-C Wu, and M. Esashi, J. Micromech. Microeng, 15, 580 (2005)
127. K. Uchino, E. Sadannaga, and T. Hirose, J. Am. Ceram. Soc. 72. 1555(1989)
128. M. H. Frey, Ph. D dissertation, Grain size effect on structure and properties for chemically prepared barium titanate, University of Illinois at Urbrana-Champaign, 174(1996)
129. Y. B. Jeon, R. Sood, J-H. Jeong, and S-G. Kim, Sens. Act. A, 122, 16-22(2005)

BIOGRAPHICAL INFORMATION

HyunUk Kim was born in Seoul, Republic of Korea. He received his bachelor of engineering degree in materials science and engineering from Hong-Ik University, Seoul, Republic of Korea. Prior to joining to University of Texas at Arlington (UTA), he was a R&D engineer at STATsChippac Korea(SCK), Icheon, Republic of Korea and Signetics Crop, Paju, Republic of Korea. During this period, He has been participated several projects which are microelectronic packaging especially 3D package and has authored 2 US patents. And after joining the UTA, he published 1 paper and 2 conference papers. His research interest is piezoelectric materials for the MEMS application and design.